A Numerical Investigation of the Gas-Phase Dynamics of Small Pool Fires

Anay Luketa-Hanlin

A dissertation submitted in partial fulfillment of the
requirements for the degree of

Doctor of Philosophy

University of Washington

2002

Program Authorized to Offer Degree: Mechanical Engineering

ProQuest Information and Learning Company
300 North Zeeb Road
P.O. Box 1346
Ann Arbor, MI 48106-1346

In presenting this dissertation in partial fulfillment of the requirements for the Doctoral Degree at the University of Washington, I agree that the Library shall make its copies freely available for inspection. I further agree that extensive copying of the dissertation is allowable only for scholarly purposes, consistent with "fair use" as prescribed in the U.S. Copyright Law. Requests for copying or reproduction of this dissertation may be referred to Proquest Information and Learning, 300 North Zeeb Road, Ann Arbor, MI 48106-1346, to whom the author has granted "the right to reproduce and sell (a) copies of the manuscript in microform and/or (b) printed copies of the manuscript made from microform."

Signature Amay Luketa-Hanlin

Date August 15, 2002

University of Washington
Graduate School

This is to certify that I have examined this copy of a doctoral dissertation by

Anay Luketa-Hanlin

and have found that it is complete and satisfactory in all respects,
and that any and all revisions required by the final
examining committee have been made.

Chair of Supervisory Committee:

Richard C. Corlett

Reading Committee:

Richard C. Corlett

John C. Kramlich

James J. Riley

Date: Aug. 14, 2002

University of Washington

Abstract

A Numerical Investigation
of the Gas-Phase Dynamics of Small Pool Fires

Anay Luketa-Hanlin

Chair of the Supervisory Committee:
Professor Emeritus Richard C. Corlett
Mechanical Engineering

This work is an investigation, through direct numerical simulation, of the gas-phase dynamics of small circular pool fires. The objectives are: to determine the mechanisms that contribute to vortex formation and their relative magnitude as dependent upon the Froude and Reynolds number, the frequency response of the flame as dependent upon the Froude and Reynolds number; and to determine the diameter limit of the axisymmetric assumption by formulating a local Reynolds number. The parametric range investigated is $10^{-4} \leq Fr \leq 10^{-2}$ and $10 \leq Re \leq 10^{2}$. The effect of heat release rate, flame temperature, fuel molecular weight and air-fuel ratio on the vortex formation mechanisms is also investigated. The vortical formation mechanisms include baroclinic torque, density gradient/gravity interaction, stratified shear layers, and density inversion. Stratified shear layers and density inversion are investigated by formulating a kinetic energy of fluctuation equation and evaluating the pertinent production terms. Time-averaged, as well as Favre-averaged, spatially integrated values are obtained as a function of elevation. The flow is modeled as axisymmetric, and an infinitely fast chemical reaction, thin-flame sheet model is used along with a low Mach number approximation. The time-dependent governing equations are solved in axisymmetric coordinates with an explicit, projection-based algorithm. The results indicate that radial density gradients interacting with gravity and unstable density stratification are the dominant mechanisms effecting vortex formation. Baroclinic torque is also significant. The net effect of shear is to provide stability, though local areas exist which are destabilizing. Local regions of stabilizing density stratification also occur. The Froude number, Reynolds number, heat release rate, flame temperature, fuel molecular weight and air-fuel ratio effect the investigated flame dynamics. The Froude number is the dominant parameter effecting the investigated

vortex generation mechanisms. An approximate critical local Reynolds number can be identified for which an axisymmetric model is valid. Using available experimental evidence, this value as been found to be around 3000. It is concluded, for this range that an axisymmetric, single-step, irreversible, reaction model with finite rate chemistry is capable of capturing essential features of the gas-phase of small pool fires.

TABLE OF CONTENTS

LIST OF FIGURES

LIST OF TABLES

Acknowledgements

I am grateful to R.C. Corlett for providing his guidance and wisdom, and to J.J. Riley for his insight and valuable suggestions. I would like to thank the other members of my supervisory committee, J. C. Kramlich and G. Kosály, for providing their guidance. These four individuals have allowed be to learn a great deal and to be successful in the program. I feel forever indebted to them for their kindness.

Finally, I would like to acknowledge the support of my family, especially my daughter Amanda for making me lunch this past summer while I worked to complete my degree. She even made dinner half the time. Thanks kiddo!

Dedication

To my family

Chapter 1

Introduction

The objective of this research is to determine, through numerical experiments, the gas-phase dynamics of small circular pool fires. A pool fire is defined as a horizontally configured condensed fuel, the vapor from which supports a flame that burns upwardly in free convection. The combustion region is classified as a diffusion flame wherein fuel and oxidant are initially separate and must diffuse together in order for chemical reaction to occur. The pool fire fuel is typically a liquid but can be a solid. The fuel gasification rate is controlled by heat transfer from the flame to the pool surface. This coupling is an essential feature of pool fires. Thus, to fully characterize a pool fire, the heat and mass transfer coupling between the pool surface and gaseous flame region must be taken into account. In general, the mass flux rate of gasified fuel leaving the pool surface will vary with time and location depending on pool size. For small pool fires, the flux of fuel at the pool surface is approximately uniform in space with the exception at the pool edges where flame attachment occurs.[1, 26] In this work, only the region above the surface of the issuing fuel is modeled and the fuel gasification velocity at the pool surface is approximated as spatially uniform and constant in time. The fuel gasification velocity, henceforth called the 'inlet velocity', is a parameter, to be explored over the typical range of pool fire burning rates. The system configuration is one in which fuel with a constant velocity exits from a circular region as in a burner and reacts with the surrounding air. This configuration is sometimes termed a 'pool-like gas fire' in that the fuel supply rate can be controlled independently. Though heat and mass transfer dynamics at the pool surface are not modeled, the gas phase dynamics that are captured resemble that of a pool fire.[15] It follows that pool-like gas fires are described by the same model that describes the gas-phase region of true pool fires.

For pool fires, fuel issues from the pool surface with inlet velocity, ~.01 m/s, much lower than the buoyant velocity that develops in the flow (~1 m/s); thus pool fires are buoyancy controlled. This is in contrast to jets, which have a much higher inlet fuel velocity, so that momentum forces dominate. Hence, the Froude number, which is a dimensionless parameter that measures the ratio of inertial to buoyancy forces, is very low for pool fires. For small pool fires (<15 cm), the Froude number is ($\sim 10^{-4}$-10^{-2}) and the Reynolds number is $\sim 10^{1}$-10^{2}. The Froude number is defined as v_{in}^2/Dg, where v_{in} is the fuel inlet velocity, D the pool diameter, and g the gravitational acceleration. The Reynolds number is defined as $v_{in} D/ \upsilon_{in}$, where υ_{in} is the fuel inlet kinematic viscosity.

An interesting feature of circular pool fires is their pulsating nature in which periodic behavior occurs in temperature, velocity, density, and pressure fields. Several investigations obtaining measurements of these quantities show that a dominant frequency, f, occurs.[2,4,8,9,12,21,38,39,42,44] The frequency has a strong dependence on pool diameter where $f \sim D^{-0.5}$, and is a function of the gravitational acceleration, where $f \sim g^{0.5}$. The relationship, $f \sim D^{-0.5}$, has been shown to be independent of fuel type and to hold over a wide range of diameters (0.007 m – 50 m). Work done by Schonbucher et al.[39] revealed that, in addition to a dominant frequency, multiple frequencies occur throughout a fire. Furthermore, the frequency behavior of a circular pool fire is linked to the formation and shedding of vortices. Vortical structures form at the base of the fire, then rise up through the flame and dissipate. The evolution of these structures is evident by the periodic flame bulging and necking that occurs. Several experimental studies have shown a relationship to exist between vortex formation and the oscillation of temperature or pressure measurements by using time sequence imaging. [9,21,39,44] The mechanics of the formation and shedding of these vortices are still not understood.

Various theories have been proposed to explain the flickering nature of diffusion flames. Buckmaster and Peters[5], using a boundary layer approximation, proposed that flame pulsations are due to a modified Kelvin-Helmholtz instability, which arises when a

continuous variation of velocity and density occur over a finite thickness, and shear causes the flow to destabilize.[13] The analysis done by Buckmaster and Peters is restricted to very small laboratory-scale, diffusion flames (~2 mm) with Fr ≈ 100 and Re ≈ 200, and is thus not applicable to pool fires which have Froude numbers under 0.1. Their motivation for studying flames of such small diameter was to apply a similarity solution to a boundary layer description of the flame. Similarly, Yuan et al.[46] experimentally investigated the buoyant flow of helium that issued horizontally from a vertical slot. They found the velocity profile to be similar to that of a reactive buoyant jet. The buoyant acceleration induces a stratified layer between the low-density fluid of helium and the higher density ambient fluid. The velocity profile of this layer is such that the vorticity has a maximum value which causes it to roll up in a shear layer as in a Kelvin-Helmoltz type of instability. This stratified layer can be influenced by perturbations resulting from gravitational and viscous forces.

Vortex formation can also result from the misalignment of density gradients with pressure gradients, resulting in what is known as baroclinic torque. Vorticity is generated from the net pressure force not acting through the center of gravity of a volume element, thereby creating a torque.[27] Baroclinic flow can occur when density is a function of temperature, as is the case for a chemically reacting flow. Based upon phenomenological reasoning and observation of fires, the explanation of vortical structures for turbulent pool fires have been presented by Tieszen et al.[42] who state that the misalignment of pressure and density gradients exists throughout the entire flow field to provide a source of vorticity. The greatest vorticity generation occurs where the spatial separation between hot and cold gases is the smallest. This would arise in the horizontal direction, perpendicular to the flame sheet, where hot gases meet the ambient air. This density gradient is misaligned with the vertical pressure gradient that exists as the hydrostatic pressure field due to the gravitational force.

Cetegen and Kasper[11] have argued that reacting and non-reacting buoyant flows have an inherent instability caused by density stratification. They state that there can exist a region of Rayleigh-Taylor instability and perturbations from gravitational forces can rapidly amplify the instability. A Rayleigh-Taylor instability can occur when a region of higher density fluid occurs on top of a lower density fluid in a gravitational field.[13] Jiang and Luo[24] concluded that a radial density gradient under the influence of gravity plays a major role in vortex formation.

Thus, the basic mechanisms for vortex formation include: that due to shear, as in a Kelvin-Helmoltz instability; that due to baroclinic torque; that due to radial density gradients under the influence of gravity; and that due to density inversion, as in a Rayleigh-Taylor instability. Yet to be determined is the relative contribution of these mechanisms for highly buoyant, low-speed diffusion flames. It is the intent of this work to isolate the individual role that each of these mechanisms contributes to vortex formation and to determine the frequency response of the flame at various locations. The above is investigated as dependent upon fuel inlet velocity and pool diameter. Thus, a parametric study is performed by varying the Froude and Reynolds number.

Fuel characteristics such as heat release rate, stoichiometric air-fuel ratio, and fuel molecular weight can influence flame behavior. Thus, the aforementioned vortex formation mechanisms and frequency response is investigated by varying fuel molecular weight, stoichiometric air-fuel ratios, and heat release rates. Definitions and discussion of these fuel parameters are provided in Chapter 6.

In this work, the flow field is modeled as being axisymmetric. There are two motivations for utilizing such a model. First, observations of experiments indicate that laminar pool fires are essentially axisymmetric up to elevations of several diameters, depending on pool size. Secondly, this model allows for a lower computational run time, so that many more runs can be performed as required for investigation of the

aforementioned effects. For any given pool diameter, the elevation up to which an axisymmetric model can be applied is uncertain. As elevation is increased, circumferential instabilities eventually occur and the flow is no longer axisymmetric. Thus, a further objective of this work is to estimate, for a particular diameter, the elevation for which an axisymmetric model is valid. This is accomplished by determining a local Reynolds number at any given elevation. This concept is analogous to the transition criteria for the free convection flow of a heated vertical plate, wherein a local Grashof number between 10^8 and 10^9 is the critical range for transition.[18] The Grashof number is a dimensionless group representing the ratio of buoyancy to viscous forces. Since the local Grashof number is a function of the vertical distance along the plate, this critical range of values implies an approximate height to which a boundary layer analysis is valid.

One way to gain understanding of the dynamics of pool fires is to solve the full governing conservation and chemical kinetic equations, namely through the Navier-Stokes equations for ideal gases along with the conservation of species equations which include the effects of chemical kinetics. Due to the limitations of present day computers and to the time and length scales that need to be resolved in pool fires, a direct time-dependent, three dimensional simulation is not practical for the range of Froude and Reynolds numbers under investigation. The simulation must span length scales of roughly three orders of magnitude, that is, from the combustion zone, which is on the order of a millimeter, up to several pool diameters. Simplifications must be introduced to focus on the dominant effects. Thus, an axisymmetric simulation with a simplified combustion model is used. The use of this facilitates a larger number of runs as necessary to accomplish a parametric study. Though only small pool fires are considered, the model and methodology used could be extended to larger pool fires in the near future when computing power allows a three-dimensional simulation in a reasonable length of run time. It is then that circumferential instabilities can be investigated. The intent of the present work is to utilize the full potential of an axisymmetric model.

In this work, the coupled, time-dependent equations are solved numerically in axisymmetric coordinates using an explicit, projection based algorithm. A finite volume formulation on a staggered grid is used. The approach is to focus on the fluid dynamics of the fire rather than its chemical kinetics since non-chemical effects are responsible for the formation of vortices that control entrainment and stability behavior. Thus, a single-step, irreversible, reaction model with infinitely fast chemistry is used. Furthermore, radiation modeling is not included. Additional simplifications include: the use of the low Mach number approximation[35], thin flame sheet approximation[6], and a Lewis number of unity. Justification and discussion of these approximations will be given in following sections.

1.1 Objectives

Numerical experiments are performed on laminar, gas-phase, circular pool fires with the following specific goals:

- To determine the relative contributions to vortex formation of the following: baroclinic torque, radial density gradients in a gravitational field, stratified shear layers, and density inversion.
- To determine the multiple frequency response at various locations.
- To perform a parametric study of the vortex formation mechanisms and frequency response as dependent upon the source Reynolds and Froude number.
- To determine the influence of fuel molecular weight, air-fuel ratio, and heat release rates on vortex formation mechanisms and frequency response.
- To estimate the pool diameter limit for which an axisymmetric model can be applied by identifying and interpreting a local Reynolds number.

1.2 Organization

Chapter 2, Background: Previous research on pool fires by other investigators is presented.

Chapter 3, Mathematical Model: In this chapter the major assumptions are discussed. The governing equations are stated with the low Mach number approximation, and a detailed statement of the problem is made.

Chapter 4, Numerical Model: In this chapter the numerical model is discussed in detail, and numerical boundary conditions are given.

Chapter 5, Model Validation: In this chapter the mathematical model is compared with experiments done by other researchers.

Chapter 6, Results and Discussion: In this chapter the results are presented and discussed.

Chapter 7, Conclusions: In this chapter a summary and implications of the results, and recommendations for future work is presented.

Chapter 2

Background

The purpose of this chapter is to provide background for the current research, and to elucidate some features of pool fires, primarily their pulsating nature and the mechanics of vortical structures. Previous experimental and numerical research done on the pulsating nature of pool fires and on the mechanisms involved in the formation of vortical structures is presented.

2.1 Previous Experimental Research on Pulsation Frequency of Pool Fires

The first major experimental investigation of pool fires was by Blinov and Khudyakov.[4] They performed experiments on pool fires ranging is size from 1.1 cm to 30 m for several liquid fuels. Flame structure was strongly dependent on pool diameter. A Reynolds number for these experiments, as interpreted by Hottel,[23] is based upon the gaseous burning velocity of the fuel, pool diameter, and viscosity of the cold or non-burning fuel vapor. For pool diameters approximately 5 cm or less the visible flame was laminar (Re<20), for diameters between 5 cm and 1 m it was in transition (Re~ 20-200), and for diameter greater than 1 m it was in the turbulent regime (Re>200). From a diameter around 1.1 cm the structure of the flame is steady and conical until at around 3 cm it exhibits a pulsating tip which has a maximum frequency of about 18-20 Hz. A further increase in diameter causes the pulsating portion of the flame to shift downward and the frequency to decrease. The burning rate was found to depend on pool diameter. For the laminar regime the burning rate decreases as a function of pool diameter, and from the transition to turbulent regime it increases, until it reaches a constant value independent of pool diameter.

By measuring time-traces of velocity, pressure, and temperature near the base of pool fires, Hamins et. al.,[21] obtained the pulsation frequency of several gaseous and liquid fuels, over a wide range of burner diameters (0.0074 m ~ 0.30 m), Froude number (10^{-4}~10^{3}), Reynolds number (10~10^{3}), both based on burner diameter, inlet fuel velocity and properties. They investigated the effects of varying the heat release rate, fuel exit velocity and burner diameter on the pulsation frequency of flames. They found that there is a minimum critical fuel flow rate needed to initiate pulsations. This minimum critical velocity is dependent on fuel type and diameter, approximately $D^{-1.5}$. They also found that the higher the exit velocity, the closer that vortical structures are to the pool surface. Pulsation frequency is weakly dependent on fuel exit velocity. The heat release rate was varied through nitrogen dilution of the fuel stream. The authors point out that nitrogen dilution changes the stoichiometry, adiabatic flame temperature, oxygen demand, total air entrainment, and density distribution of the flow field. The heat release rate did not have an effect on the pulsation frequency. For all fuels tested the Strouhal number ($=f\,D/v_e$) was found to be inversely proportional to the Froude number. A best-fit power law to all of the data gave $Str \sim Fr^{-0.57}$. Isothermal helium plumes were also tested and the relationship $Str \sim Fr^{-0.38}$ was found. The authors conclude that due to the difference in the Strouhal-Froude relationship between the reacting and non-reacting flows that entrainment and vorticity cannot be modeled through studies of isothermal buoyant flows such as helium. This is due to the steep density gradients present in reacting flows, whereas non-reacting flows have more of a Gaussian density distribution.

Cetegen and Ahmed[9] investigated the periodic oscillations of pool fires by conducting a series of experiments on 0.1 and 0.3 m diameter propane fires and non-reacting helium plumes. Pressure fluctuations were synchronized with video recordings, temperature, and velocity measurements at the pool surface. The effect of changes in heat release, by way of fuel dilution with CO_2, was also investigated. A decrease in heat release causes the intensity of the pressure fluctuations at the pool surface to decrease, but does not effect the frequency. Helium plumes similarly display a "puffing" frequency,

scaling with $D^{-0.5}$. This suggests that the puffing phenomenon is associated with instabilities of a buoyant flow. The results for the propane pool fires indicate that periodic formation and shedding of vortices occurs. They form a short distance above the pool surface, within one diameter, and are thought to be responsible for the periodic nature of pool fires. The puffing frequency for pool fires was found to scale as $D^{-0.5}$.

Weckman and Sobiesiak[44] took detailed velocity and temperature measurements on a 30 cm acetone pool fire by using laser Doppler anemometry and thermocouples. They found that large-scale structures develop with a frequency dependent on pool diameter. These structures originate at the base of the fire as vortices that rise up to converge to form a large plume that is shed. The authors describe these structures to be formed in two stages. There is first a well-ordered flame composed of a series of vertical ribs connected by curved flame sheets to form channels. At this stage a vortex ring outside the base of the fire develops. In the second stage this vortex ring pulls up the flame sheet to form an initial instability that amplifies and travels to the centerline to create vortices. These vortices then accelerate upward and break down to form a large-scale structure that expands. With this expansion a narrow flame base is once again formed. The authors point out that a consistent explanation is needed for the processes that cause the formation of these large-scale structures and how their behavior is related to entrainment and mixing.

Cetegen and Dong[10], performing experiments on propane diffusion flames of diameters 2.5 to 10.2 centimeters, showed that two modes of instabilities occur, the sinuous mode and varicose mode. The sinuous mode of instability is characterized by a vortex ring becoming tilted and causing a wave-like appearance to the flame. This type of instability first begins in the contracting region of the flame, then fully develops significantly downstream of the fuel surface. The varicose mode is characterized by a vortex ring, which remains horizontal as it travels upward through the flame, and is responsible for the flame height fluctuations. This type of instability develops very near

the pool surface. The probability of observing the varicose mode increases with increasing Richardson number, or equivalently inverse Froude number ($g\ D/v_e^2$).

Davis et al.[17] conducted a numerical and experimental investigation on low-speed buoyant jet of propane diluted with 50% nitrogen. They found that buoyancy-induced, counter rotating vortical structures form to cause bulging and necking of the flame as well as flickering. It was also found that with zero gravity the flow does not develop vortical structures, but results in a steady flame with no flickering.

Schonbucher et al.[39] performed experiments on pool fires of several different fuels for diameters ranging from 1 cm to 10 cm. Using real-time, holographic, interferometry they found organized structures, which they termed 'density parcels'. These structures depend on the height above the pool surface, pool diameter, fuel supply rate, equivalence ratio, and fuel type. They also display mono-, quasi- and non-periodic behavior. Mono-periodic behavior is defined as the occurrence of a fundamental frequency along with frequencies that are multiples of the fundamental frequency, also termed harmonic. Quasi-periodic behavior results in independent frequencies that are not multiples of a fundamental frequency. Non-periodic behavior occurs in convection velocities, refractive indices, mass densities, and temperatures. The mechanisms of origin of 'density parcels' is unknown, but the authors believe that they are influenced both by hydrodynamic and combustion-generated instabilities. Harmonics are found in lower elevations, approximately two diameters and under, while independent frequencies occur in higher elevations.

2.2 Previous Numerical Work

Jiang and Luo[24] performed a numerical simulation of a buoyant diffusion flame to determine the dependence of vorticity generation on Froude number. They found that buoyancy induced effects due to the interaction between gravity and radial density

gradients are the dominant mode of vorticity generation and oscillation of the flame. The Froude number range used (0.2 – ∞ (g=0)) corresponds to a low-speed, buoyant jet, rather than to Froude numbers for pool fires (Fr ~ 10^{-5} – 10^{-2}).

Ghoniem et al.[20] performed a numerical simulation of an axisymmetric fire plume (Fr=.04, Re=200) in order to determine the source of vorticity generation. The results indicate that the origin of the instability is due to radial density gradients between the fire plume and air. A shear layer exits in this region so that a Kelvin-Helmoltz type of instability occurs. This instability begins very close to the pool surface, within a pool radius. They found that non-reacting and reacting plumes have similar density fields close to the pool surface, which results in similar puffing characteristics.

Mell et al.[31] performed a numerical simulation of a 10-cm-diameter methanol pool fire in an enclosure. The numerical model was based upon axial symmetry, the low Mach number approximation, and a mixture-fraction formulation. The results agreed well with experiment for heights one diameter above the pool surface, but not for heights greater than this. They attribute the disagreement to the assumption of axial symmetry. Simulations were also performed with and without baroclinic torque. When the baroclinic term was removed the pulsation frequency increased and the onset of oscillations was delayed.

Lee and Baek[28] numerically simulated ethylene pool fires of 0.02, 0.05, and 0.10 m in diameter. The pool fire was modeled using the geometry of coaxial cylinders in which fuel exits the inner cylinder and oxidant the outer. Infinitely fast chemistry and axial symmetry were assumed. Soot formation was also included in the model. The oscillation frequency for each diameter agreed with experimental results from other researchers, and the periodic formation of large-scale vortical structures was captured. The authors conclude that changes in diameter effects flow dynamics.

Kuldeep et al.[26] numerically simulated a 1-cm-diameter methanol pool fire. The fire was modeled in two-dimensional Cartesian coordinates and a single-step chemical reaction was assumed. The liquid phase was also taken into account to capture the burning rate. The numerical results were compared to the experimental results of a slot burner. They compared favorably for puffing frequency, temperature, and burning rate. The simulations were performed with varying speeds of co-flowing oxidant. For air velocities of 2 and 10 cm/s the flame was unsteady, while for velocities of 20 and 40 cm/s the flame became steady. The authors conclude that increasing the air co-flow velocity stabilizes the flame by pushing the vortices away from the flame region. Increasing the co-flow velocity also resulted in an increase in the burning rate. The results indicate that the burning rate is significantly higher at the burner edge than at the pool center.

The aforementioned experimental work on pool fires provide much information on flame structure and periodic behavior, as well as the effect of various parameters such as heat release rate, fuel exit velocity, and ambient conditions for many different fuels and for a large range of Froude number. Laboratory experimental work has the advantage of observing a large range of Froude and Reynolds number, but has the disadvantage that quantities such as vorticity production terms are difficult to measure. Numerical experiments offer the advantage that these quantities can be obtained. The approach of the current work is to use direct numerical simulation on small pool fires to capture quantities that would be difficult or impossible to obtain in the laboratory. The quantities of interest as previously specified in Chapter 1 have yet to be obtained for pool fires for the Froude and Reynolds number range specified either experimentally or numerically. The aforementioned bodies of numerical work have focused on larger Froude numbers, thus less buoyant flows that do not reflect the behavior of the gas-phase of pool fires, and/or they have not obtained the vortex generation mechanisms of present interest for a parametric study. Nor has a local Reynolds number been formulated for pool fires. Thus, the intent of this work is to extent the current knowledge of pool fires by examining a

lower range of Froude number and to capture the vortex generation mechanisms previously mentioned, as well as formulate a local Reynolds number.

Chapter 3

Mathematical Model

In this chapter the major assumptions and equations used to describe the gas-phase region of a pool fire are specified. The equations include the conservation of mass and momentum for gaseous mixtures along with a mixture fraction equation. The low Mach number approximation is used and the appropriate equations assuming such an approximation are derived.

3.1 Problem Statement

This work is concerned with the gas phase dynamics of pool fires, which are highly buoyant (Fr ~ 10^{-4} – 10^{-2}), and have Reynolds numbers in the range of (~ 10^{1} - 10^{2}). Fuel issues from a circular, horizontal surface with a uniform velocity to react with the surrounding, initially quiescent, air. This geometry allows for comparison with experiments done by other researchers, and offers simplicity in that the flame can be modeled as being axisymmetric. For the diameters considered, the visible flame is in the laminar to transitional region of the flow field. The ignition of fuel and air is not considered in this work and thus is not modeled. Also, the region of interest is above the fuel surface, thus heat feedback dynamics are not considered.

Major assumptions include:

1. The flame chemistry is represented by a single-step, irreversible reaction.
2. Fast chemistry in which the reaction takes place in an infinitely thin flame-sheet.
3. A unity Lewis number.
4. The effect of soot formation is negligible.

5. Radiation is not modeled and is considered to be a secondary mode of heat transfer for the size of pool fires considered.
6. The low Mach number approximation.
7. Axial symmetry of the flow field

The working equations along with the initial and boundary conditions are collected at the end of this chapter.

3.2 Governing Equations for a Reacting Flow

For a reacting flow the conservation of mass, momentum, and species along with an equation of state for mixtures must be invoked to completely describe the velocity, pressure, species, and temperature fields.[6] The following differential forms of the equations assume an Eulerian frame of reference in which quantities are evaluated at a fixed point over time. The mixture is made up of N fluids, each having a velocity. These velocities are mass averaged to obtain a mixture velocity, defined as

$$\mathbf{v} = \sum_{i=1}^{N} Y_i \mathbf{v}_i, \tag{3.1}$$

where the Y_i are mass fractions with

$$\sum_{i=1}^{N} Y_i = 1 \tag{3.2}$$

The separate densities are defined as $\rho_i = \rho Y_i$, where ρ is the density of the mixture. The conservation of mass for individual species is

$$\frac{\partial(\rho Y_i)}{\partial t} + \nabla \cdot (\rho Y_i \mathbf{v}_i) = \dot{\omega}_i, \tag{3.3}$$

where $\dot{\omega}_i$ is the production rate of specie i in units of mass per unit volume per unit time. Summing over all species gives

$$\sum_{i=1}^{N} \dot{\omega}_i = 0 \tag{3.4}$$

Summing equation (3.3) over all species and using equations (3.1), (3.2), and (3.4) results in the continuity equation.

$$\frac{\partial \rho}{\partial t} + \nabla \cdot (\rho \mathbf{v}) = 0 \tag{3.5}$$

To determine the mass flux of species relative to the surface moving with the mass average velocity, the diffusion velocity is defined,

$$\mathbf{V}_i = \mathbf{v}_i - \mathbf{v}. \tag{3.6}$$

Note that $\sum_{i=1}^{N} Y_i \mathbf{V}_i = 0$, which follows from equation (3.1), (3.2), and (3.6). Using (3.6) and (3.5), (3.3) may be written as

$$\rho \frac{\partial Y_i}{\partial t} + \rho \mathbf{v} \cdot \nabla Y_i = \dot{\omega}_i - \nabla \cdot (\rho Y_i \mathbf{V}_i). \tag{3.7}$$

Equation (3.7) accounts for preferential diffusion, in which the diffusion of a species into all other specie of the system is included. In this work D_{ij} is approximated by making all binary diffusion coefficients equal for each side of the flame sheet, which simplifies equation (3.7). This approximation is only valid when the molecular weights of the species are all on the same order. For fuels considered in this work this condition is approximately satisfied.

Using Fick's Law,

$$Y_i \mathbf{V}_i = -\sum_{j=1}^{N} D_{ij} \nabla Y_j \tag{3.8}$$

where D_{ij} is the diffusion coefficient, equation (3.7) may be written as,

$$\rho \frac{\partial Y_i}{\partial t} + \rho \mathbf{v} \cdot \nabla Y_i = \dot{\omega}_i + \nabla \cdot (\rho D \nabla Y_i) \tag{3.9}$$

The differential form of the conservation of momentum is expressed by the Navier-Stokes equations for a viscous, compressible fluid using the mixture velocity.

$$\frac{\partial(\rho \mathbf{v})}{\partial t} + \nabla \cdot (\rho \mathbf{v}\mathbf{v}) = -\nabla p + \nabla \cdot \mathbf{T} + \rho \mathbf{g}, \tag{3.10}$$

where **g** is the average body force per unit mass, and

$$\mathbf{T} = -\frac{2}{3}(\mu \nabla \cdot \mathbf{v})\mathbf{I} + \mu\left[\nabla \mathbf{v} + (\nabla \mathbf{v})^T\right]$$

I is the unit tensor and μ is the dynamic viscosity.

The differential form of the conservation of energy equation is expressed as the following.

$$\rho c_p \frac{\partial T}{\partial t} + \rho c_p \mathbf{v} \cdot \nabla T = \nabla \cdot (\kappa \nabla T) + Q \dot{\omega}_F \tag{3.11}$$

where κ is the mixture thermal conductivity and,

$$Q = h_F^\circ MW_F \nu_F + h_O^\circ MW_O \nu_O - h_P^\circ MW_P \nu_P$$

The h_i are the standard heat of formation of species i, suffix F denotes fuel, O denotes oxidant, P denotes products, MW molecular weight, and ν_i the stoichiometric coefficient for species i.

The equation of state is the ideal gas equation for mixtures:

$$p = \rho RT \sum_{i=1}^{N} \frac{Y_i}{MW_i}, \tag{3.12}$$

where the MW_i are molecular weights, R is the universal gas constant, T the absolute temperature, and p the thermodynamic pressure.

3.3 Global, one-step reaction model

In this work elementary reactions are ignored since their inclusion would have negligible impact on the fluid dynamics.[14,25] Capturing the heat release from the overall chemical reaction is what is essential in modeling a buoyancy dominated flow. This simplifies the problem to make it much more tractable. Thus, a global, single-step reaction model is used and the chemical reaction is represented as a fuel mixture combining with an oxidant mixture in stoichiometric proportions to form products, that is,

$$1 \text{ mass of fuel} + \lambda \text{ mass of oxidant} \rightarrow (\lambda + 1) \text{ mass of products}$$

where λ is the stoichiometric ratio of oxidant to fuel by mass, that is

$$\lambda = \frac{\nu_0 MW_O}{\nu_F MW_F}. \tag{3.13}$$

The reaction rates are then related by:

$$\dot{\omega}_F = \frac{1}{\lambda}\dot{\omega}_O = -\frac{1}{\lambda+1}\dot{\omega}_{products} \tag{3.14}$$

Then using (3.9) and (3.14), specie equations can be written as,

$$\rho\frac{\partial Y_F}{\partial t} + \rho\mathbf{v}\cdot\nabla Y_F = \nabla\cdot(\rho D\nabla Y_F) + \dot{\omega}_F \tag{3.15}$$

$$\rho\frac{\partial Y_O}{\partial t} + \rho\mathbf{v}\cdot\nabla Y_O = \nabla\cdot(\rho D\nabla Y_O) + \lambda\dot{\omega}_F \tag{3.16}$$

$$\rho\frac{\partial Y_P}{\partial t} + \rho\mathbf{v}\cdot\nabla Y_P = \nabla\cdot(\rho D\nabla Y_P) - (\lambda+1)\dot{\omega}_F \tag{3.17}$$

An equation may now be formed which is independent of a chemical source term. By multiplying equation (3.15) by λ and subtracting equation (3.16) the following equation results:

$$\rho\frac{\partial \beta}{\partial t} + \rho\mathbf{v}\cdot\nabla\beta = \nabla\cdot(\rho D\nabla\beta) \tag{3.18}$$

where,

$$\beta = \lambda Y_F - Y_O. \tag{3.19}$$

The variable β is a conserved scalar, that is, it is independent of chemical reaction, and is known as a Schwab-Zeldovich variable. Similarly, another Schwab-Zeldovich variable can be formed by using equations (3.11) and (3.17).

$$\gamma = T - \frac{Q/c_p}{1+\lambda} Y_p \tag{3.20}$$

where c_p is the mixture specific heat at constant pressure,

$$c_p = \sum_{i=1}^{N} Y_i c_{pi}$$

This variable also obeys equation (3.18).

The fast-chemistry limit in which the Damkohler number approaches an infinite value is also assumed. The Damkohler number is defined as the ratio of mixing time to chemical reaction time.[5] In this limit chemical reaction occurs many orders of magnitude faster than the time needed for mixing. Instantaneous reaction occurs when fuel and oxidant come in contact. The chemical reaction is then confined to an infinitesimally thin flame surface that separates fuel and oxidant with implications that fuel and oxidant cannot coexist, that is,

$$Y_F Y_O = 0 \tag{3.21}$$

The mixture fraction Z, a normalized variable that is defined in terms of β, may be utilized.

$$Z = \frac{\beta - \beta_O}{\beta_F - \beta_O} = \frac{[\lambda Y_F - Y_O] - [\lambda Y_F - Y_O]_O}{[\lambda Y_F - Y_O]_F - [\lambda Y_F - Y_O]_O} \tag{3.22}$$

where the suffix F and O, respectively, denote streams of fuel mixture and oxidant mixture, as prescribed. The equations are the same if the stream of fuel is pure and if the stream of oxidant is pure, as opposed to a mixture. Thus, in what follows each stream will be denoted as pure, though it is allowable for the streams to be comprised of a mixture.

In the pure fuel stream

$$Y_O = 0,\ Y_F = Y_F^\infty = 1, \tag{3.23}$$

and in the pure oxidant stream

$$Y_F = 0,\ Y_O = Y_O^\infty \tag{3.24}$$

Using (3.23) and (3.24) equation (3.22) reduces to

$$Z = \frac{\lambda Y_F - Y_O + Y_O^\infty}{\lambda + Y_O^\infty}, \qquad 0 \le Z \le 1 \tag{3.25}$$

The mixture fraction is linearly related to β, thus it is a conserved scalar and also obeys the transport equation.

$$\rho\frac{\partial Z}{\partial t} + \rho \mathbf{v} \cdot \nabla Z = \nabla \cdot (\rho D \nabla Z) \tag{3.26}$$

At the flame sheet neither fuel or oxygen is present and z is defined there as:

$$Z_{st} = \frac{Y_O^\infty}{\lambda + Y_O^\infty} \tag{3.27}$$

This defines the location of the flame sheet were chemical reaction takes place, and the boundary that separates fuel and oxygen. The flame sheet acts as the source of products and a sink for fuel and oxidant. Thus,

$$z = \frac{-Y_O + Y_O^\infty}{\lambda + Y_O^\infty} \qquad 0 \le Z \le Z_{st}, \quad Y_F = 0 \tag{3.28}$$

$$z = \frac{\lambda Y_F + Y_O^\infty}{\lambda + Y_O^\infty} \qquad Z_{st} \le Z \le 1, \quad Y_O = 0 \tag{3.29}$$

Using equations (3.27-3.29), mass fractions for fuel and oxygen can be obtained.

$$Y_F = \frac{Z - Z_{st}}{1 - Z_{st}}, \qquad Z_{st} \le Z \le 1, \quad Y_O = 0 \tag{3.30}$$

$$Y_O = \frac{Z_{st} - Z}{Z_{st}} Y_O^\infty, \qquad 0 \le Z \le Z_{st}, \quad Y_F = 0 \tag{3.31}$$

The mass fraction for the inert species nitrogen is obtained by the linear relationship

$$Y_{N_2} = Y_{N_2}^\infty (1 - Z), \tag{3.32}$$

and using equation (3.2), the mass fraction of products,

$$Y_P = 1 - (Y_F - Y_O - Y_{N_2}) \tag{3.33}$$

The mass fraction of individual species in the products is obtained by

$$Y_j = Y_P \frac{(MW_j)(\nu_j)}{\sum_{i=1}^{M} (MW_i)(\nu_i)}, \tag{3.34}$$

where the summation is over M product species.

Similarly the variable, γ, can be linearly related to the mixture fraction by

$$Z = \frac{\gamma - \gamma_O}{\gamma_F - \gamma_O} = \frac{\left[T - \frac{Q/C_P}{1+\lambda} Y_P\right] - \left[T - \frac{Q/C_P}{1+\lambda} Y_P\right]_O}{\left[T - \frac{Q/C_P}{1+\lambda} Y_P\right]_F - \left[T - \frac{Q/C_P}{1+\lambda} Y_P\right]_O} \tag{3.35}$$

In the pure fuel stream and the pure oxidant stream $Y_p = 0$, thus equation (3.35) becomes

$$Z = \frac{\left[T - \frac{Q/C_P}{1+\lambda} Y_P\right] - T_O}{T_F - T_O} \tag{3.36}$$

The temperature field can now be expressed in terms of Z by equation (3.36).

$$T = T_O + \frac{Q/c_p}{1+\lambda} Y_p + (T_F - T_O)Z \tag{3.37}$$

The mixture fraction formulation allows a single transport equation to be solved instead of N-1 specie equations. This has the advantage of providing a substantial reduction in computational effort, while allowing the essential physics to be captured. Once the mixture fraction is known the temperature field can be solved for and, using the ideal gas equation, the density field can then be obtained.

A detailed approach to modeling radiation is not adopted in this work. Approximately 15% of the heat generated from a 8.3 cm methane pool fire is lost due to

radiation to the surroundings.[7] For smaller diameters such as .5 cm this fraction reduces to .1. This fraction can change not only with diameter, but also with fuel type. Fuels that have high soot production will have a larger fraction of heat lost to the surroundings than fuels with low soot production. Furthermore, the fraction of radiation to the pool surface is also secondary compared to convection for the diameters considered. For very small pool fires (D~0.01 m), conduction dominates the heat feedback to the pool surface, whereas for diameters up to 0.1 meters convection dominates.[23] For diameters greater than 0.5 meters radiation then becomes the leading mode of heat transfer. For diameters and fuels considered in this work, radiation is not the dominant mode of heat transfer.

Temperature-dependent transport properties are modeled with the Chapman-Enskog theory and the Lennard-Jones potentials for the viscosity and binary diffusion coefficients.[36] The mixture viscosity is determined using the formula by Wilke.[45] On the fuel side of the flame sheet all species are assumed to have the binary diffusion coefficient of fuel and nitrogen, and on the other side of the flame sheet that of oxygen and nitrogen. Thus, fuel and oxidizer are allowed to diffuse at different rates.

3.4 Low Mach Number Approximation

The diffusion flames considered have a very low Mach number (< 0.1). Thus, the low Mach number approximation, which is a non-singular, perturbation approach, can be applied.[35] The advantage of such an approximation is that the characteristic time scale comes either from chemical reaction, diffusion, or convection times, rather than acoustic times. For flows such as in noise generation systems, acoustic wave time scales must be resolved, which is computationally expensive. This approximation allows the elimination of these acoustic waves, but the resulting equations still allow for large density variation that occur in reacting flows. The pertinent equations to consider include equations (3.5), (3.10), (3.12), (3.26), (3.30-3.34), and (3.37). These equations are nondimensionalized by the scales:

v_{in} - Inlet fuel velocity

D - Pool diameter

ρ_{in} - Inlet fuel density

T^{∞} - Ambient temperature

c_p^{∞} - Ambient specific heat at constant pressure

c_v^{∞} - Ambient specific heat at constant volume

μ_{in} - Inlet fuel viscosity

D_{ij}^{∞} - Ambient binary diffusion coefficient

Pressure is scaled by $\rho_{in} R_{air} T^{\infty}$. Equations (3.5), (3.10), (3.12), and (3.26) then become

$$\frac{\partial \rho}{\partial t} + \nabla \cdot (\rho \mathbf{v}) = 0 \tag{3.38}$$

$$\frac{\partial (\rho \mathbf{v})}{\partial t} + \nabla \cdot (\rho \mathbf{v}\mathbf{v}) = -\frac{1}{\gamma Ma^2} \nabla p + \frac{1}{Re} \nabla \cdot \mathbf{T} + \frac{1}{Fr} \rho \mathbf{g} \tag{3.39}$$

$$\rho \frac{\partial Z}{\partial t} + \rho \mathbf{v} \cdot \nabla Z = \frac{1}{Re\, Sc} \nabla \cdot (\rho D \nabla Z) \tag{3.40}$$

$$p = \rho T \tag{3.41}$$

where the dimensionless parameters are defined as

$$Re = \frac{\rho_{in} v_{in} D}{\mu_{in}}, \quad Fr = \frac{v_{in}^2}{Dg}, \quad \gamma = \frac{c_p^{\infty}}{c_v^{\infty}}, \quad Ma^2 = \frac{v_{in}^2}{\gamma R T^{\infty}}, \quad Sc = \frac{\mu_{in}}{\rho_{in} D}$$

Since the Mach number is small, so is the term γMa^2. Thus, let

$$\varepsilon = \gamma Ma^2 \tag{3.42}$$

All variables can be expanded in powers of ε in the form

$$\mathbf{v} = \mathbf{v}^{(0)} + \varepsilon \mathbf{v}^{(1)} + \varepsilon^2 \mathbf{v}^{(2)} \ldots$$

and substituted into equations (3.34-3.37). Equating zeroth order terms the following equations are obtained.

$$\frac{\partial \rho^{(0)}}{\partial t} + \nabla \cdot (\rho^{(0)} \mathbf{v}^{(0)}) = 0 \tag{3.43}$$

$$\nabla p^{(0)} = 0 \tag{3.44}$$

$$\frac{\partial (\rho^{(0)} \mathbf{v}^{(0)})}{\partial t} + \nabla \cdot (\rho^{(0)} \mathbf{v}^{(0)} \mathbf{v}^{(0)}) = -\nabla p^{(1)} + \frac{1}{Re} \nabla \cdot \mathbf{T}^{(0)} + \frac{1}{Fr} \rho^{(0)} \mathbf{g}^{(0)} \tag{3.45}$$

$$\rho^{(0)} \frac{\partial Z}{\partial t} + \rho^{(0)} \mathbf{v}^{(0)} \cdot \nabla Z = \frac{1}{Re\, Sc} \nabla \cdot (\rho^{(0)} D^{(0)} \nabla Z) \tag{3.46}$$

$$p^{(0)} = \rho^{(0)} T^{(0)} \tag{3.47}$$

Equation (3.44) states that the zeroth order term for pressure is constant. This term is called the ambient or thermodynamic pressure. Only small pressure perturbations from the ambient pressure are significant in the momentum equation. This approximation removes the acoustic waves by not allowing variations in pressure to cause changes in density as is evident by equation (3.47). Thus, these equations are incompressible, but they still allow variation in density caused by chemical heat release.

3.5 Working Equations

The following provide the working equations assuming a low Mach number approximation. Due to the near symmetric behavior of the flow field the equations are solved in cylindrical coordinates in two dimensions. Thus, only variations in the (r,z) directions are considered, where r and z are the radial and axial directions respectively. In the following conditions and equations, all variables refer to the zeroth order terms in eqns 3.43 – 3.47, except for pressure, which refers a first order kinematic pressure.

Initial conditions (t = 0):

$$\left.\begin{aligned} v_z &= 0 \\ v_r &= 0 \\ T &= T^{\infty} \\ \rho &= \rho^{\infty} \\ p &= 0 \\ Z &= 0 \end{aligned}\right\} \begin{aligned} &0 < z < \infty \\ &0 < r < \infty \end{aligned}$$

Boundary conditions:

For the boundary condition at z = 0, conditions for two different cases are specified, no co-flow and co-flow. A co-flow configuration is co-annular cylinders with the inner cylinder issuing fuel and the outer cylinder issuing air. Two simulations performed in Chapter 5 for model validation have a co-flow condition. These two cases have the outer cylinder extending up to 20 diameters axially, acting as a shield against disturbances. Thus, different boundary conditions apply for this configuration at the shield boundary than for the case with no co-flow. All other simulations in this work are performed without co-flow. Conditions at all other boundaries are the same for both cases.

The boundary condition at z = 0 for no co-flow is the following:

$$
\left.\begin{array}{l}
\left.\begin{array}{l} v_z = v_{in} \\ v_r = 0 \\ Z = 1 \\ T = T_{in} \\ \rho = \rho_{in} \\ p = 0 \end{array}\right\} 0 \le r \le D \\
\left.\begin{array}{l} v_z = 0 \\ v_r = 0 \\ \dfrac{\partial Z}{\partial z} = 0 \\ \dfrac{\partial T}{\partial z} = 0 \\ \dfrac{\partial \rho}{\partial z} = 0 \\ p = 0 \end{array}\right\} D < r \le \infty
\end{array}\right\} z = 0,\ t > 0
$$

The boundary condition at z = 0 for co-flow is the following:

$$
\left.\begin{array}{l}
\left.\begin{array}{l} v_z = v_{in} \\ v_r = 0 \\ Z = 1 \\ T = T_{in} \\ \rho = \rho_{in} \\ p = 0 \end{array}\right\} 0 \le r \le r_{inner} \\
\left.\begin{array}{l} v_z = v_{in_{air}} \\ v_r = 0 \\ Z = 0 \\ T = T_{in\,air} \\ \rho = \rho_{in_{air}} \\ p = 0 \end{array}\right\} r_{inner} < r \le r_{outer}
\end{array}\right\} z = 0,\ t > 0
$$

$$\left.\begin{aligned} v_z &= 0 \\ v_r &= 0 \\ Z &= 0 \\ T &= T^{\infty} \\ \rho &= \rho^{\infty} \\ p &= 0 \end{aligned}\right\} z = \infty,\ t > 0$$

$$\left.\begin{aligned} \frac{\partial v_z}{\partial r} &= 0 \\ v_r &= 0 \\ \frac{\partial Z}{\partial r} &= 0 \\ \frac{\partial T}{\partial r} &= 0 \\ \frac{\partial \rho}{\partial r} &= 0 \\ \frac{\partial p}{\partial r} &= 0 \end{aligned}\right\} r = 0,\ t > 0$$

The boundary condition at $r = \infty$ for no co-flow is the following:

$$\left.\begin{aligned} v_z &= 0 \\ v_r &= 0 \\ Z &= 0 \\ T &= T^{\infty} \\ \rho &= \rho^{\infty} \\ p &= 0 \end{aligned}\right\} r = \infty,\ t > 0$$

The boundary condition for co-flow at $r = r_{outer}$ with the outer cylinder extending axially to act as a shield is the following:

$$\left.\begin{aligned} v_z &= 0 \\ v_r &= 0 \\ \frac{\partial Z}{\partial r} &= 0 \\ T &= T^{\infty} \\ \rho &= \rho^{\infty} \\ p &= 0 \end{aligned}\right\} r = r_{outer},\ t > 0$$

Note that the radius of the outer cylinder shield is much larger than the inner cylinder radius, by approximately 5 diameters. Thus, at $r = r_{outer}$ the temperature and density remain that of ambient.

The ∇ operator is defined as

$$\nabla \equiv \frac{1}{r}\frac{\partial}{\partial r} r + \frac{\partial}{\partial z}$$

Continuity:

$$\frac{\partial \rho}{\partial t} + \nabla \cdot (\rho \mathbf{v}) = 0 \tag{3.48}$$

Momentum (first order perturbation pressure):

$$\frac{\partial (\rho \mathbf{v})}{\partial t} + \nabla \cdot (\rho \mathbf{v}\mathbf{v}) = -\nabla p + \frac{1}{Re}\nabla \cdot \mathbf{T} + \frac{1}{Fr}\left(\frac{\rho^{\infty}}{\rho_{in}} - \rho\right) \tag{3.49}$$

where the viscosity term in the r-direction, assuming zero bulk viscosity is

$$\nabla \cdot \mathbf{T}\big|_r = \frac{\partial}{\partial r}\left[2\mu\frac{\partial v}{\partial r} - \frac{2}{3}\mu\nabla\cdot\mathbf{u}\right] + \frac{\partial}{\partial z}\mu\left[\frac{\partial v}{\partial z} + \frac{\partial u}{\partial r}\right] + 2\mu\frac{\partial v}{\partial r} - 2\mu\frac{v}{r^2} \tag{3.50}$$

and in the z-direction

$$\nabla \cdot \mathbf{T}\big|_z = \frac{\partial}{\partial z}\left[2\mu\frac{\partial u}{\partial z} - \frac{2}{3}\mu\nabla\cdot\mathbf{u}\right] + \frac{1}{r}\frac{\partial}{\partial z}\mu r\left[\frac{\partial v}{\partial z} + \frac{\partial u}{\partial r}\right] \tag{3.51}$$

Note that the hydrostatic pressure has been subtracted out in equation (3.49) to give a kinematic pressure.

Mixture Fraction:

$$\rho\frac{\partial Z}{\partial t} + \rho\mathbf{v}\cdot\nabla Z = \frac{1}{\mathrm{Re\,Sc}}\nabla\cdot(\rho D\nabla Z) \tag{3.52}$$

where,

$$Z = \frac{\lambda Y_F - Y_O + Y_O^\infty}{\lambda + Y_O^\infty}, \qquad 0 \le Z \le 1$$

Temperature:

$$T = T_O + \frac{Q/c_p}{1+\lambda}Y_p + (T_F - T_O)Z \tag{3.53}$$

Ideal gas for mixtures (thermodynamic pressure; zeroth order):

$$p = \rho RT \sum_{i=1}^{N} \frac{Y_i}{MW_i} \tag{3.54}$$

Mass fraction of fuel:

$$Y_F = \frac{Z - Z_{st}}{1 - Z_{st}}, \qquad Z_{st} \le Z \le 1, \quad Y_O = 0 \tag{3.55}$$

Mass fraction of oxygen:

$$Y_O = \frac{Z_{st} - Z}{Z_{st}} Y_O^{\infty}, \qquad 0 \le Z \le Z_{st}, \quad Y_F = 0 \tag{3.56}$$

Mass fraction of nitrogen:

$$Y_{N_2} = Y_{N_2}^{\infty}(1 - Z) \tag{3.57}$$

Mass fraction of products:

$$Y_P = 1 - (Y_F - Y_O - Y_{N_2}) \tag{3.58}$$

Mass fraction of individual species in products:

$$Y_j = Y_P \frac{(MW_j)(\nu_j)}{\sum_{i=1}^{M_P} (MW_i)(\nu_i)} \tag{3.59}$$

Chapter 4

Numerical Method

In this chapter, the numerical method used to solve the set of equations for a low speed, reacting flow as specified in Chapter 3 is described. The discrete formulation of the coupled set of partial differential equations is specified as well as the methodology for their solution.

4.1 Discrete Formulation

In this work the finite volume method is used to represent the discretized form of the conservation equations which are cast in axisymmetric coordinates (r,z). This method uses the integral form of the conservation equations and is applied to each control volume that subdivides the domain. Finite volume formulations guarantee local conservation for each control volume as well as global conservation for the entire domain.[19,43] The conservation equations can be written in the generalized form

$$\frac{\partial(\rho\phi)}{\partial t} + \nabla \cdot (\rho \mathbf{u}\phi) = \nabla \cdot (\tau \nabla \phi) + S_\phi \tag{4.1}$$

where ϕ can represent any dependent variable of the system, τ is a diffusion coefficient, and S_ϕ is a source term that includes any remaining significant terms. Equation (4.1) is integrated over a control volume and with respect to time over a time interval of Δt to result in

$$\int_{\Delta t}\int_{CV} \frac{\partial(\rho\phi)}{\partial t}\, dV dt + \int_{\Delta t}\int_{CV} \nabla \cdot (\rho \mathbf{u}\phi)\, dV dt = \int_{\Delta t}\int_{CV} \nabla \cdot (\tau \nabla \phi)\, dV dt + \int_{\Delta t}\int_{CV} S_\phi\, dV dt \tag{4.2}$$

By using Gauss' theorem the convective and diffusive integral terms in (4.2) can be rewritten as integrals over the entire bounding surface of the control volume.

$$\int_{\Delta t}\int_{CV}\frac{\partial(\rho\phi)}{\partial t}\,dV dt + \int_{\Delta t}\int_{A}\mathbf{n}\cdot(\rho\mathbf{u}\phi)\,dA dt = \int_{\Delta t}\int_{A}\mathbf{n}\cdot(\tau\nabla\phi)\,dA dt + \int_{\Delta t}\int_{CV}S_{\phi}\,dV dt \qquad (4.3)$$

where $\mathbf{n}$ is the unit vector normal to the bounding surface.

Equation (4.3) contains surface integrals that must be evaluated. In order to evaluate surface integrals exactly the integrand must be known everywhere on the volume surface. Since only the nodal value at the center of the control volume is available, an approximation must be introduced. This can be done by interpolating the value at the cell face from nodal values and then using the midpoint rule where the integral is the product of the integrand at the cell face center and the cell face area.

Other approximations such as the trapezoid rule in which corner values are averaged can be used as well as higher order approximations. Both the midpoint and trapezoid approximation are of second order. In this work a midpoint formulation is invoked for simplicity. Similarly, volume integrals must be approximated in equation (4.3). This is done by approximating the integral as the product of the nodal value at the volume center and the cell volume. Since all variables are known at nodal values no interpolation is necessary.

Cell face values are obtained by interpolation from nodal values in order to evaluate the convective fluxes. The simplest first order scheme is upwind interpolation[19] (UDS) in which face values are approximated as follows:

$$\phi_i = \begin{cases} \phi_I & \text{if } (\mathbf{v}\cdot\mathbf{n})_i > 0 \\ \phi_{I+1} & \text{if } (\mathbf{v}\cdot\mathbf{n})_i < 0 \end{cases} \tag{4.4}$$

where the index 'i' refers to face location and 'I' to nodal location as shown in figure 4.1, which illustrates a one-dimensional grid.

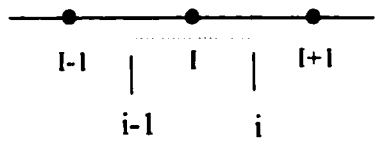

Figure 4.1: A control volume illustrating nodal and volume face indexing on a one-dimensional grid.

This scheme never produces numerical oscillations, thus it is very stable, but introduces large amounts of numerical diffusion thereby reducing the accuracy.

The simplest second order scheme is central differencing[19] (CDS) in which values are obtained by a linear interpolation between the two nearest nodes to a face.

$$\phi_i = \phi_{I+1}\alpha_i + \phi_I(1-\alpha_i), \quad \text{where} \quad \alpha_i = \frac{x_i - x_I}{x_{I+1} - x_I} \tag{4.5}$$

The leading truncation error term for CDS is proportional to the square of the grid spacing. Schemes of order higher than two are more accurate, but require a greater number of nodal values thereby increasing the computational effort. Boundary conditions also become more difficult to implement. Thus, due to its simplicity and to its sufficient level of accuracy, the central differencing scheme is utilized in this work. Gradients at cell faces using CDS are approximated with the second order representation

$$\left(\frac{\partial \phi}{\partial x}\right)_{face} = \frac{\phi_{I+1} - \phi_I}{x_{I+1} - x_I} \tag{4.6}$$

Approximation to the temporal integrals in (4.3) is done by an Adams-Bashforth scheme[19], which involves fitting a polynomial to the temporal derivatives at a number of points in time. This second order approximation is represented by

$$\phi\left(t^{n+1}\right) = \phi\left(t^{n}\right) + \frac{\Delta t}{2}\left\{3f\left[t^{n}, \phi\left(t^{n}\right)\right] - f\left[t^{n-1}, \phi\left(t^{n-1}\right)\right]\right\}, \quad \text{where } f = \frac{\partial \phi}{\partial t} \tag{4.7}$$

4.2 Solution Method of Discrete Equations

The approach to obtaining a numerical solution to the working equations is an explicit, projection based method developed by McMurtry et al.[29] To begin, it is assumed that all variables are known at time steps n and n-1. First, the mixture fraction equation (3.52) is integrated with respect to time using the Adams-Bashforth method to obtain Z^{n+1}. Then T^{n+1} and ρ^{n+1} are obtained by using equation (3.53) and the ideal gas equation (3.54) respectively. Next, the momentum equation is integrated with respect to time using the Adams-Bashforth method[19] resulting in

$$(\rho v)^{n+1} = (\rho v)^{n} - \Delta t \nabla \overline{p} + \Delta t\left(\frac{3}{2}\Pi^{n} - \frac{1}{2}\Pi^{n-1}\right) \tag{4.8}$$

where

$$\Pi = -\nabla \cdot (\rho \mathbf{v}\mathbf{v}) + \frac{1}{Re}\nabla \cdot \mathbf{T} + \frac{1}{Fr}\left(\frac{\rho^{\infty}}{\rho_{in}} - \rho\right)\mathbf{g}$$

$$\bar{p} = \frac{1}{\Delta t}\int_{t}^{t+\Delta t} p\, dt$$

Since $\bar{p}$ is needed for the time advancement of equation (4.8), a Poisson equation for $\bar{p}$ is formed by taking the divergence of equation (4.8) to obtain

$$\nabla^2 \bar{p} = -\frac{1}{\Delta t}\left[\nabla \cdot (\rho v)^{n+1} - \nabla \cdot (\rho v)^{n}\right] + \nabla \cdot \left(\frac{3}{2}\Pi^{n} - \frac{1}{2}\Pi^{n-1}\right) \tag{4.9}$$

The term $\nabla \cdot (\rho v)^{n+1}$ is evaluated by utilizing the continuity equation.

$$\nabla \cdot (\rho v)^{n+1} = -\left(\frac{\partial \rho}{\partial t}\right)^{n+1} \tag{4.10}$$

The term on the right hand side of equation (4.10) is approximated by

$$\frac{\partial \rho}{\partial t}^{n+1} = \frac{\rho^{n+1} - \rho^{n}}{\Delta t} \tag{4.11}$$

The strategy involves first computing convective and viscous terms that will be utilized in a Poisson equation for the average pressure $\bar{p}$. Once $\bar{p}$ is obtained velocity values at the n+1 time step can be obtained with the use of the momentum equation (4.8). The discretized Poisson equation forms a set of simultaneous equations that are solved using a conjugate gradient method.[19]

4.3 Grid

A staggered grid is used as shown in figure 4.2. Equation (4.3) is applied to each control volume that subdivides the domain. Scalar values are evaluated at locations shown by dots, and velocity values are evaluated at locations indicated by arrows. Each control volume has four plane faces and a central node P.

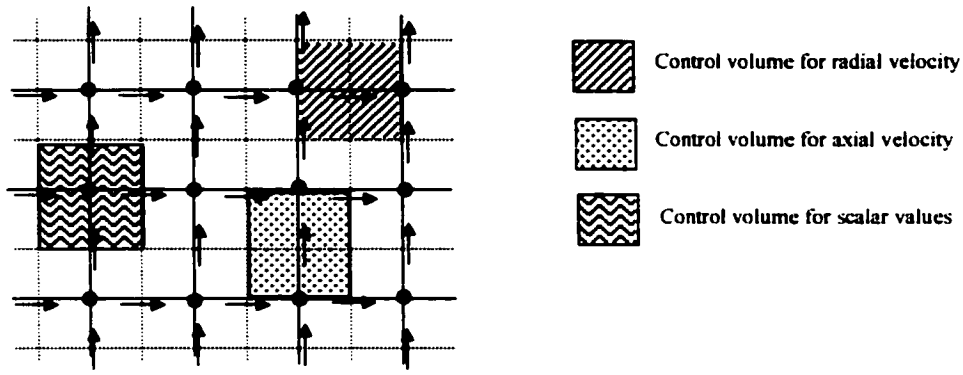

Figure 4.2: Control volume arrangement for a staggered grid

This grid structure is chosen so that no pressure nodes appear on the boundary, thus pressure boundary conditions are unnecessary. Only mass fluxes are needed at the boundary, which are prescribed and will be stated in the next section.

The grid is stretched in the radial and axial direction using the function

$$x = L\left[\frac{(\alpha+1)-\left\{(\alpha-1)\left[(\alpha+1)\,(\alpha-1)\right]^{(1-\bar{x})}\right\}}{\left[(\alpha+1)\,(\alpha-1)\right]^{(1-\bar{x})}}\right], \text{ where } 1<\alpha<\infty,\ 0\le x\le L \qquad (4.12)$$

$\bar{x}$ is generated from a uniform grid where $0\le\bar{x}\le 1$. The grid clusters near zero as $\alpha\to 1$. The grid is concentrated near the pool surface in the axial direction and near the axis of symmetry in the radial direction. The time step is limited by the minimum grid

spacing. Thus, the degree of clustering, indicated by α, was chosen by satisfying a unity Courant number where a fluid particle is not allows to travel more than one grid length in a time step. A unity Courant number requires $\Delta t < \Delta x_i/u_i$ or $\Delta x_i < u_i \Delta t$.

4.4 Boundary Conditions

The domain is axisymmetric in (r,z) coordinates, where u_z and u_r are the axial and radial velocities respectively. The interior nodes are indexed as i = 2,..,NZ-1 and j = 2,..,NR-1. Boundary nodes are located at i =1, NZ, and j =1, NR. Neumann boundary conditions are represented by $\phi|_{1,j} = \phi|_{2,j}$ and $\phi|_{i,1} = \phi|_{i,2}$, where the gradient of the variable is zero in the i^{th} and j^{th} direction respectively, and are of second order accuracy.

Inflow condition:

At the inflow all variables are specified, that is the velocity components, temperature, density, and mixture fraction are given set values. The values are prescribed as follows:

$$\left.\begin{aligned} u_z &= u_{in} \\ u_r &= 0 \\ Z &= 1.0 \\ \rho &= \rho_{in} \\ T &= T_{in} \end{aligned}\right\} \; 0 \le r \le \text{poolradius} \qquad (4.13)$$

For no co-flow:

$$\left.\begin{aligned} u_z &= u_{in} \\ u_r &= 0 \\ Z|_{1,j} &= Z|_{2,j} \\ \rho|_{1,j} &= \rho_{2,j} \\ T|_{1,j} &= T|_{2,j} \end{aligned}\right\} \text{pool radius} < r \leq \text{length of radial domain} \qquad (4.14)$$

Two of the simulations run in Chapter 5 for model validation were performed with co-flow in which an inner co-annular cylinder issues fuel, and an outer co-annular cylinder issues air. The boundary condition for co-flow is equation (4.14) for the inner cylinder issuing fuel, and for the outer cylinder issuing air it is the following:

$$\left.\begin{aligned} u_z &= u_{in\,air} \\ u_r &= 0 \\ Z &= 0 \\ \rho &= \rho_{in_{air}} \\ T &= T_{in_{air}} \end{aligned}\right\} \text{pool radius} < r \leq \text{radius of outer cylinder} \qquad (4.15)$$

Centerline condition:

The domain is axisymmetric, thus at the centerline the axial velocity gradient and scalar gradients in the radial direction are zero, and the radial velocity is zero, that is:

$$u_z|_{i,1} = u_z|_{i,2}$$
$$u_r|_{i,1} = 0$$
$$Z|_{i,1} = Z|_{i,2}$$
$$\rho|_{i,1} = \rho|_{i,2}$$
$$T|_{i,1} = T|_{i,2}$$

Air Entrainment Boundary:

Velocity values at the air entrainment boundary are unknown. Thus, the radial velocity component is determined by using the continuity equation. The axial velocity is computed by linear extrapolation. The pressure node at the scalar control volume nearest the boundary is set to zero. The boundary conditions are the following:

$$p|_{NR} = 0$$
$$u_r|_{i,NR} = \frac{1}{(\rho A)_{i,NR}}\left[(\rho A u_r)_{i,NR-1} + (\rho A u_z)_{i-1,NR-1} - (\rho A u_z)_{i,NR-1} - \left.\frac{\left(\rho^{n+1} - \rho^n\right)}{\Delta t}\right|_{i,NR}\right]$$
$$u_z|_{i,NR} = 2u_z|_{i,NR-1} - u_z|_{i,NR-2}$$
$$T_{i,NR} = T_{i,NR-1}$$
$$Z_{i,NR} = Z_{i,NR-1}$$
$$\rho_{i,NR} = \rho_{i,NR-1}$$

As previously mentioned, runs were performed for model validation in Chapter 5 with boundary conditions representing an outer cylindrical shield enclosing the fire. Those boundary conditions are as follows:

$u_r|_{i,NR} = 0$

$u_z|_{i,NR} = 0$

$T_{i,NR} = T_\infty$

$Z_{i,NR} = Z_{i,NR-1}$

$\rho_{i,NR} = \rho_\infty$

Outflow:

Two boundary conditions were tested for the outflow boundary. One was a convective condition for all variables prescribed at the inflow[19]:

$$\frac{\partial}{\partial t} + U\frac{\partial}{\partial z} = 0 \tag{4.16}$$

U is a constant velocity that is chosen so that the outflow mass flux is equal to the incoming mass flux. The second condition tested is a Neumann condition with the normal derivative of all variables set to zero:

$$\frac{\partial}{\partial z} = 0 \tag{4.17}$$

It was found that either condition is sufficient for this flow problem. Due to its simplicity, all quantities at the outflow boundary are prescribed with the Neumann boundary condition (4.17). The placement of the boundary was found to have the greatest effect on the flow field. It was found that the outflow boundary should be placed at least 20 diameters away. Thus, in these simulations the outflow boundary is placed far from the inflow (~30 – 50 diameters). Simulations of varying domain size were performed to ensure that boundary interference is minimized. Once the solution is invariant, the domain size is considered large enough.

The outflow boundary conditions are as follows:

$$u_z|_{NZ-1,j} = u_z|_{NZ-2,j}$$
$$u_r|_{NZ,j} = u_r|_{NZ-1,j}$$
$$Z|_{NZ,j} = Z|_{NZ-1,j}$$
$$\rho|_{NZ,j} = \rho|_{NZ-1,j}$$
$$T|_{NZ,j} = T|_{NZ-1,j}$$

4.5 Initial Conditions

Simulations are begun with the uniform values:

$$u_z|_{t=0} = 0$$
$$u_r|_{t=0} = 0$$
$$p|_{t=0} = 0$$
$$Z|_{t=0} = 0$$
$$\rho|_{t=0} = \rho_\infty$$
$$T|_{t=0} = T_\infty$$

Chapter 5

Model Validation

In this section, the combustion model is compared with the experimental results of other investigators. The first comparison is made with the work done by Santoro et al.[37] on a 1.11 cm ethane diffusion flame, the second with the experiments performed by Smooke et al.[41] on 1.11 cm methane diffusion flame, and lastly the experimental results by Schonbucher et al.[39] on a 4.6 cm diameter, n-hexane pool fire. Though a co-flow configuration is different from a pool fire or a pool-like gas fire, it can be utilized for model validation by invoking the appropriate boundary conditions as specified in Chapter 4. The following sections state the experimental configuration for the aforementioned research, the comparison between these experimental results and the results from using the combustion model used in this work, as well as a discussion on the experimental results. It should be noted that in Chapter 6 further model validation is provided by comparison with experiment on the relationship between the Strouhal and Froude number.

5.1 Ethane Diffusion Flame (1.11 cm)

Santoro et al.[37] performed experiments on a co-annular, ethane, laminar diffusion flame. The inner cylinder of 1.11 cm in diameter had fuel exiting with a velocity of .0398 m/s, and the outer 10.16 cm cylinder issued air at .089 m/s. Based on the inlet fuel velocity, inner cylinder diameter, and ambient viscosity of air the Froude and Reynolds number are 0.015 and 25, respectively. A cylindrical shield of 40.5 cm in height was used to prevent flame disturbances. Temperature, velocity, and soot measurements were taken to provide radial profiles of these quantities at several different axial locations. Figure 5.1 compares the calculated axial velocity profiles from this work with the

measured axial velocity profiles by Santoro et al. The radial and temperature profiles have not been presented due to reasons stated in the discussion section of this chapter.

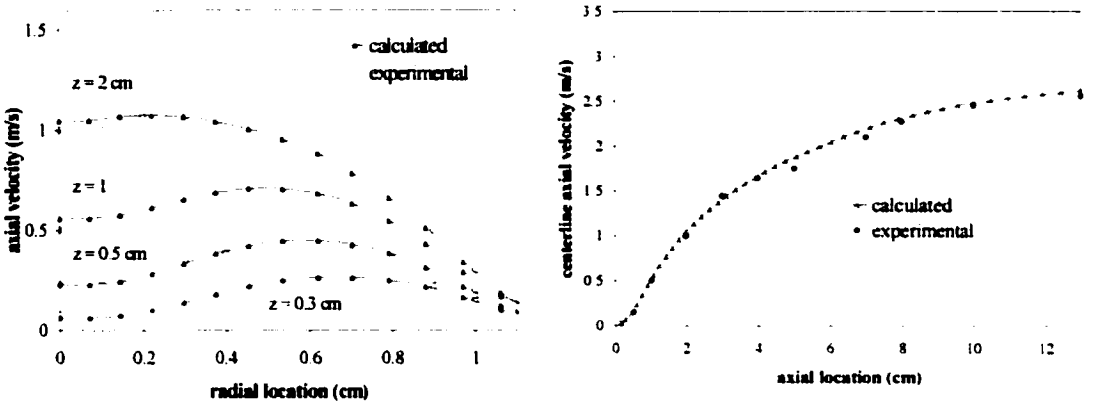

(a) (b)

Figure 5.1: (a) Axial velocity at various elevations, (b) centerline axial velocity (ref. 37)

5.2 Methane Diffusion Flame (1.11 cm)

Smooke et al.[41] took temperature, species, and soot measurements of a co-annular, methane diffusion flame. The inner cylinder of 1.11 cm in diameter had fuel exiting with a velocity of .0552 m/s, and the outer 9.53 cm cylinder issued air at .1254 m/s. Based on the inlet fuel velocity, inner cylinder diameter, and ambient viscosity of air the Froude and Reynolds number are 0.028 and 34, respectively. The outer cylinder extended beyond the inner cylinder to provide a barrier against disturbances. Figure 5.2 compares the calculated temperature values from this work with the measured temperature values by Smooke et al. at various elevations.

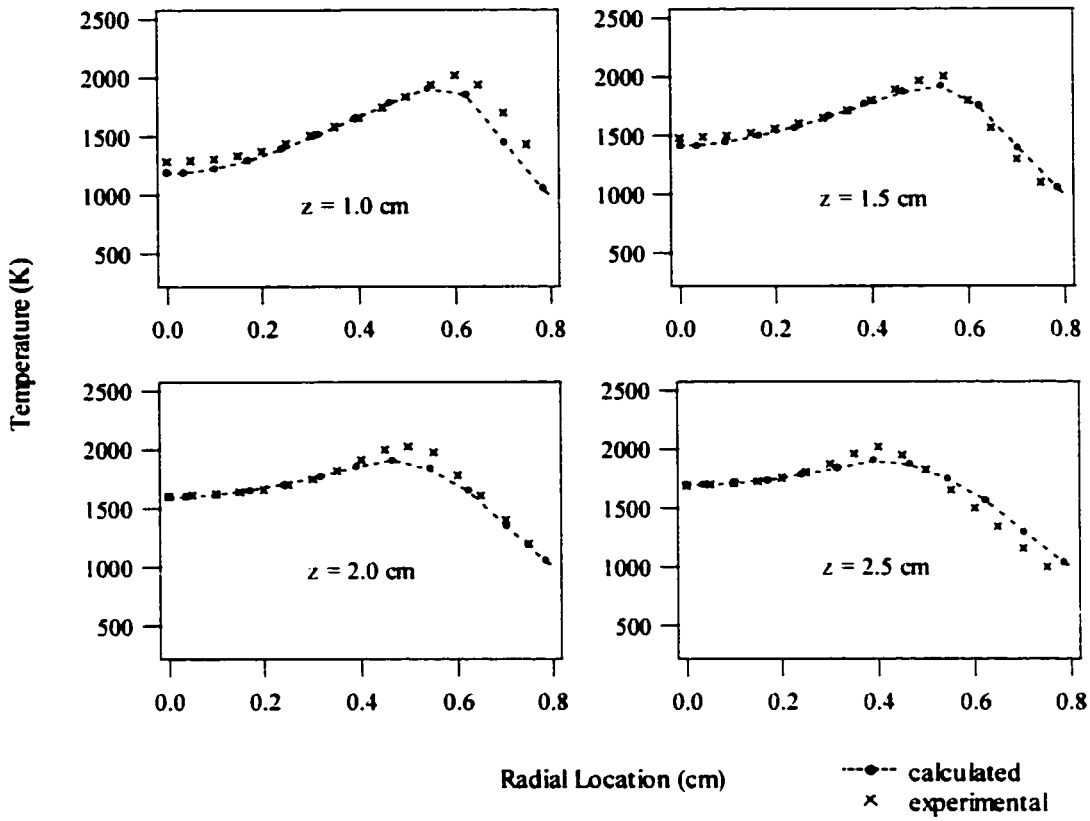

Figure 5.2: Comparison between calculated and measured temperature values at various elevations (ref. 41).

5.3 N-Hexane Pool Fire (4.6 cm)

Schonbucher et al.[39] performed experiments on several different fuels for diameters between $1 \leq d \leq 10$ cm, and used real-time, holographic interferometry to determine the density field, which revealed organized structures they termed 'density parcels'. The geometric configuration is one in which fuel exits from a circular burner into ambient still air.

They provide frequency data at various elevations for a 4.6 cm, n-hexane pool fire with a fuel exit velocity of .011 m/s (Fr = .00027, Re = 29). The mean frequency data for up to 8 cm (1.74 dia.) indicate that there is one independent frequency of 3 Hz and two harmonics of 9 and 12 Hz as shown in Figure 5.3. The frequency of 3 Hz is associated with the formation of the density parcel configuration, and that of 9 Hz with vertical oscillations of the fuel boundary layer. The frequency of 12 Hz is associated with the following processes: wave motion of the visible fire shape, oscillations of density parcels at the fire rim, helical wave motion of the thermal boundary layer, and the rise of density parcels.

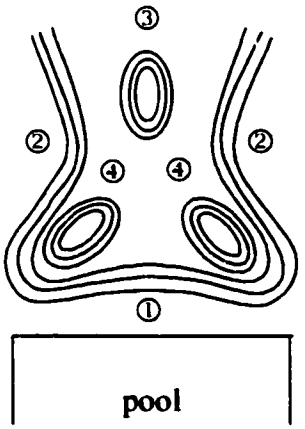

① - Vertical oscillation of the fuel boundary layer (9 Hz)

② - Helical wave motion of the thermal boundary layer (12 Hz)

③ - Rise of density parcels (12 Hz)

④ - Oscillations of density parcels at the pool rim (12Hz)

Figure 5.3: Mean frequency profile of 4.6 cm n-hexane pool fire for height region $0 \leq z \leq 8$ cm (ref. 39).

From this work, the results for temperature and temperature frequency response values are shown in Figures 5.4 - 5.7. The averaged frequency was determined by using an amplitude-weighted average. At a location that corresponds to the fuel boundary layer in Figure 5.3, the average frequency is 9.33 Hz (Fig. 5.4), as compared to the experimental value of 9 Hz.

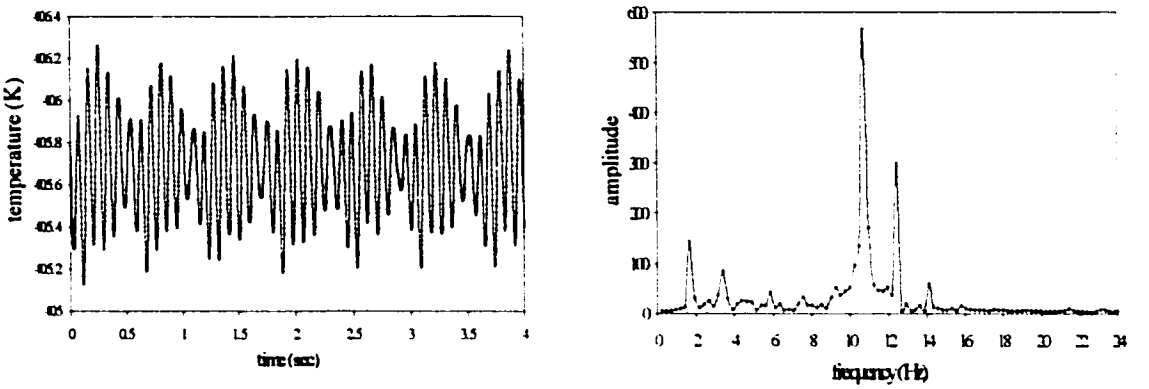

Figure 5.4: Centerline temperature (a) and temperature frequency response (b) at elevation z = .026 cm.

At a location that corresponds to the rise of density parcels in Figure 5.3, the average frequency is 11.55 Hz (Fig. 5.5), as compared to the experimental value of 12 Hz.

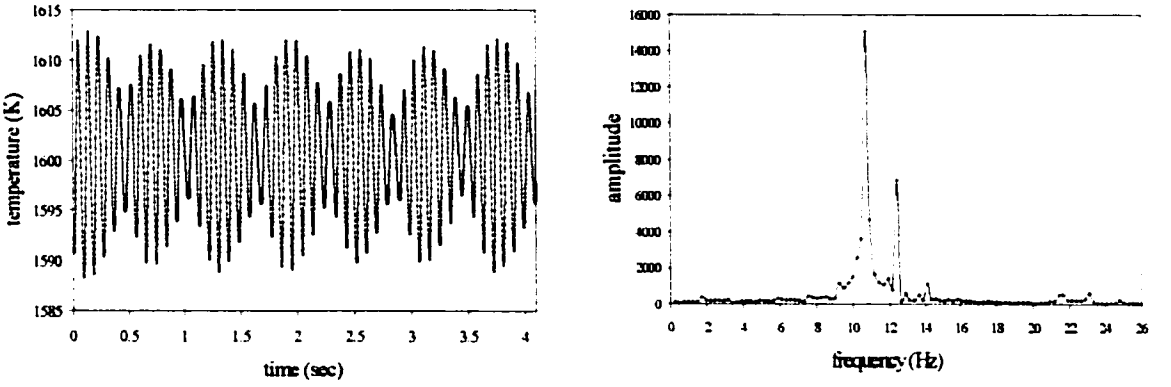

Figure 5.5: Centerline temperature (a) and temperature frequency response (b) at elevation z = 5.61 cm.

At a location that corresponds to the thermal boundary layer in Figure 5.3, the average frequency is 12.1 Hz (Fig. 5.6), as compared to the experimental value of 12 Hz.

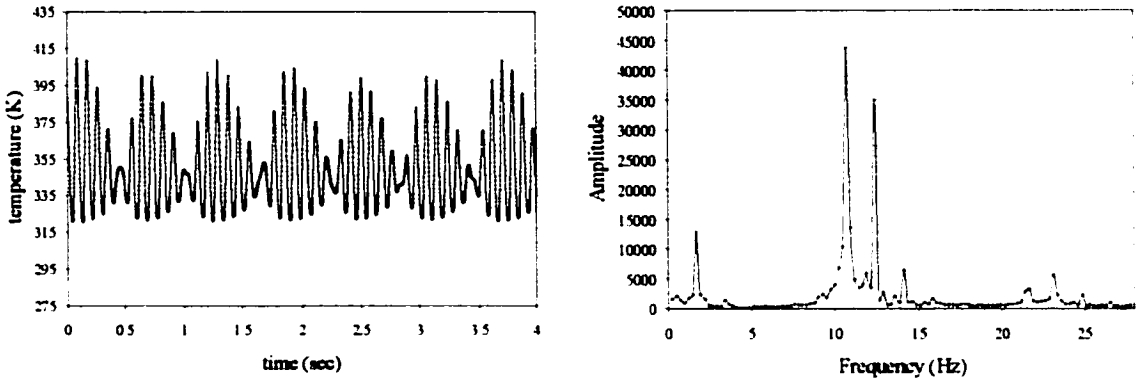

(a) (b)

Figure 5.6: Temperature (a) and temperature frequency response (b) at elevation z = 5.61 cm and radial location r = 1.98 cm.

At a location that corresponds to the oscillation of density parcels at the pool rim in Figure 5.3, the average frequency is 10.55 Hz (Fig. 5.7), as compared to the experimental value of 12 Hz.

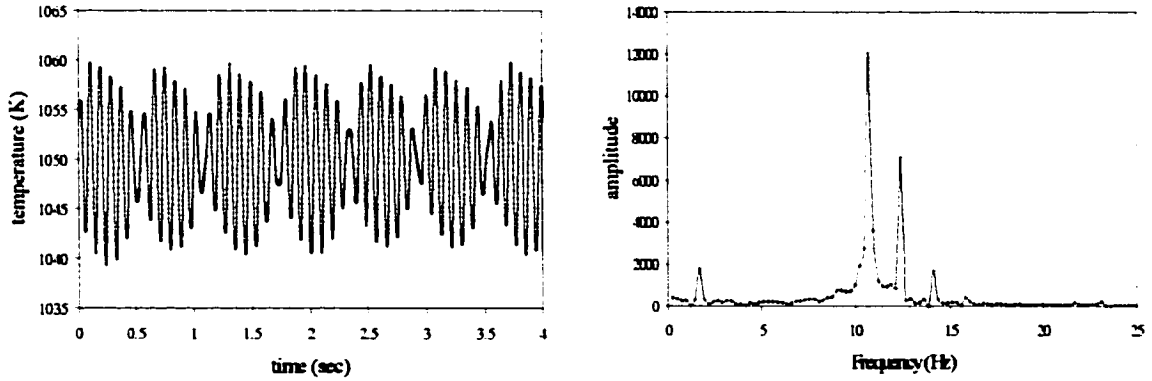

(a) (b)

Figure 5.7: Temperature (a) and temperature frequency response (b) at elevation z = .094 cm and radial location r = 1.98 cm.

5.4 Discussion

The numerical results from this work indicate good agreement with the experimental results as shown in Figures 5.1-5.7. A few remarks should be made concerning the experimental results. The centerline axial velocity measurements by Santoro et al. (Fig. 5.1b) show a deviation from the experimental trend line around 6 cm. Similarly, the radial velocity measurements shown in the work by Santoro et al. are highly asymmetric for heights greater than 4 cm. They state that this is probably due to room disturbances made allowable by large slot openings used in the chimney. They also state that the temperature profiles are of a qualitative nature due to multiple sources of error. Thus, radial velocity and temperature profile comparisons have not been presented in this work.

For temperature measurements Smooke et al. state that using a 75-μm thermocouple wire gives less error than a 125-μm wire, which can have conduction errors up to 100 K. They estimate that the absolute error in the gas temperatures is less than 50 K in soot-free flame regions. No estimate is given for soot flame regions. They also performed a numerical simulation of the methane diffusion flame and found disagreement with experimental temperature measurements. Their numerical model includes finite rate chemistry with a detailed soot growth formulation. Figure 5.8 shows a comparison between their numerical results and experimental values. Their numerical results are too low up to the flame edge by about 100 to 150 K, and too high past the flame edge by 200 to 500 K. The flame edge is also over predicted with a radial difference of .05 to .1 cm. They attribute the disagreement to the uncertainty of the inlet boundary conditions as well as the lack of including in their model the absorption by methane of energy radiated from the flame front. They state that conduction and radiation from the base of the flame to the burner exit tube caused significant preheating of both inlet fuel and air streams.

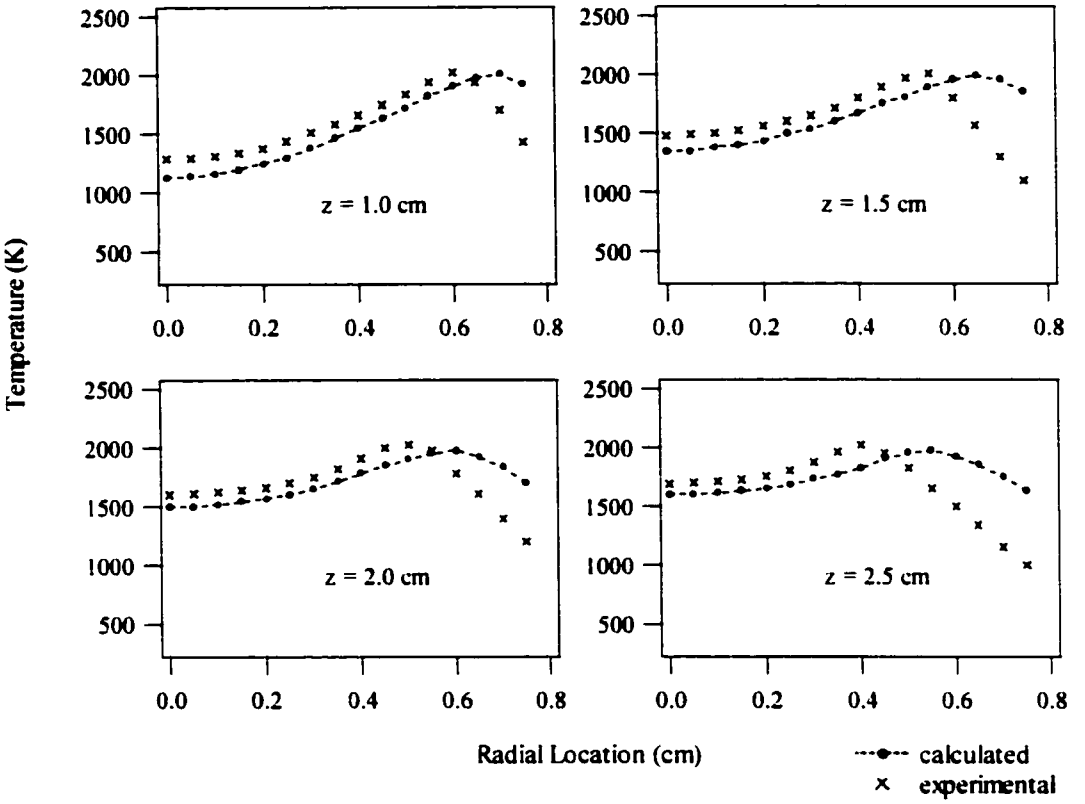

Figure 5.8: Comparison between calculated and measured temperature values at various elevations from numerical and experimental work by Smooke et. al. (ref. 41).

It is also of interest to note a comparison between the work done by Smooke et al. and work done by Mitchell et al.[32,33] Mitchell et al. provided experimental and numerical results for a co-annular, methane diffusion flame of 1.27 cm diameter with a fuel exit velocity of .045 m/s, and air co-flow of .0988 m/s. The Froude and Reynolds number are .016 and 32 respectively, which is similar to the system investigated by Smooke et al. with a Froude and Reynolds number of .028 and 34 respectively. When the results of these two bodies of work are compared there is a discrepancy in centerline temperatures at similar heights of 400 to 500 K. The difference in the Froude number is not great

enough to explain such a large discrepancy. Mitchell et al. state that errors from incorrect emissivity values for thermocouple measurements can cause significant temperature errors. Temperature measurements can have sources of error from radiation effects, conduction along thermocouple wire, catalytic effects due to the presence of bare thermocouple wire, and soot coating of thermocouples that change emissivity values. The point to be made about these two experimental studies is the difficulty in obtaining agreement. Experimental results can differ from multiple sources of error. Experimental boundary conditions can also be difficult to control as was pointed out in the work done by Santoro et al.

The numerical results show good agreement with three different variables, namely, velocity, temperature, and frequency for independent experimental investigations. As stated previously, further model validation is provided in Chapter 6 wherein agreement with experiment is found for the relationship between the Strouhal and Froude number. The model is also tested for a non-uniform inlet velocity profile in order to ascertain the effect on the dynamics investigated. The results shown in Chapter 6 indicate that an exponential inlet velocity profile does not effect the dynamics of interest. This further supports the validity of the model by indicating that the gaseous region of pool-like gas fires are similar to pool fires. This will be further discussed in Chapter 6. Given the good agreement with the experimental studies provided, it can be concluded that the model is capable of capturing the pertinent characteristics of pool-like gas fires, and thus ultimately the gas-phase of small pool fires.

Chapter 6

Results and Discussion

In this chapter numerical results are presented for the following parametric cases: (Fr =.01, Re = 40), (Fr = .001, Re = 40), (Fr = .0001, Re = 40), (Fr = .001, Re = 10), and (Fr = .001, Re = 100). The Froude number is defined as $Fr = v_{in}^2/Dg$, where v_{in} is the fuel velocity at the pool surface, D the pool diameter, and g the gravitational constant. The Reynolds number is defined as $Re = v_{in}D/\upsilon_{in}$, where υ_{in}, is the fuel inlet kinematic viscosity. For each case, results comparing the magnitude of baroclinic torque and density gradient/gravity interaction are presented, as well as the shear and buoyancy production terms in the equation for the kinetic energy of fluctuating motion. The results showing the effect of heat release rate, fuel molecular weight, air-fuel ratio, and inlet velocity profile on the energetics, vorticity generation, and frequency response are provided for the case Fr = .01, Re = 40. For all cases, a local Reynolds and Froude number is identified as a function of axial location. Contour and velocity vector plots showing instantaneous values for the case, Fr = .001, Re = 40 are presented. Temperature frequency response is computed and compared for all cases at various locations. A discussion of the results is also provided in this chapter.

The simulations were performed on a computational domain of 30 diameters in the axial direction and 6 diameters in the radial direction. For all cases, the time step was chosen so that a fluid particle does not travel more than one grid length in a single time step. Thus, the time step satisfies a Courant number, c, of less than 1.0, where $c = u_i \Delta t/\Delta x_i$.[19] Thus, $\Delta t < \Delta z/u$ and $\Delta t < \Delta r/v$. For cases (Fr = .01, Re = 40) and (Fr = .001, Re = 10) the grid was stretched in the axial direction with minimum grid spacing of .103 diameters and 100 nodes, and in the radial direction with minimum grid spacing of .0278 diameters and 75 nodes. Thus, 24 axial nodes are concentrated under 5 axial diameters, and 18 radial nodes are concentrated under 1 radial diameter. The time step used is 10^{-3} in

dimensionless time. This corresponds to 4.25 x 10^{-4} and 1.25 x 10^{-3} seconds in real time for cases (Fr = .01, Re = 40) and (Fr = .001, Re = 10), respectively. For cases (Fr = .001, Re = 40), (Fr = .0001, Re = 40), and (Fr = .001, Re = 100) the grid was stretched in the axial direction with minimum grid spacing of .0451diameters and 100 nodes, and in the radial direction with minimum grid spacing of .0133 diameters and 75 nodes. Thus, 36 axial nodes are concentrated under 5 axial diameters, and 27 radial nodes are concentrated under 1 radial diameter. The time steps used is 10^{-4} in dimensionless time. This corresponds to 3.8 x 10^{-4}, 2.65 x 10^{-4}, and 9 x 10^{-4} seconds in real time for cases (Fr = .001, Re = 40), (Fr = .001, Re = 100), and (Fr = .0001, Re = 40), respectively. The runs were performed on a 1GHz single processor PC operating on Microsoft Windows. The code was programmed in Fortran 90 using Compaq Visual Fortran as the compiler. The computational time to reach a converged state was approximately 1 hour for cases (Fr=.01, Re =40) and (Fr = .001, Re =10), and 10 hours for cases (Fr = .001, Re = 40), (Fr = .0001, Re = 40), and (Fr = .001, Re = 100). To obtain time averages the computational time was approximately 15 minutes for cases (Fr=.01, Re =40) and (Fr = .001, Re =10), and 2.5 hours for cases (Fr = .001, Re = 40), (Fr = .0001, Re = 40), and (Fr = .001, Re = 100). Inlet fuel temperature and density values are 295 K and .66 kg/m^3, respectively. Corresponding values of fuel inlet velocity and diameter for the various parametric cases is shown in Table 6.1.

Table 6.1: Corresponding fuel inlet velocities and diameters for parametric cases

Parametric Values	Fuel inlet velocity (m/s)	Diameter (m)
Fr = .001, Re = 10	.012	.015
Fr = .01, Re = 40	.040	.017
Fr = .001, Re = 40	.019	.038
Fr = .001, Re = 100	.026	.069
Fr = .0001, Re = 40	.009	.080

It was found that the flow was able to develop oscillations without the deliberate introduction of a perturbation. Thus, numerical perturbations were sufficient to excite the flow. In order to perturb the flow with a wide range of unbiased frequencies the following perturbation was introduced into the axial velocity at three grid points just above the inflow boundary:

u=u(1+.01*sin(random number*t)), where 0<random number<1000.

Thus, a perturbation with a maximum of 1% variation from the axial velocity value at those three locations is provided.

For the results that follow it should be noted that though calculations were done for a 30 diameters axial extent the validity of the solution pertains only to much lower elevations depending on the parametric values. This is due to the breakdown of the axisymmetric assumption. The elevation of solution validity decreases as the Froude number decreases and as the Reynolds number increases. Thus, for the cases of (Fr=.0001, Re=40) and (Fr=.001, Re=100) elevations up to 1 to 2 diameters should be considered to be valid. Determining the elevation at which an axisymmetric solution is valid will be addressed in a later section of this chapter.

6.1 Vorticity Generation Terms

To facilitate understanding of the results and discussion to follow, the vorticity transport equation in terms of dimensionless variables is explained:

$$\frac{D\omega_\theta}{Dt} = \omega_\theta \frac{v}{r} - \omega_\theta\left(\frac{\partial u}{\partial z} + \frac{1}{r}\frac{\partial(rv)}{\partial r}\right) + \frac{1}{\rho^2}\left(\frac{\partial \rho}{\partial z}\frac{\partial p}{\partial r} - \frac{\partial \rho}{\partial r}\frac{\partial p}{\partial z}\right) - \frac{1}{\rho^2}\frac{\rho_\infty}{\rho_{in}}\frac{1}{Fr}\frac{\partial \rho}{\partial r} + \frac{\mu}{Re}\left(\frac{\partial^2 \omega_\theta}{\partial z^2} + \frac{\partial^2 \omega_\theta}{\partial r^2} + \frac{1}{r}\frac{\partial \omega_\theta}{\partial r} - \frac{\omega_\theta}{r^2}\right) \tag{6.1}$$

where,

$$\omega_\theta = \frac{\partial v}{\partial z} - \frac{\partial u}{\partial r}.$$

Note that the dynamic viscosity is temperature dependent and dimensionless. On the right-hand side, the first and second term represents vortex stretching and expansion, which can either increase or decrease vorticity. The third term is baroclinic torque, which generates vorticity by the misalignment of density and pressure gradients. In baroclinic flow, a volume element will have net pressure forces acting through its center, but not through its center of mass. The center of volume and the center of mass do not coincide for baroclinic flow. Thus, the net pressure force acting on a volume element creates a torque about the center of mass, which is perpendicular to both the pressure and density gradients. To aid understanding, consider a block comprised of two different materials, where $\rho_1 > \rho_2$ as shown in Figure 6.1.

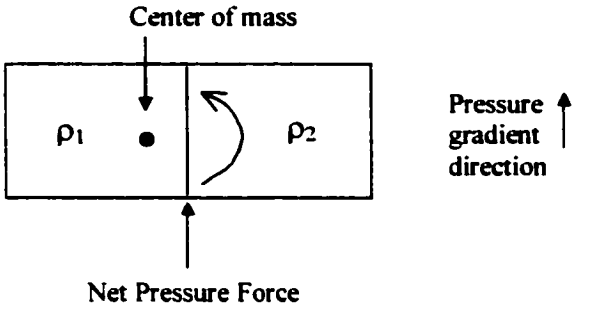

Figure 6.1: Block made of two different materials illustrating baroclinic torque.

If a surface comprising both materials is oriented perpendicular to the direction of the pressure gradients then a torque will be generated. The denser material will be rotated below the lighter material.

The fourth term is the gravitational term, which can generate vorticity due to the interaction between the radial density gradients and gravity. This term generates vorticity by the action of gravity, which forces the heavier or denser part of a volume element below the lighter part thereby creating rotation. The last term is the diffusion of vorticity and its effect is to redistribute vorticity, not generate it. Baroclinic torque and the gravitational term are responsible for the initiation of vorticity. They are evaluated for each parametric case and presented in this section.

Figure 6.2 shows the spatially integrated, absolute values of the vorticity production terms time-averaged over a cycle for varying Froude and Reynolds number. Total values are plotted against axial distance in diameters. The parametric cases shown are for methane pool-like gas fires. The results indicate that the gravitational production term has a greater influence on vorticity generation than baroclinic torque. Decreasing the Froude number results in both production terms increasing, while increasing the Reynolds number results in a slight decrease in the gravitational term. The baroclinic torque term decreases once the Reynolds number is at a large enough value. The greatest effect of baroclinic torque occurs at lower elevation as can be seen by the higher gradients in the first few diameters. The effect of the gravitational term has a more constant gradient that continues up through higher elevations, though its highest gradients occur at lower elevations as well.

The increase in the gravitational term for decreasing Froude number is indicative of the greater buoyancy forces for lower Froude numbers. The gravitational term has a factor of the inverse Froude number. Thus, for a decrease of a factor of 10 in Froude number, this term should increase by a factor of 10. Instead, the results show this term increasing by a factor of approximately 5 for every order of magnitude decrease in Froude number. This difference can be attributed to the radial density gradients decreasing for decreasing Froude number. As the Froude number decreases there is greater entrainment resulting in greater mixing, thereby decreasing the radial density

gradients. This effect can be seen from time-averaged temperature contours in Figure 6.51. It can also be seen that as the Froude number is decreased, axial density gradients increase near the pool surface. This can be attributed to the action of the stronger vortices pushing the flame inward as shown in Figure 6.51. It would then be expected that the axial density gradients increase as well as the radial pressure gradients, while the radial density gradients decrease. Thus, by examining the terms that comprise baroclinic torque in equation (6.1), it would be expected that baroclinic torque would increase for decreasing Froude number.

The decrease in the gravitational term for an increase in Reynolds number can be explained by looking at the time-averaged temperature contours shown in Figure 6.51. For a change in Reynolds number from 10 to 40, the flame sheet becomes less defined. For Re = 10, viscous forces are higher and tend to stabilize the flow, and thus the time-averaged temperature contours show the flame sheet up to 2 diameters above the pool surface. For Re = 40, greater entrainment occurs which brings in air at a lower temperature resulting in the time-averaged temperature gradients decreasing. Thus, the radial density gradients decrease. Since the Froude number is kept constant and radial density gradients are decreasing, the gravitational term decreases. The axial density gradients also increase at lower elevation, thereby causing an increase in the baroclinic torque at lower elevations.

The decrease of the gravitational term for an increase of Reynolds number from 40 to 100 can be attributed to the narrowing of the flame, rather than greater entrainment. For an increase in Reynolds number from 40 to 100, the flame height increases and narrows as can be seen from Figure 6.51. Thus, the spatially integrated values of radial density gradients would then decrease due to the narrowing of the flame. The axial density gradients decrease as well, thereby causing the baroclinic torque term to decrease.

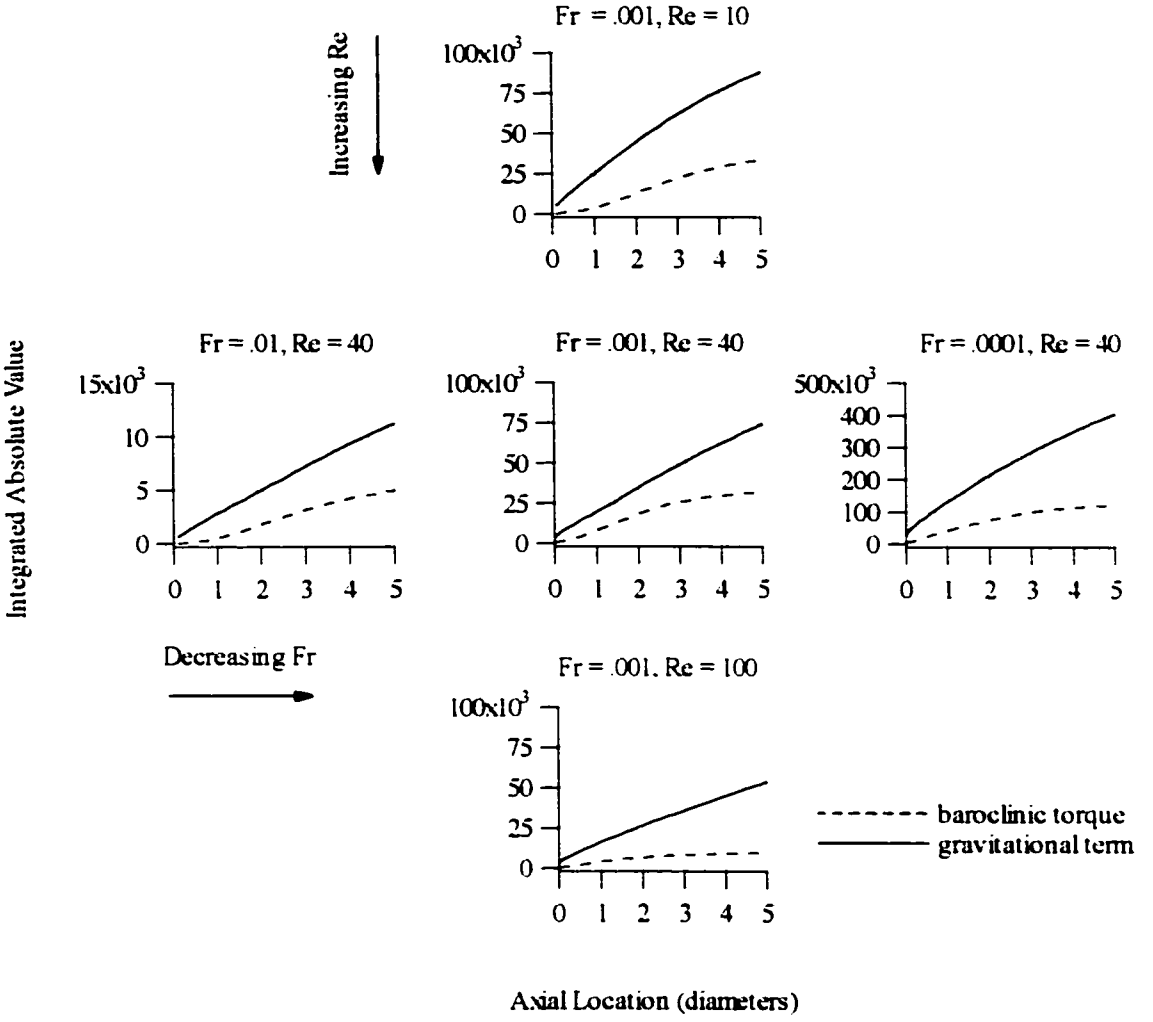

Figure 6.2: Time averaged, spatially integrated, absolute values of vorticity production terms.

Figure 6.3 shows the spatially integrated, absolute value of vorticity over one cycle for all cases. The vorticity increases with decreasing Froude number, and decreases with increasing Reynolds number. These values of vorticity reflect the same pattern as that found for the vorticity production terms in Figure 6.2.

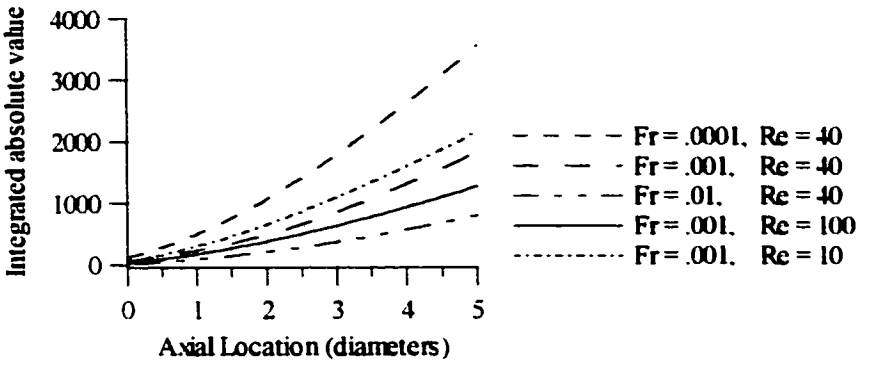

Figure 6.3: Time averaged, spatially integrated, absolute value of vorticity.

6.2 Shear and Buoyancy Production

In order to access the relative contributions of shear and buoyancy instabilities, the energetics of the flow was examined by considering the kinetic energy of fluctuations from a mean flow. A kinetic energy equation for these fluctuations was formed and the shear and buoyancy production terms evaluated. This equation is similar to that of the turbulent kinetic energy equation, though in this work the flows are not turbulent; the fluctuations are ordered rather than random. The mean is considered to be Favre-averaged quantities for velocity, and time averaged quantities for all other variables over one cycle. Since quantities are not exactly uniform from one cycle to the next, averages are obtained over many cycles. For all runs, it was found that five cycles are sufficient for averages to become invariant. Once averages are obtained, a second run is performed to obtain the fluctuating quantities by subtracting the average values from the total values. The kinetic energy equation for fluctuations is derived by subtracting the momentum equation of the Favre-averaged mean flow from the total flow. Total values are decomposed into mean and fluctuating quantities as: $u_i = \tilde{u}_i + u_i''$, $\rho = \bar{\rho} + \rho'$, $p = \bar{p} + p'$. Favre-averaging results in $\overline{\rho u''} = 0$, $\overline{\rho'} = 0$, $\overline{p'} = 0$. The momentum equation for

fluctuations is then multiplied by u_i'' and Favre-averaged to arrive at an equation for the kinetic energy of fluctuations. The equation is as follows:

$$\frac{\bar{\rho}}{2}\frac{\partial \widetilde{u_i''^2}}{\partial t} + \frac{\bar{\rho}}{2}\tilde{u}_k \frac{\partial \widetilde{u_i''^2}}{\partial x_k} = -\frac{\partial\left(\overline{u_i''p''}\right)}{\partial x_j} - \bar{\rho}\widetilde{u_k''u_i''}\frac{\partial \tilde{u}_i}{\partial x_k} + \tilde{u}_i \nabla\cdot\bar{\tau}'' + \overline{u_i''(\rho_\infty - \rho')g} \qquad (6.2)$$

where,

$$\tilde{u}_i = \lim_{T\to\infty}\frac{1}{\bar{\rho}}\frac{1}{2T}\int_{-T}^{T}\rho u_i dt = \frac{\overline{\rho u_i}}{\bar{\rho}}$$

$$\bar{\rho} = \lim_{T\to\infty}\frac{1}{2T}\int_{-T}^{T}\rho dt$$

$$\bar{p} = \lim_{T\to\infty}\frac{1}{2T}\int_{-T}^{T}p dt$$

The second and fourth terms on the right-hand side are kinetic energy production of fluctuations due to shear and to buoyancy, respectively. If the shear production term with its sign included is positive, it represents a gain in the kinetic energy of the fluctuations and a loss to the mean flow. Thus, in this case, shear production would be providing instability to the flow by generating energy for fluctuations. Conversely, a negative value would indicate a loss to the kinetic energy of the fluctuations and a gain to the mean flow, and thus providing stability to the flow. A positive value for the buoyancy production term reflects positive density gradients. A positive density gradient implies that a rising fluid elements will more likely have a positive velocity fluctuation, as well as a negative density fluctuation, thereby giving a positive value for this term. Positive buoyancy production is hence reflective of areas where heaver fluid lies on top of lighter fluid as in a Rayleigh-Taylor instability.

Figure 6.4 shows the spatially integrated values for shear production and buoyancy production. The results indicate that buoyancy production provides a much greater contribution to the kinetic energy of fluctuations than shear production for all cases.

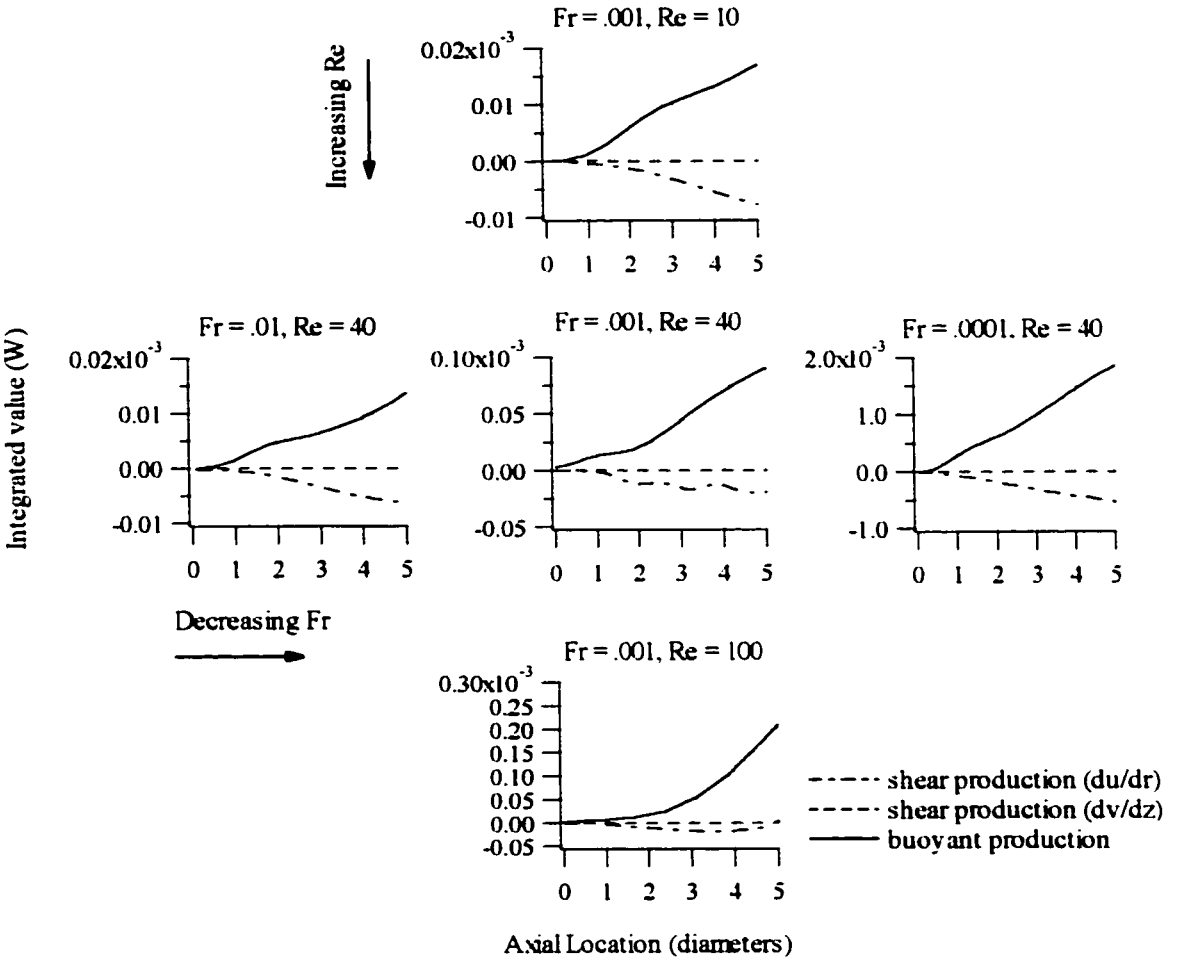

Figure 6.4: Favre-averaged, spatially integrated values of production terms for the kinetic energy of fluctuations.

Buoyancy production increases with decreasing Froude number, and increases with increasing Reynolds number. Thus, a lower Froude number results in more areas where axial density gradients result in buoyant motion. The shear production from averaged radial velocity gradients in the axial direction is negligible in all cases. For all cases, the shear production from averaged axial velocity gradients in the radial direction is negative. This indicates that shear has an overall stabilizing influence, though it should be noted that areas of positive shear production occur, but when spatially integrated the net effect is negative. For the case of (Fr=.001, Re=100) shear production has negative values below 5 axial diameters, and positive values above 5 axial diameters. This would indicate that once a sufficiently high Reynolds number is reached, shear production becomes destabilizing due to the higher momentum forces. Negative shear production increases as the Froude number is decreased, and decreases as the Reynolds number is increased. To illustrate how a negative value for shear production can occur consider a mean velocity profile as shown with velocity vectors in Figure 6.5. If a fluid particle at point A has a disturbance causing the particle to travel to a region to the left such as point B, then this

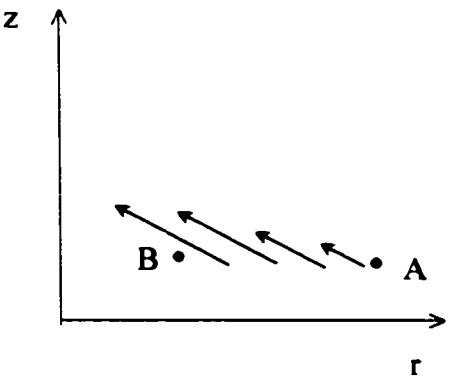

Figure 6.5: Velocity vectors of a mean flow

particle would tend to decrease the magnitude or slow down the fluid at point B since it has come from a region of slower moving fluid. This would result in a negative value for u′ and a positive value for v′. The sign of the mean axial velocity gradient in the radial direction is negative. Thus, the total sign of the shear production term would be negative as can be seen from equation 6.2. The shear production term would then have a stabilizing influence. This same flow pattern can be seen in Figure 6.52 shown at the end of this chapter. If the velocity vectors in Figure 6.5 were oriented parallel to the z-axis where the v-component is zero, then u′ would be negative and v′ would be negative since the mean value for v is zero. The shear production term would then have a positive sign. Thus, the shear production term would have a destabilizing influence. This can explain the trend seen as the Froude number is decreased, as well as when the Reynolds number is increased. As the Froude number decreases the radial velocity component becomes greater in magnitude in the negative radial direction, thus, the orientation of the mean velocity vectors become increasingly similar to those shown in Figure 6.5. Whereas, for the case with Re = 100, the mean velocity vectors have a lower v-component and thus are closer to an orientation where the vectors are parallel to the z-axis.

The spatially, integrated values of kinetic energy per unit mass of fluctuations is shown in Figure 6.6. The kinetic energy increases with decreasing Froude number, and increases with increasing Reynolds number.

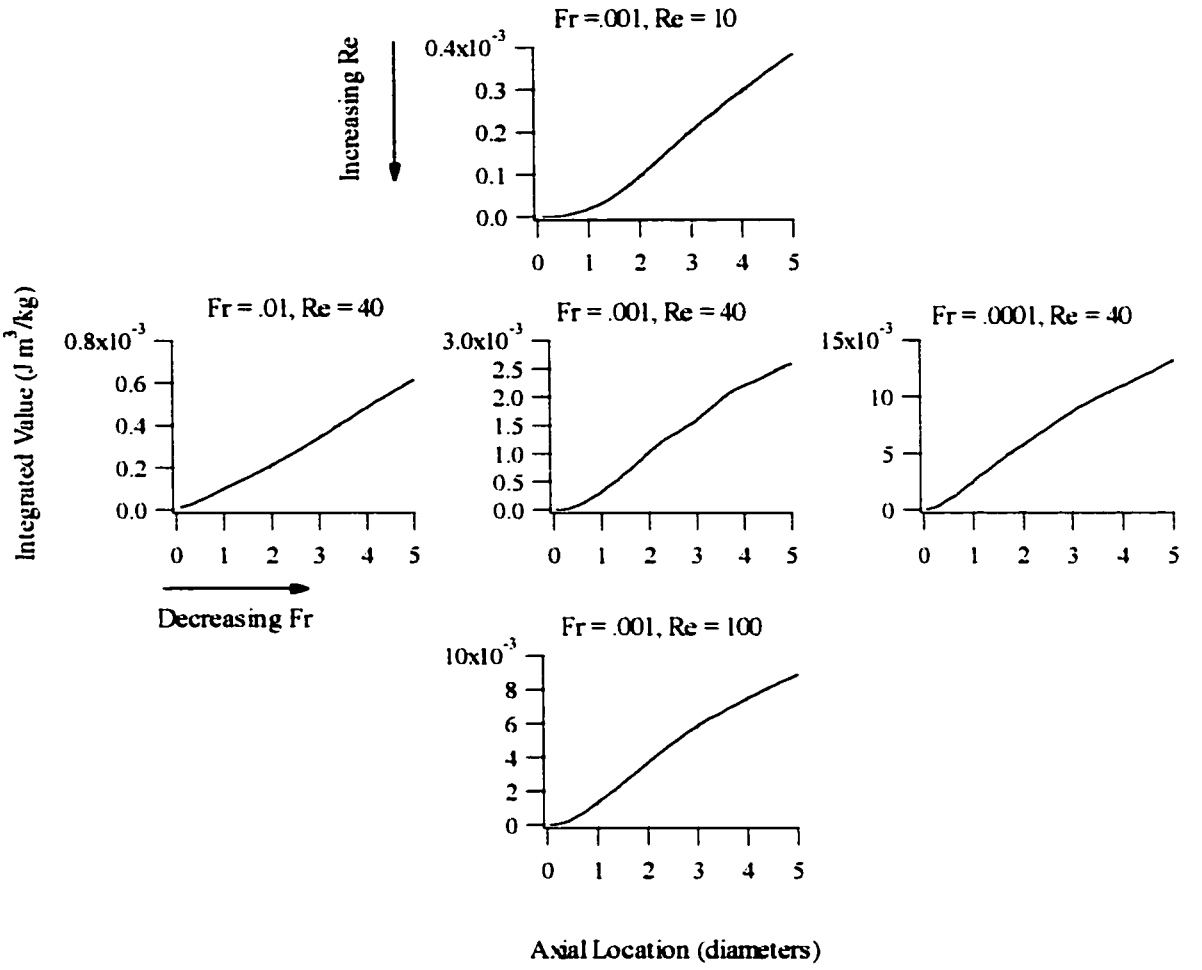

Figure 6.6: Favre-averaged, spatially integrated values for kinetic energy of fluctuations.

6.3 Frequency Spectrum

The temperature frequency spectrum as a function of varying Froude number and Reynolds number is show in Figures 6.7-6.10 at four different locations. At all locations, the results indicate that the dominant frequency decreases with decreasing Froude number, and decreases with increasing Reynolds number. The dominant frequency remains the same at all locations for these cases, but the amplitudes and number of harmonics differ.

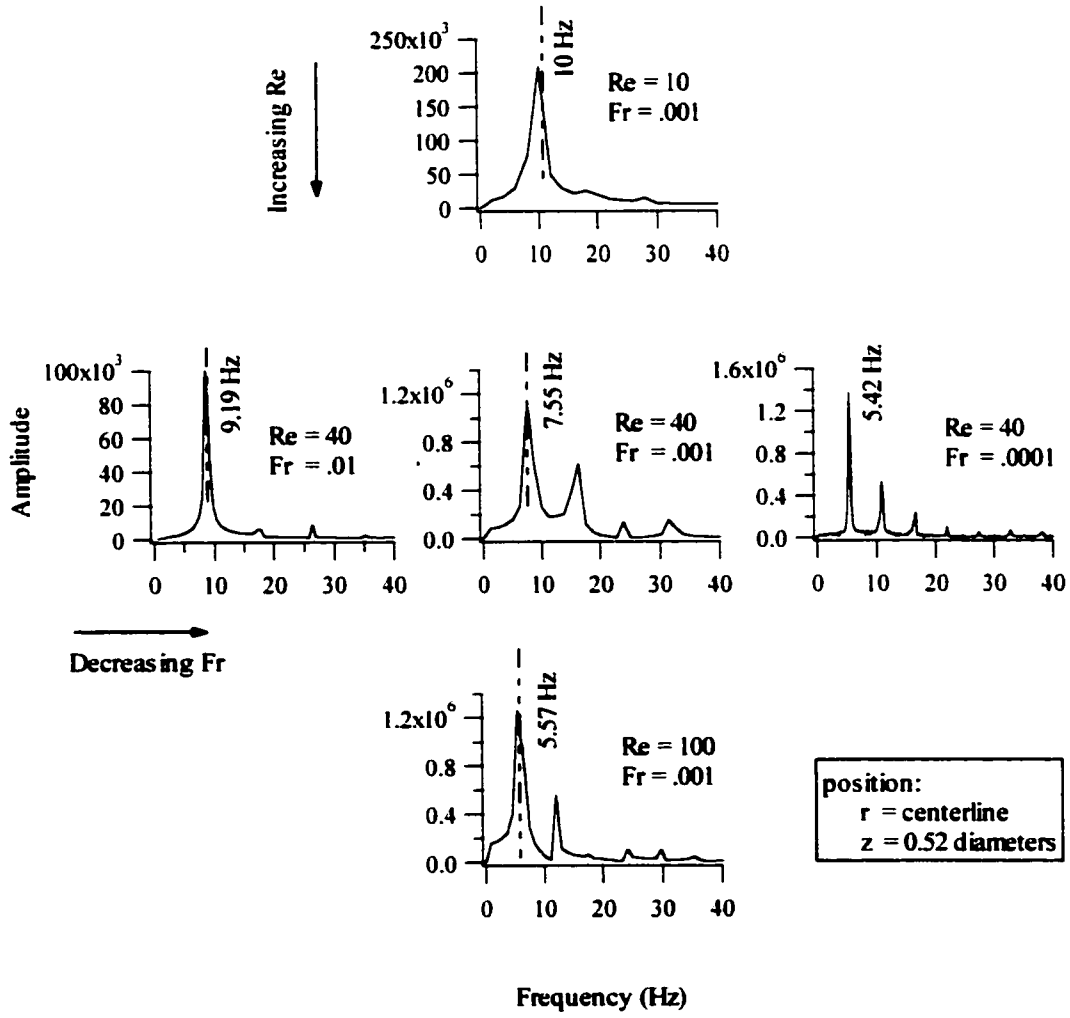

Figure 6.7: Temperature frequency spectrum for various Froude and Reynolds number.

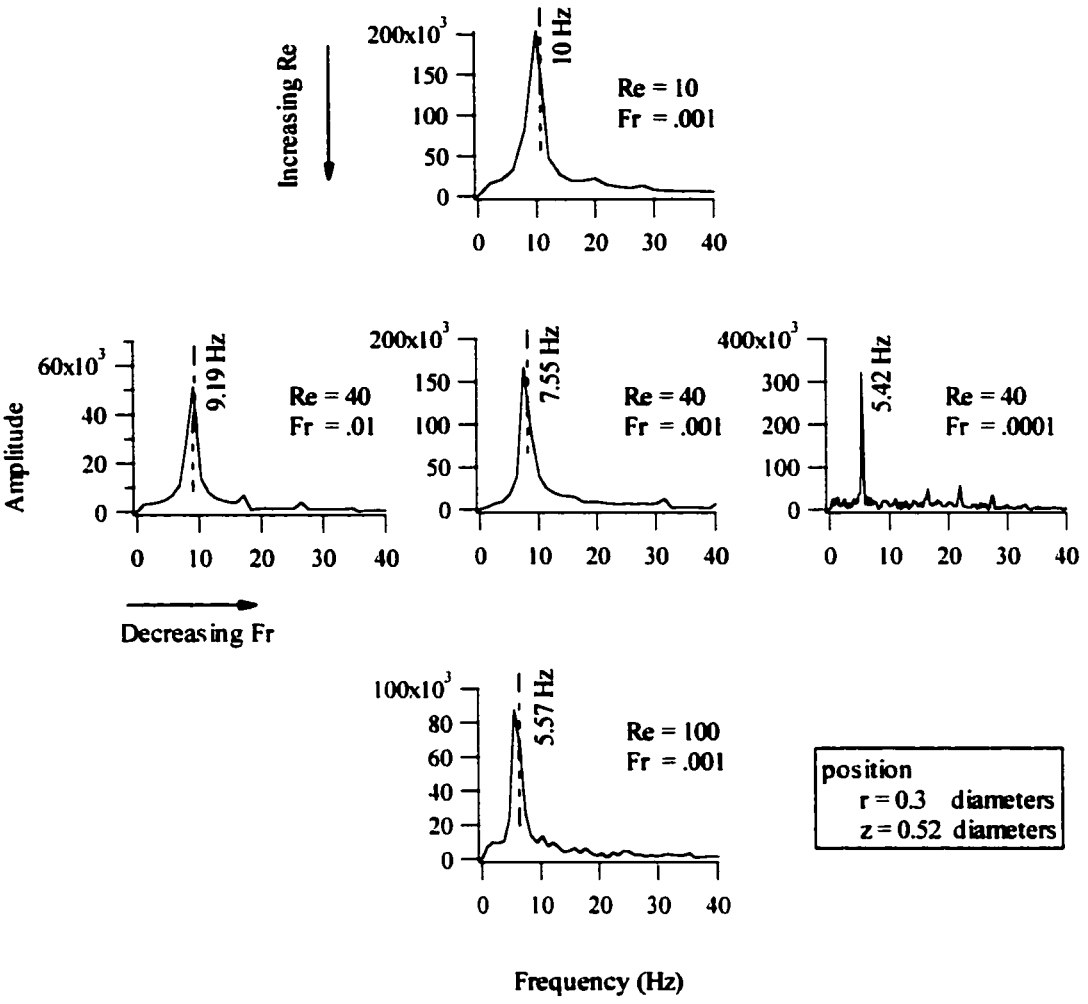

Figure 6.8: Temperature frequency spectrum for various Froude and Reynolds number.

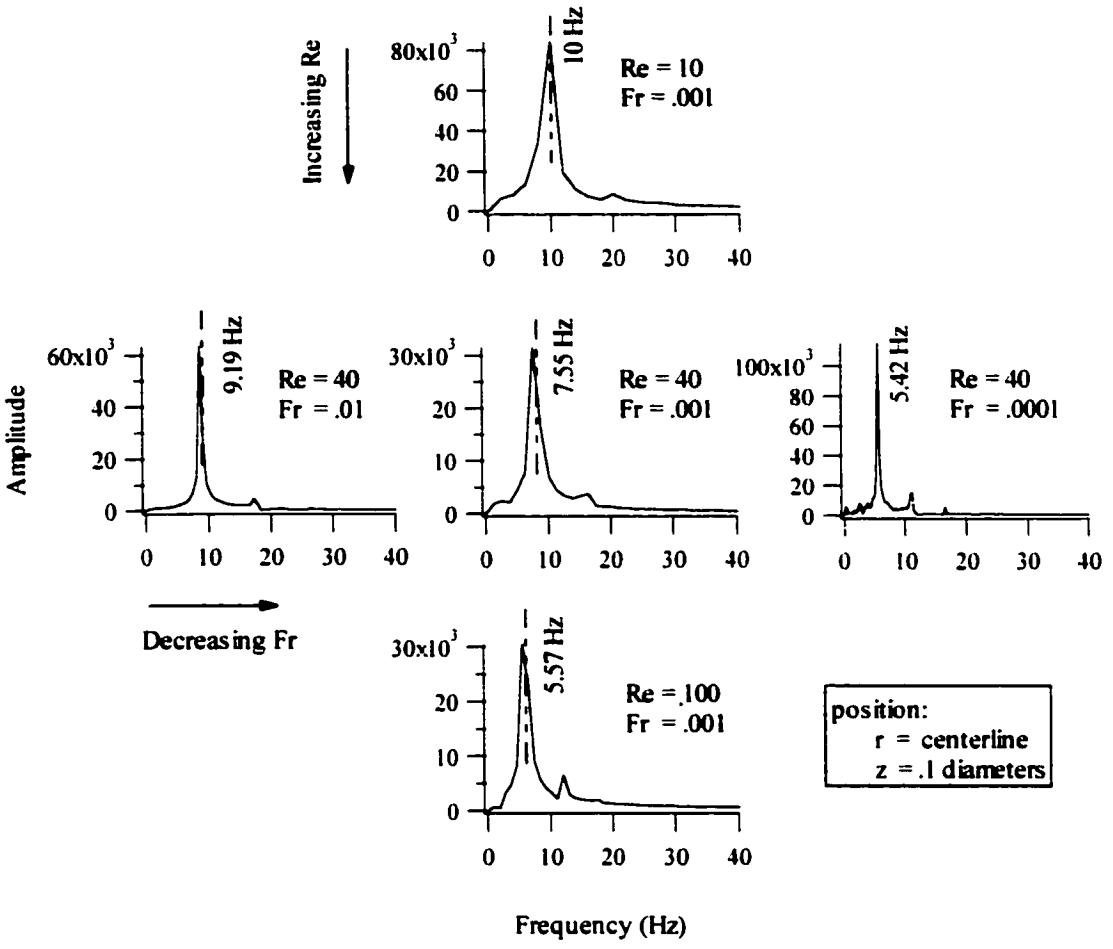

Figure 6.9: Temperature frequency spectrum for various Froude and Reynolds number.

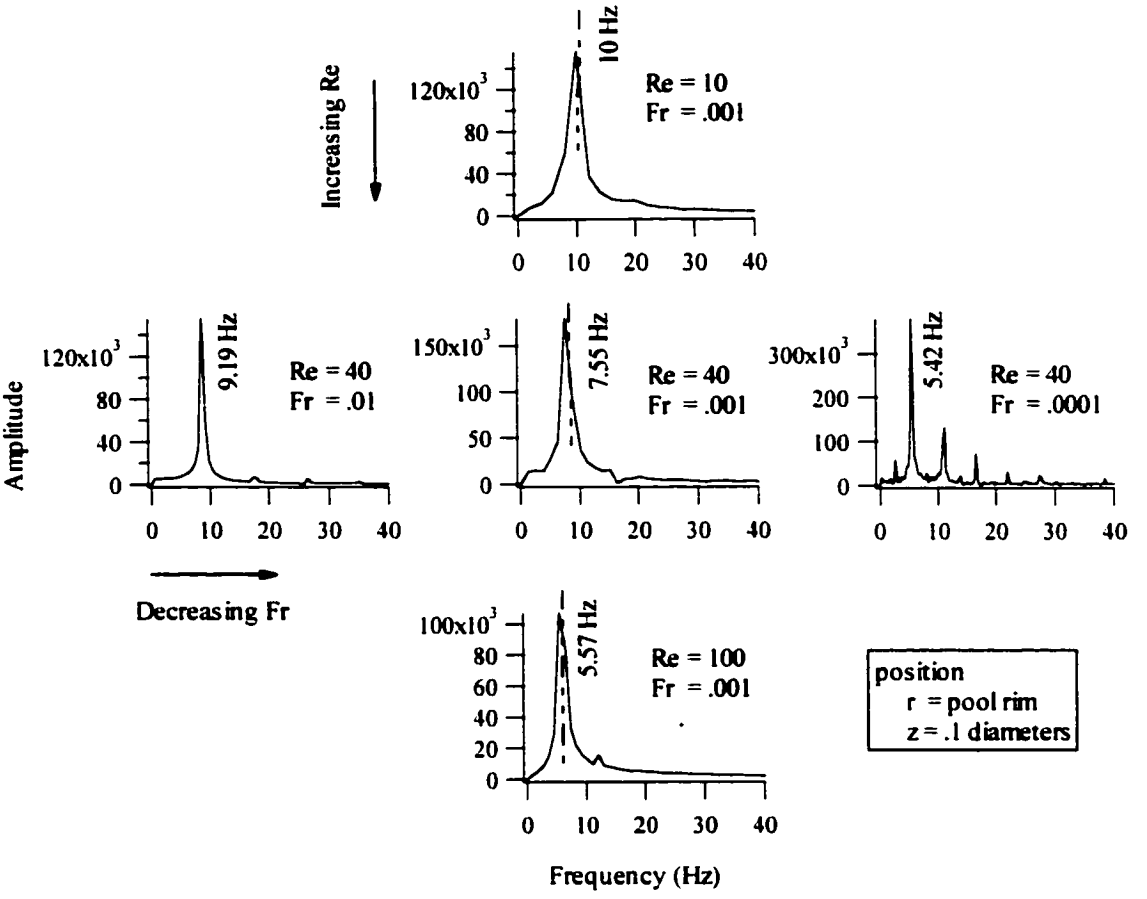

Figure 6.10: Temperature frequency spectrum for various Froude and Reynolds number.

It can also be seen that harmonics with the highest amplitudes occur at the centerline and axial location of .52 diameters for all cases. At this location, the largest amplitudes of fluctuations occur and increase with decreasing Froude number, and increases with increasing Reynolds number.

The frequency results agree with the experimental finding of Hamins, et al. They found that for methane the Strouhal number (S = fD/v) is proportional to $Fr^{-.55}$. For the results from this work, Strouhal numbers were formed for the cases with constant Reynolds number, but varying Froude number. A curve fit shows $S = .318\ Fr^{-.547}$ in Figure 6.11a. Similarly, Strouhal numbers were formed for the cases with constant Froude number, but varying Reynolds number. Figure 6.11b also shows the Strouhal number to be independent of the Reynolds number past Re = 20, and have a minor dependence for Re < 20. This result agrees with work by Hamins, et al. where it was found that the Strouhal number did not correlate with the Reynolds number. Thus, the results compare well with experiment.

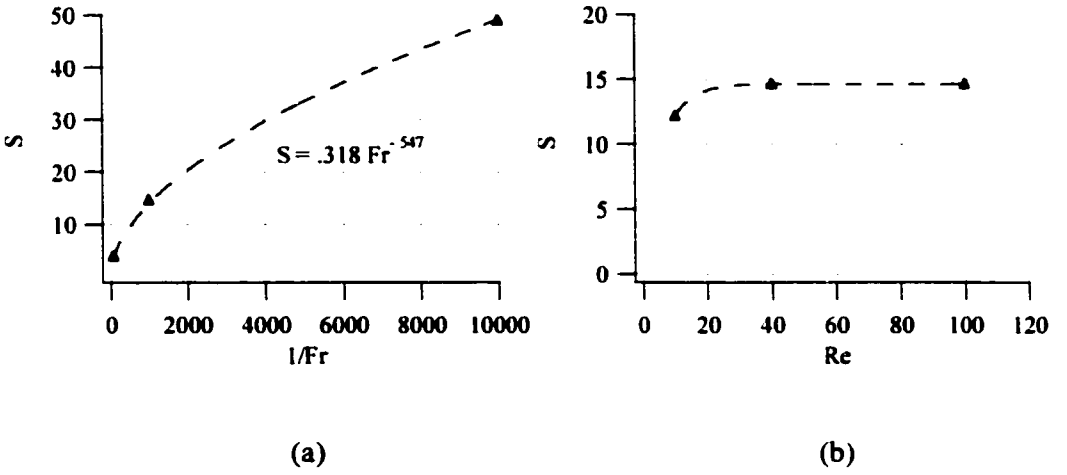

Figure 6.11: Strouhal number as a function of (a) Froude number, and (b) Reynolds number.

6.4 Local Reynolds number

As was previously noted, an axisymmetric simulation is valid only when azimuthal variations are not present, such as when the flow is laminar. Once transition to turbulence occurs the axisymmetric assumption cannot be used. Thus, the current model is applicable only up to a certain elevation above the pool surface for any particular case. The extent of this elevation is dependent upon the parametric values such that it decreases with decreasing source Froude number, and decreases with increasing source Reynolds number. The existence of a transition from laminar to turbulent flow suggests that a local Reynolds number as a function of axial location can be identified. By determining from previous experimental investigations the axial extent for which a flow is laminar, an approximate local Reynolds number for transition can be ascertained. In the following, a local Reynolds number is presented and the results for each case compared.

The local Reynolds number is defined as,

$$Re = \frac{\bar{v} D_e}{\bar{\nu}} \tag{6.3}$$

where,

$\bar{v}$ - axial mean velocity

D_e - effective diameter

$\bar{\nu}$ - mean kinematic viscosity

Quantities are determined by a mass flow average, that is, for any quantity x

$$\bar{x} M = \int_0^\infty x \, \rho v \, 2\pi r \, dr \tag{6.4}$$

where,

$$M = \int_0^\infty \rho v 2\pi r dr \quad \text{(mass flow)} \tag{6.5}$$

Thus, the mass-flow, averaged velocity, $\bar{v}$, and kinematic viscosity, $\bar{\nu}$, are defined as,

$$\bar{v} = \frac{\int_0^\infty \rho v^2 2\pi r dr}{M}, \text{ and} \tag{6.6}$$

$$\bar{\nu} = \frac{\int_0^\infty \rho \nu 2\pi r dr}{M}. \tag{6.7}$$

An effective diameter, D_e, can be determined by defining a volume flow, Q_v, by

$$Q_v = M\bar{\upsilon} = \int_0^\infty v 2\pi r dr = \frac{\pi}{4} D_e^2 \bar{v} \tag{6.8}$$

thus,

$$D_e = \sqrt{\frac{4}{\pi}\frac{Q_v}{\bar{v}}} \tag{6.9}$$

Time-averaged, local values of Reynolds number as a function of axial location are shown for each case in Figure 6.12. The results indicate that the local Reynolds number increases with increasing source Reynolds number, and increases with decreasing source Froude number. The case with the lowest source Froude number, .0001, has the highest values of local Reynolds number at any given axial location. Thus, this case has the lowest axial extent to which the axisymmetric assumption applies.

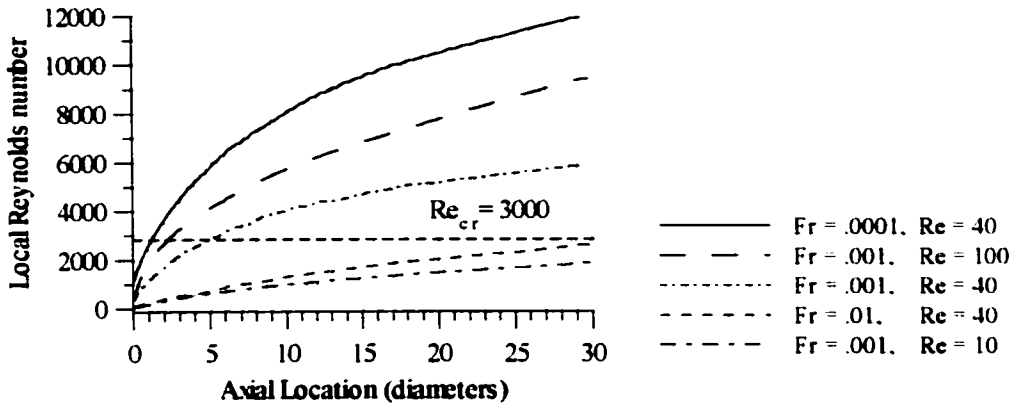

Figure 6.12: Time-averaged, local Reynolds number at various elevations for all cases.

This trend agrees with the experiments done by Blinov and Khudyakov[3] where it was found that the laminar region of the visible flame decreases with decreasing source Froude number. By comparing with experimental work done by other researchers, an approximate critical local Reynolds number for which axial symmetry applies can be determined. The experimental and numerical work done by Mell et al.[22] on a 10-cm-diameter pool fire indicates that an axisymmetric simulation is applicable up to 1 diameter above the pool surface. The case (Fr=.0001, Re=40) which has the highest local values of Reynolds number in Fig. 6.12 corresponds to a diameter of 8.0 cm. Thus, for this diameter the axial extent of validity should be slightly greater than for a 10 cm fire, and thus would be greater than 1 diameter. A local Reynolds number of approximately 3000 corresponds to an axial location of 1.5 diameters for this case. Further evidence, are photographs taken by Sibulkin and Hansen on PMMA pool fires which show that for a 5 cm fire the laminar region goes up to approximately 4 diameters. The case (Fr = .001, Re = 40) corresponds to a 3.75 cm pool fire, thus it would have a greater axial extent of validity than a 5 cm fire. Figure 6.12 shows that for this case an axial extent of 6 diameters corresponds to a local Reynolds of approximately 3000. Additionally, in the work done by Blinov and Khudyakov[3] it was found that for a 1.1 cm pool fire the flame

remains completely laminar, and that for a 3 cm fire the upper part of the flame becomes unstable. Thus, it can be expected that for pool fires under 2 cm in diameter the visible flame is laminar. The cases of (Fr = .001, Re = 10) and (Fr = .01, Re = 40) correspond to pool fire diameters of 1.4 cm and 1.7 cm respectively. Figure 6.12 indicates that if the critical Reynolds is 3000, the flame remains laminar for these two cases. Thus, using the current available experimental evidence, the critical local Reynolds number is approximately 3000. It should be noted that in order to completely substantiate a critical local Reynolds number a rigorous experimental investigation is needed.

6.5 Effect of Fuel Properties

6.5.1 Effect of Heat Release Rate

The following results show the effect of heat release rate on the vorticity production terms, kinetic energy of fluctuations production terms, local Reynolds number, and frequency. Heat release rate, $\dot{Q}$, is defined as the product of the mass of fuel leaving the pool surface per unit time and the heat of combustion. That is,

$$\dot{Q} = \dot{m} H_C = \rho_{in} A v_{in} H_c \tag{6.10}$$

where, ρ_{in}, A, v_{in}, and H_c are the density of the fuel vapors leaving the pool surface, pool surface area, velocity of fuel vapors at pool surface, and heat of combustion respectively. This definition of the heat release rate is theoretical since it is assumed that all of the fuel leaving the pool surface goes towards complete combustion, and that the fuel velocity and density are constant. The actual heat release rate will be less than theoretical due to incomplete combustion, and due to the possibility of some fuel not

taking part in burning. Furthermore, the mass flux at the pool surface can vary in space and time, thus the heat release will be a function of space and time.

The heat release rate can be altered by changing any of the variables in its definition, though in order to maintain a constant Froude and Reynolds number, the pool area and inlet fuel velocity were kept constant. Only the fuel vapor density at the pool surface and the heat of combustion were varied. Changing the inlet fuel vapor density results in a change in inlet fuel temperature. This implies a change in the fuel inlet kinematic viscosity, thereby changing the Reynolds number. In order to preserve the Reynolds number, the kinematic viscosity was held constant by adjusting the dynamic viscosity at the fuel inlet. This cannot be realized in an actual laboratory, since it does not reflect the true kinematic viscosity at the specified fuel inlet temperature. In the following subsections, the first shows results for the effect of heat release rate varied by way of the fuel vapor density at the pool surface. The second subsection shows results for the effect of heat release rate varied by way of the heat of combustion.

6.5.1.1 Inlet Fuel Density Varied

Results are shown for the effect of heat release rate altered by way of the fuel vapor density at the pool surface or the inlet fuel density. The inlet fuel temperature was determined by using this value for density and the ideal gas equation. Thus, a decrease in inlet fuel density indicates a rise in inlet fuel temperature. Table 6.2 specifies heat release rate, corresponding inlet temperatures and densities for each case using methane.

Table 6.2: Heat release rates and inlet temperatures and densities

Fuel	Heat Release Rate (W)	Inlet temperature (K)	Inlet density (kg/m^3)
Methane	200	443	.44
	300	295	.66
	400	221	.88

All cases were run for Fr = .01 and Re = 40. Figure 6.13 shows the time-averaged, spatially integrated, absolute values of the vorticity production terms. The results indicate that these terms are not significantly effected by changes in heat release rate. Similarly, there is negligible difference in the time-averaged, absolute values of vorticity for each case as shown in Figure 6.14.

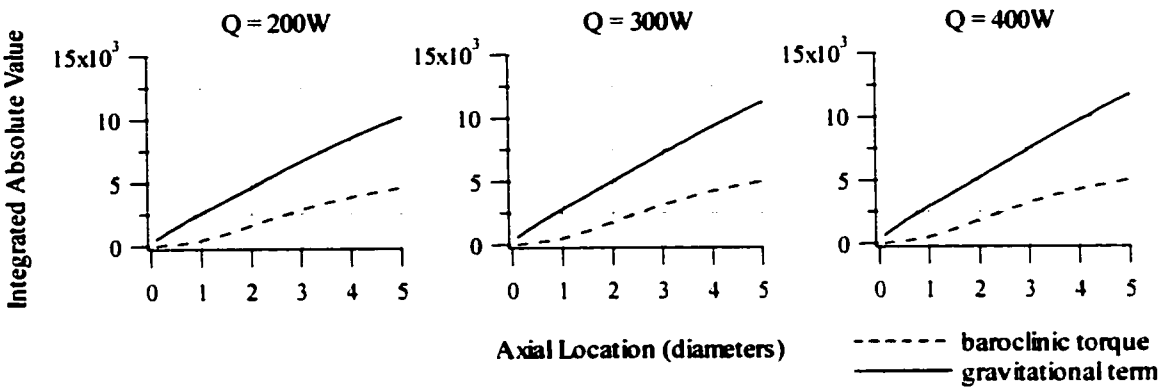

Figure 6.13: Integrated, absolute values of baroclinic torque and gravitational term for heat release rates of 200W, 300W, and 400W. Inlet fuel density varied. Case (Fr=.01, Re = 40).

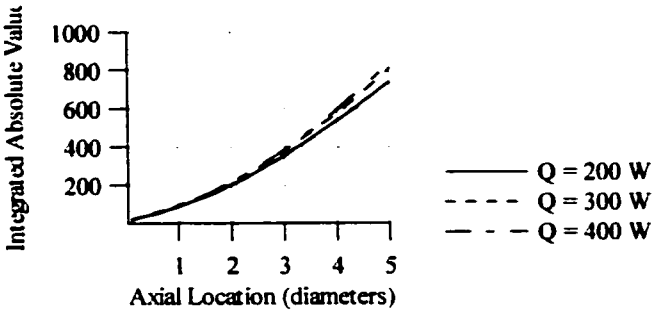

Figure 6.14: Integrated, absolute values of vorticity for heat release rates of 200W, 300W, and 400W. Inlet fuel density varied. Case (Fr=.01, Re=40).

Figure 6.15 shows the spatially integrated values for the kinetic energy of fluctuations production terms. Heat release rate does not influence buoyant production, but does influence shear production. An increase in the heat release rate causes shear production from axial velocity gradients in the radial direction to increase.

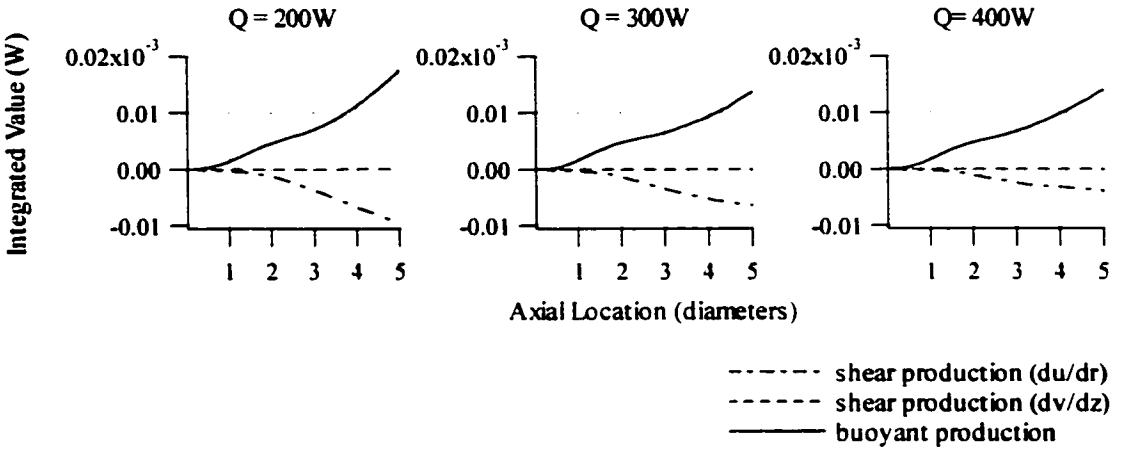

Figure 6.15: Integrated values of shear and buoyancy production for theoretical heat release rates of 200W, 300W, and 400W. Inlet fuel density varied. Case (Fr=.01, Re=40).

The spatially integrated values of kinetic energy of fluctuations are shown in Figure 6.16. The results indicate that the kinetic energy of fluctuations increases with increasing heat release rate.

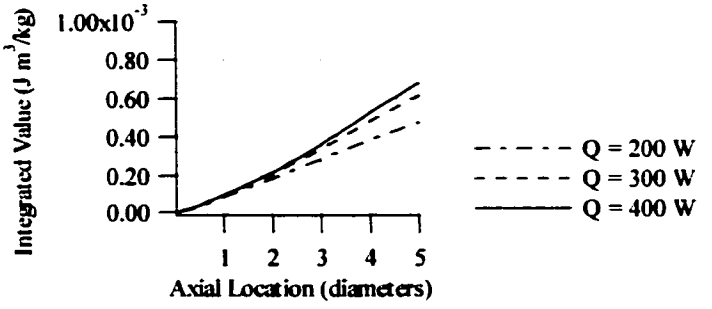

Figure 6.16: Integrated values of kinetic energy of fluctuations for theoretical heat release rates of 200W, 300W, and 400W. Inlet fuel density varied. Case (Fr=.01, Re=40).

The local values of Reynolds number are shown in Figure 6.17. The results indicate that local Reynolds number is not significantly effected by heat release rate.

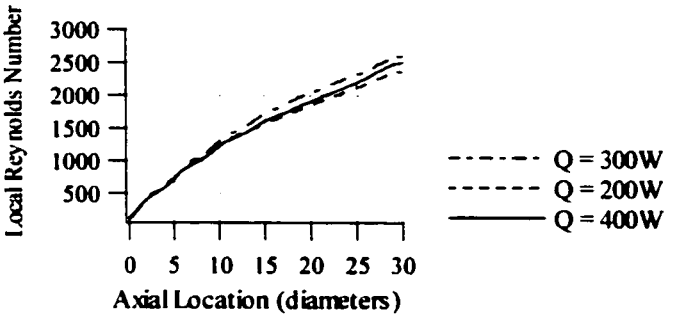

Figure 6.17: Local values of Reynolds number for theoretical heat release rates of 200W, 300W, and 400W. Inlet fuel density varied. Case (Fr=.01, Re=40).

Figure 6.18 shows the frequency spectrum of temperature at a location of z = 0.52 diameters and centerline. The dominant frequency (9.19 Hz), amplitude, and harmonics are not effected by heat release rate.

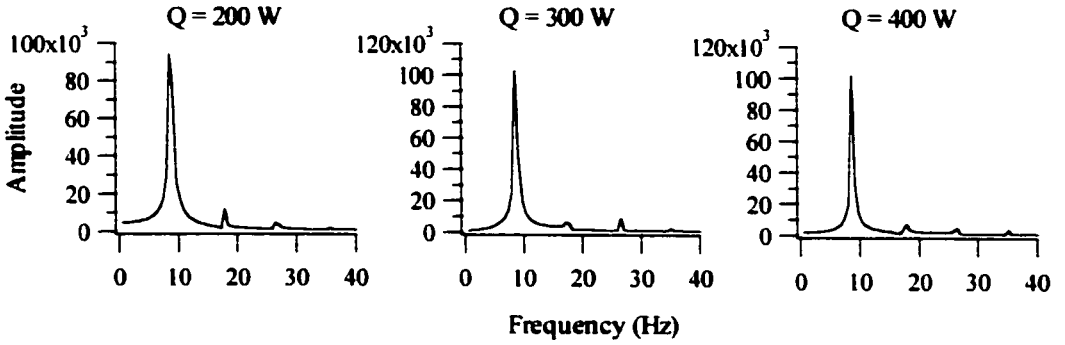

Figure 6.18: Temperature frequency spectrum for theoretical heat release rates of 200W, 300W, and 400W at location of z =0.52 and centerline. Inlet fuel density varied. Case: (Fr=.01, Re=40).

Time-averaged, temperature contours are shown in Figure 6.19. The time-averaged flame-sheet location indicated by the hottest region becomes higher for increasing heat release rate. The trend of this result agrees with the finding of Zukowski[14] and Heskestad[19] that flame height is proportional to heat release rate. Thus, an increase in flame height is expected for an increase in the heat release rate.

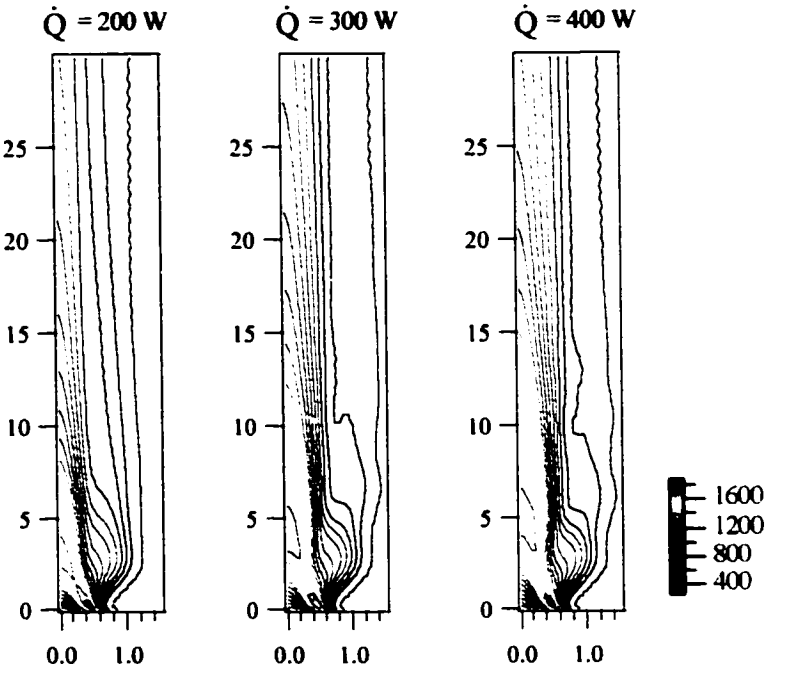

Figure 6.19: Time-averaged, temperature contours for theoretical heat release rates of 200W, 300W, and 400W. Inlet fuel density varied. Dimensions are in diameters. Case: (Fr=.01, Re=40).

6.5.1.2 Heat of Combustion Varied

Results are shown for the effect of heat release rate altered by way of the heat of combustion. The flame temperature is changed as a result. It should be noted that all other cases performed in this work have similar maximum flame temperature. Flame temperature is altered only in this section. Results show a comparison between heat release rates of 200 and 300 W, as well as the case for heat release varied by way of fuel inlet density with a heat release rate of 200 W. This is provided in order to compare the difference between the two methods of altering the heat release rate. Inlet fuel temperature and density are respectively 295 K and .66 kg/m^3 for the case varied by heat of combustion. Figure 6.20 shows the time-average, integrated absolute values of the vorticity production terms. The results show that flame temperature has an effect on these terms, but not heat release rate. The vorticity production terms decrease as the flame temperature is decreased. Similarly, Figure 6.21 showing the integrated, absolute values of vorticity indicate that flame temperature has a greater effect than heat release rate on vorticity. Thus, flame temperature is an influential parameter effecting flame dynamics.

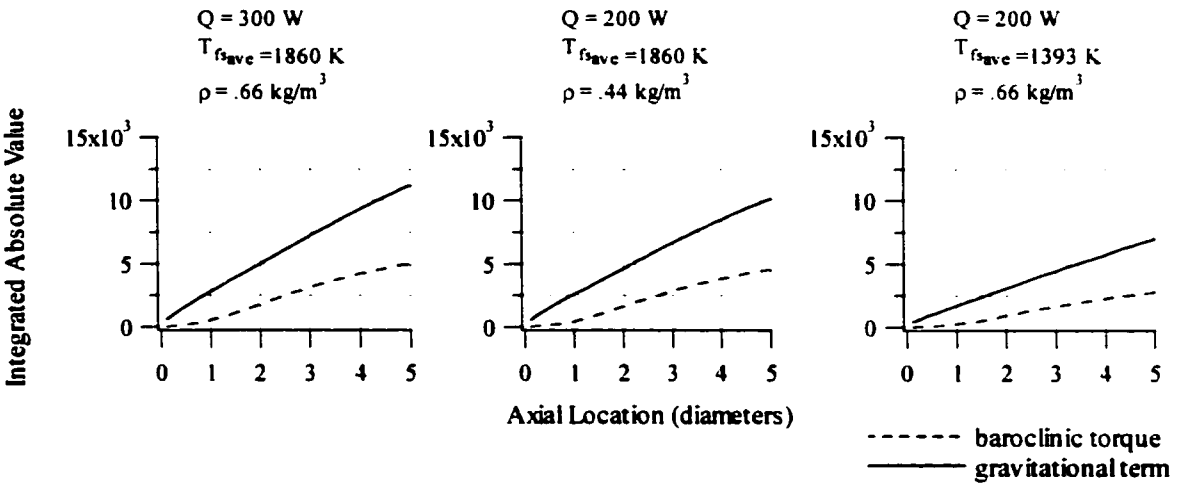

Figure 6.20: Integrated, absolute values of vorticity production terms. Heat release, average flame-sheet temperature, and inlet fuel density is indicated. Case (Fr = .01, Re = 40)

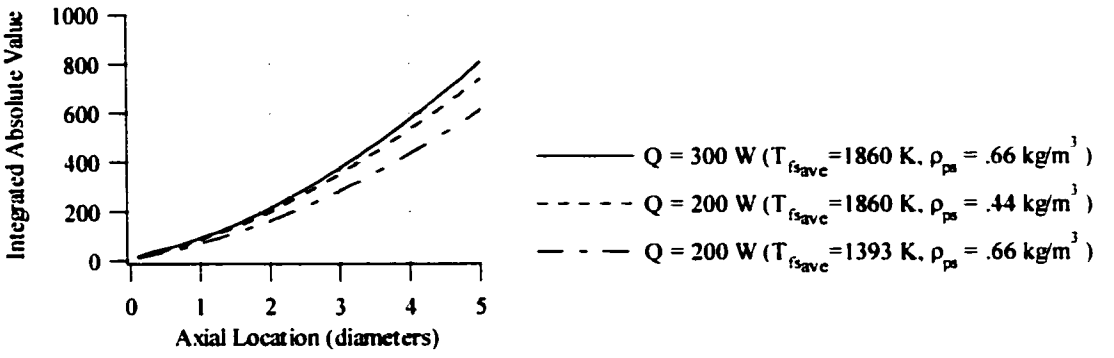

Figure 6.21: Integrated, absolute values of vorticity. Heat release, average flame-sheet temperature, and inlet fuel density is indicated. Case (Fr = .01, Re = 40)

Figure 6.22 shows the integrated values of shear and buoyancy production of kinetic energy of fluctuations. The results indicate that for a 25% change in average flame-sheet temperature there is a negligible change in the shear and buoyancy production from the case with equivalent heat release. The flame temperature does effect the kinetic energy of fluctuations as shown in Figure 6.23. The time-averaged, integrated values of kinetic energy of fluctuations decrease with decreasing flame temperature.

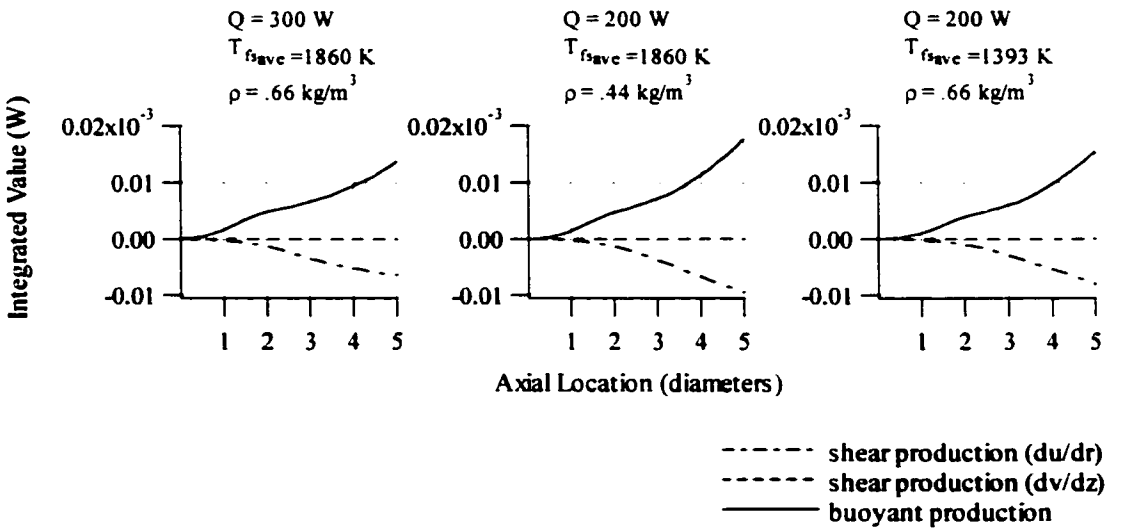

Figure 6.22: Integrated values of shear and buoyancy production of kinetic energy of fluctuations. Heat release, average flame-sheet temperature, and inlet fuel density is indicated. Case (Fr = .01, Re = 40)

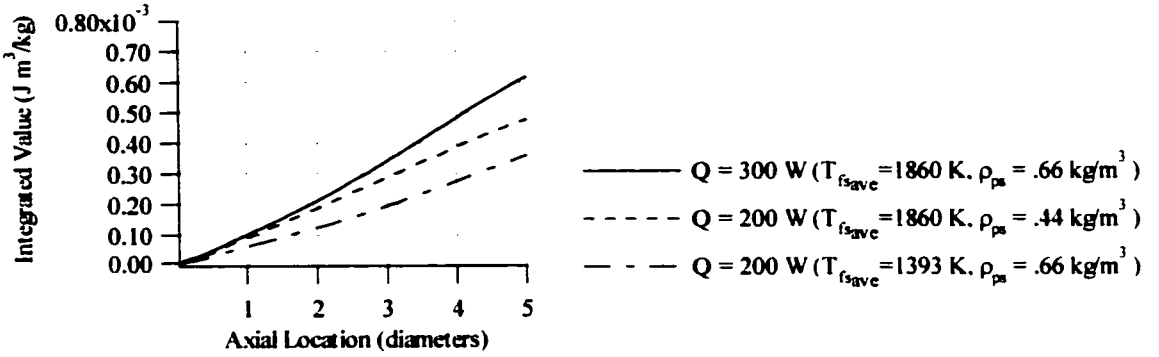

Figure 6.23: Integrated values of kinetic energy of fluctuations. Heat release, average flame-sheet temperature, and inlet fuel density is indicated. Case: (Fr = .01, Re = 40)

Results showing the local Reynolds number values in Figure 6.24 indicate that flame temperature does not effect these values significantly. Results showing the temperature frequency spectra at location of z = .52 diameters and centerline in Figure 6.25 indicate that the dominant frequency is not effected by flame temperature. The amplitude does change with heat release rate.

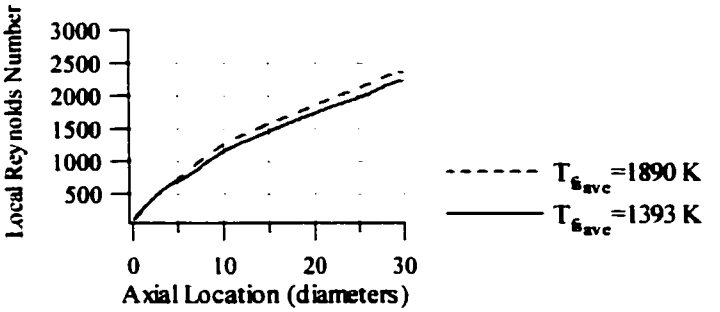

Figure 6.24: Local values of Reynolds number. Average flame-sheet temperature is indicated. $\dot{Q}$= 200 W. Case: (Fr = .01, Re = 40)

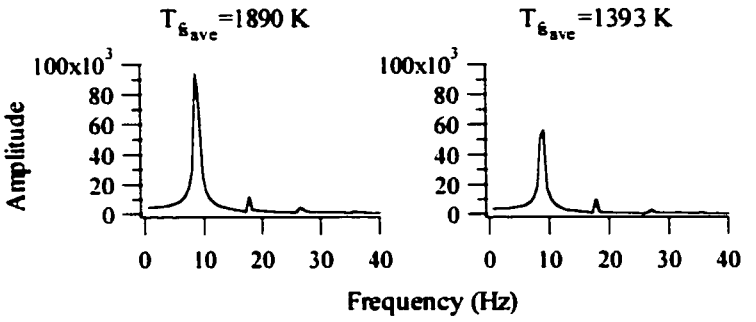

Figure 6.25: Temperature frequency spectrum at location z = .52 diameters and centerline. Average flame-sheet temperature is indicated. $\dot{Q}$ = 200 W. Case: (Fr = .01, Re = 40)

Figure 6.26 shows the time-averaged temperature contours for average flame-sheet temperatures of 1393 K and 1890 K. Both cases have equivalent heat release rates of 200W. The figures show that the average flame-sheet location is similar for both cases. Due to the higher average flame temperature, the case for average T_{fs}= 1890 K is more radially diffused than the case for average T_{fs}=1393 K.

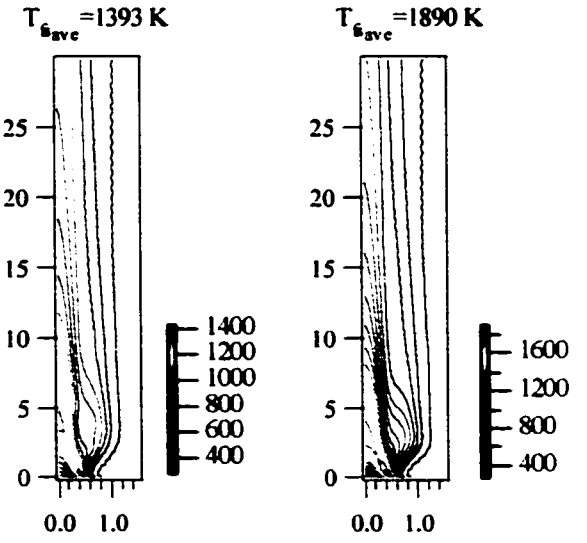

Figure 6.26: Time-averaged, temperature contours. $\dot{Q}$= 200 W. Dimensions are in diameters. Case: (Fr = .01, Re = 40)

6.5.2 Fuel Molecular Weight

The effect of fuel molecular weight on vorticity generation, energetics, and frequency spectrum was also investigated for the parametric case of (Fr =.01, Re = 40). In order to ascertain only the effect of fuel molecular weight, fuels were chosen that have similar air-fuel ratios. The fuels compared are methane, ethane, and propane. Methane is lighter than air, and propane is heavier than air. Thus, the effect of molecular weight different from ambient can be ascertained. These fuels have different viscosities and densities, thus the inlet temperature was adjusted to preserve the source Reynolds number. By changing the inlet fuel density and preserving the Reynolds number, a change in heat release occurs. The results shown previously in section 6.5.1.1 indicate the isolated effect of heat release rate. Thus, the difference between the results that follow in this section and the results for heat release rate varied by way of inlet fuel density can be utilized to ascertain the effect of fuel molecular weight. It should be noted that the Reynolds number could have been artificially preserved by altering the inlet viscosities of the different fuels, but the intent was to simulate conditions that could be realizable in a laboratory. Table 6.3 shows the fuel properties and inlet conditions used. The spatially integrated, absolute values of baroclinic torque and the gravitational term for these fuels are shown in Figure 6.27. The spatially integrated, absolute values of vorticity are shown in Figure 6.28 for each case. The results indicate that fuel molecular weight does not appreciably effect vorticity or its production terms. This was also true for the effect of heat release rate in section 6.5.1.1.

Table 6.3: Fuel properties and inlet conditions for methane, ethane and propane

Fuel	MW	λ	T_{in} (K)	ρ_{in} (kg/m^3)	Heat Release Rate (W)
Methane	16	17.3	293	.66	300
Ethane	30	16.1	455	.80	363
Propane	44	15.7	610	1.2	545

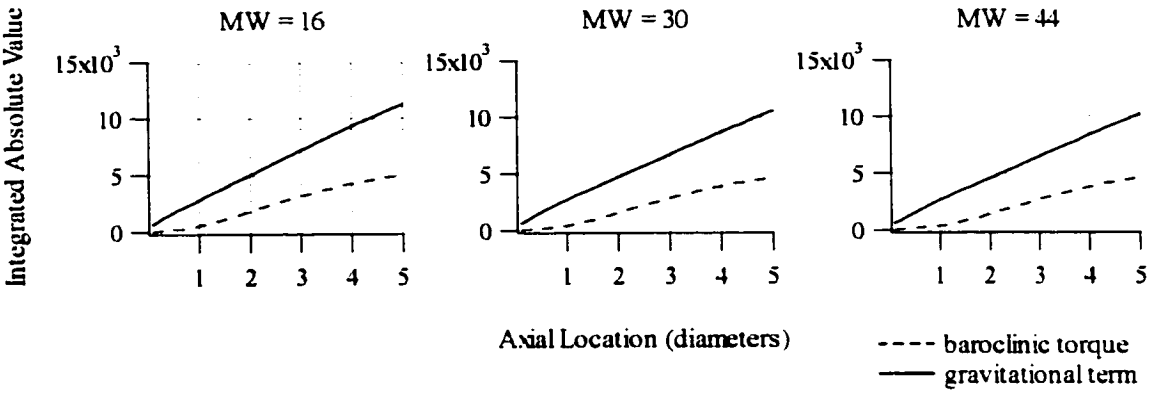

Figure 6.27: Integrated, absolute values of baroclinic torque and gravitational term for different fuel molecular weights. Case (Fr=.01, Re = 40)

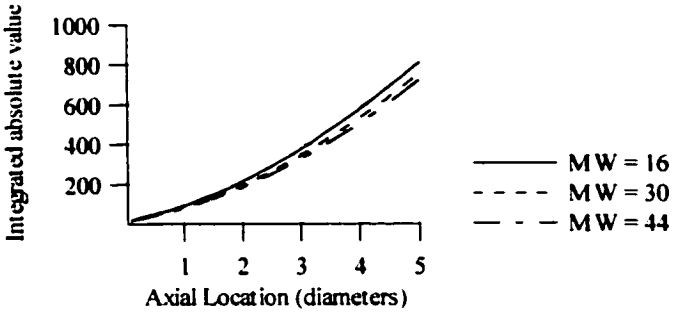

Figure 6.28: Integrated, absolute values of vorticity for different fuel molecular weights. Case (Fr=.01, Re = 40).

Figure 6.29 shows integrated values of shear and buoyancy production of kinetic energy of fluctuations for increasing fuel molecular weight. The buoyant production term is not appreciably effected by fuel molecular weight, nor was it by heat release rate. There is a slight increase in the buoyant production term for MW = 44 above approximately 1 diameter. The shear production term from axial velocity gradient in the radial direction slightly decreases with a fuel molecular weight lighter than air. This can be seen by considering the shear production term for MW = 30. The heat release rate is reduced by 63 W for MW = 16, which should result in a decrease of approximately 10%

from the results obtained in section 6.5.1.1, but the figure shows that it decreases by more than that. Thus, this additional decrease can be attributed to the change in molecular weight lighter than air. This is also the case for a fuel molecular weight heavier than air. The heat release rate is increase by 182 W, which should result in an increase of almost 50%, but instead it shows negligible change in Figure 6.29 for MW = 44. Thus, a fuel molecular weight heavier than air causes the shear production term to decrease. The shear production term from radial velocity gradients in the axial direction is negligible for all cases.

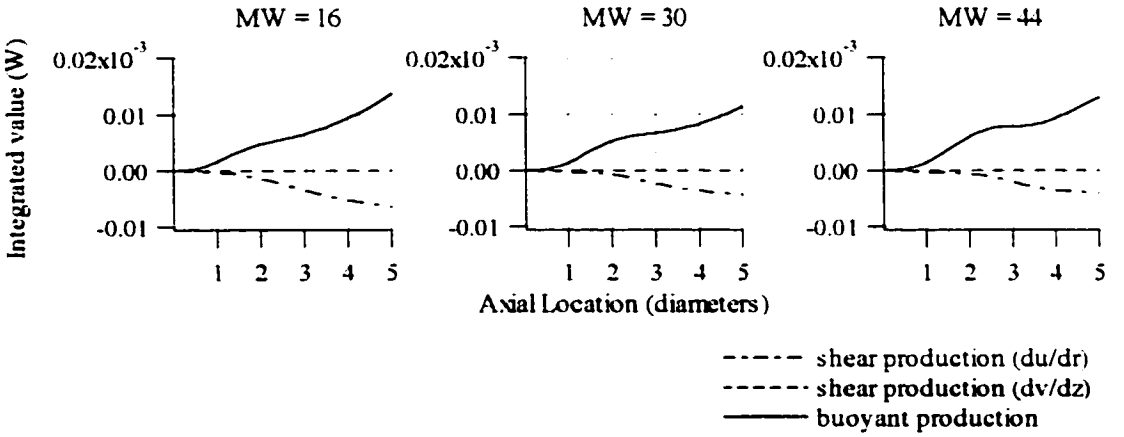

Figure 6.29: Total and radially integrated values of shear and buoyancy production for different fuel molecular weights. Case (Fr=.01, Re = 40).

Figure 6.30 shows the integrated values for the kinetic energy of fluctuations for the various fuel molecular weights. The kinetic energy of fluctuations decreases slightly with increasing fuel molecular weight even though the heat release is increasing. Increasing heat release was found to increase these values. Thus, fuel molecular does effect the kinetic energy of fluctuations. For a fuel lighter than air the kinetic energy of fluctuations increases slightly, and for a fuel heavier than air it decreases, but it both cases the change is not great. For a 175% change in fuel molecular weight the maximum change in kinetic energy of fluctuations is 25%.

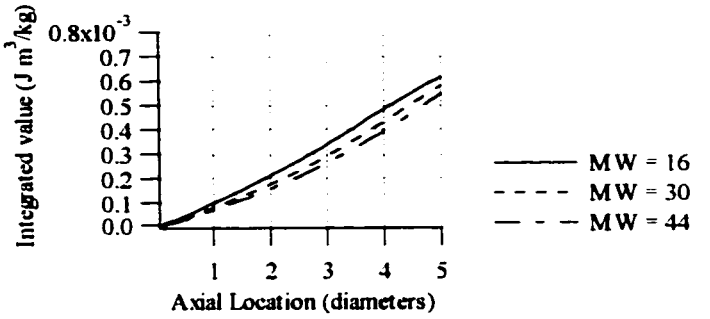

Figure 6.30: Integrated values of kinetic energy of fluctuations for different fuel molecular weights. Case (Fr=.01, Re = 40).

Figure 6.31 shows the local Reynolds number as a function of axial extent for various fuel molecular weights. The local Reynolds number has negligible variation with fuel molecular weight.

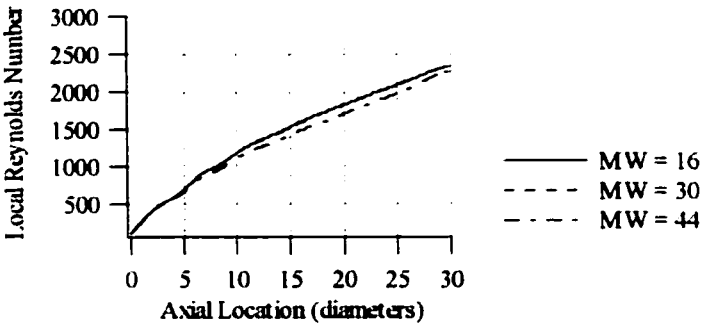

Figure 6.31: Local Reynolds at different axial locations for various fuel molecular weights. Case (Fr=.01, Re = 40).

Figure 6.32 shows a comparison of temperature frequency spectra for various fuel molecular weights at a location of z = .52 diameters and centerline. The dominant frequency of 9.19 Hz does not change with fuel molecular weight. The amplitude of the fluctuations decreases with increasing fuel molecular weight.

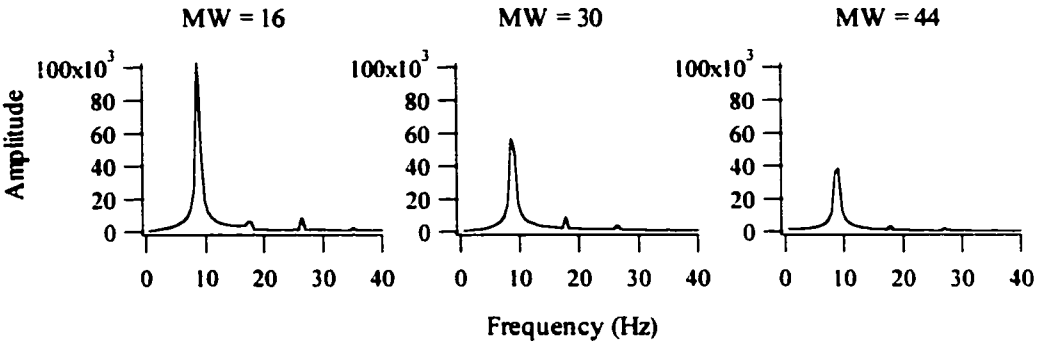

Figure 6.32: Temperature frequency spectra for various fuel molecular weights at location of z =0.52 and centerline. Case (Fr=.01, Re = 40).

Time averaged temperature contours are shown in Figure 6.33. The height of the time-averaged flame-sheet is similar for all cases. It would be expected that since the heat release rate is increasing as the fuel molecular weight is increased that the flame height should increase, but the increasing fuel molecular weight is counteracting this effect. Thus, increasing fuel molecular weight tends to decrease flame height.

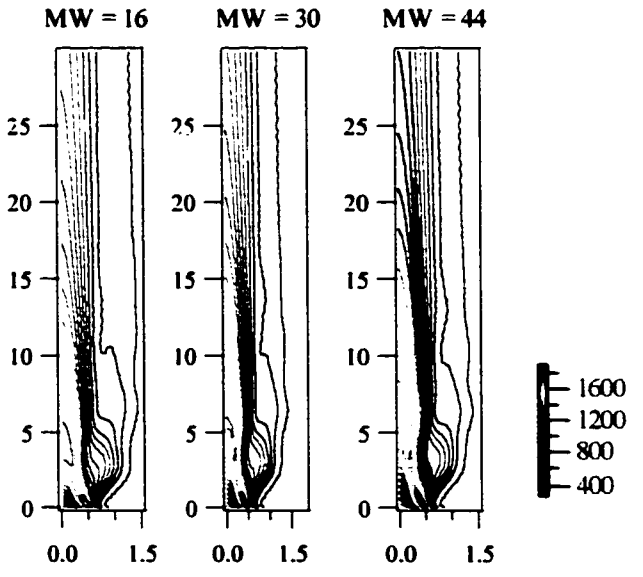

Figure 6.33: Temperature frequency spectra for various fuel molecular weights at location of z =0.52 and centerline. Case (Fr=.01, Re = 40).

6.5.3 Effect of Air-Fuel Ratio

The effect of the air-fuel ratio on vorticity generation, energetics, and frequency spectrum was also investigated for the parametric case of (Fr =.01, Re = 40). The air-fuel ratio is defined as

$$\lambda = \frac{\nu_0 MW_O}{\nu_F MW_F} \tag{6.11}$$

The two cases for comparison have a fuel molecular weight of 30. The maximum flame temperature for both cases is approximately 2000K. Carbon monoxide is mixed with methanol to have a molecular weight of 30 and an air-fuel ratio of 4.6 by mass. This case is compared with ethane with an air-fuel ratio of 16.1. The Reynolds number was preserved by changing the inlet viscosity. Heat release rate, inlet fuel temperature and density, as well as flame-sheet temperature are equal for both cases. Figure 6.34 shows the time-averaged, integrated, absolute values of baroclinic torque and the gravitational term. Both terms decrease with decreasing air-fuel ratio, though the change is not large for such a significant change in air-fuel ratio. This is also true for the time-averaged, integrated, absolute values of vorticity shown in Figure 6.35. Thus, the air-fuel ratio does not have a great influence on the vorticity, and the vorticity production terms.

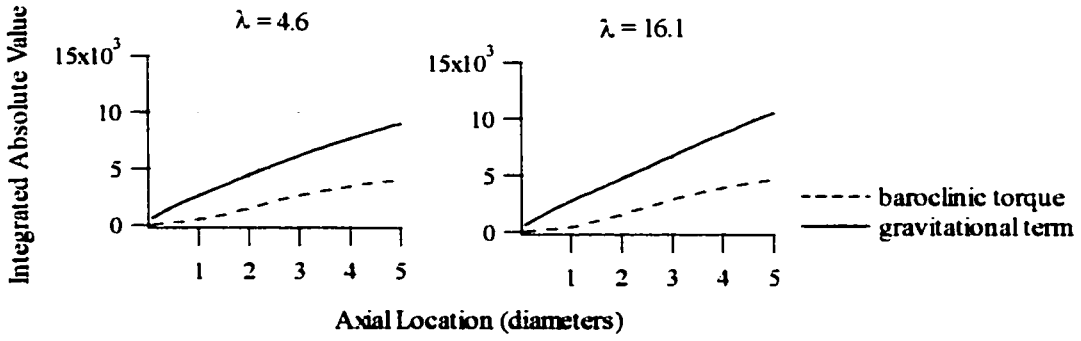

Figure 6.34: Integrated, absolute values of baroclinic torque and gravitational term for air-fuel ratio of 4.6 and 16.1. Case (Fr=.01, Re = 40).

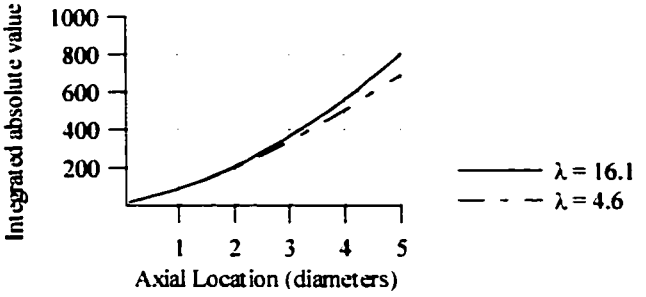

Figure 6.35: Integrated, absolute values of vorticity for air-fuel ratio of 4.6 and 16.1. Case (Fr=.01, Re = 40).

Figure 6.36 shows the integrated value of shear and buoyancy production for different air-fuel ratios. The buoyant production terms increases with a decrease in air-fuel ratio, whereas the shear production term from axial velocity gradients in the radial direction decreases. The shear production term from radial velocity gradients in the axial direction is negligible for both cases. Integrated values of kinetic energy of fluctuations for both air-fuel ratio cases are shown in Figure 6.37. The kinetic energy of fluctuations decreases with a decrease in air-fuel ratio for elevations greater than 2 diameters.

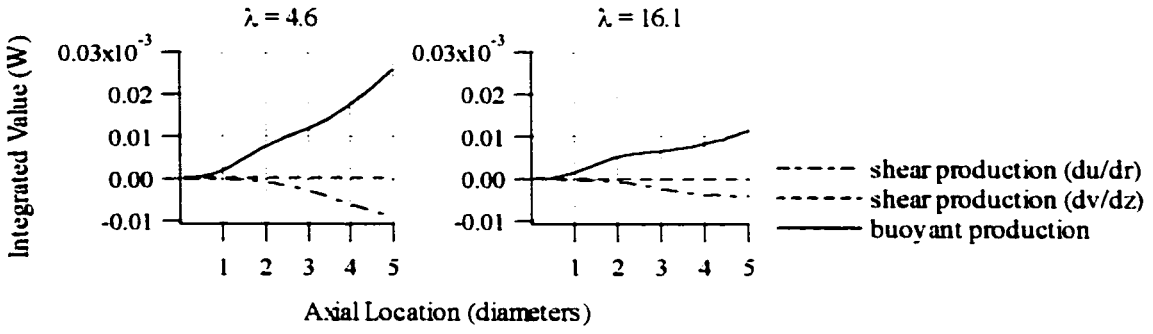

Figure 6.36: Integrated values of buoyancy and shear production for air-fuel ratio of 4.6 and 16.1. Case (Fr=.01, Re = 40).

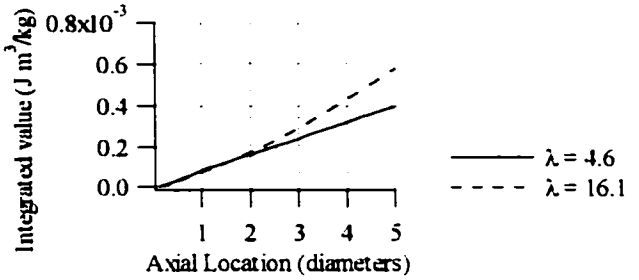

Figure 6.37: Integrated values of kinetic energy of fluctuations for air-fuel ratio of 4.6 and 16.1. Case (Fr=.01, Re = 40).

Temperature frequency spectra comparing air-fuel ratios of 4.6 and 16.1 are shown in Figure 6.38. The results indicate that the dominant frequency at z = 0.52 and centerline does not change with air-fuel ratio. The amplitude greatly increases for λ = 4.6. The time-averaged temperature contours in Figure 6.40 indicate that the average flame-sheet height is much lower for λ = 4.6, thus the point at which the frequency is sampled is nearer to the flame-sheet where larger amplitude fluctuations occur.

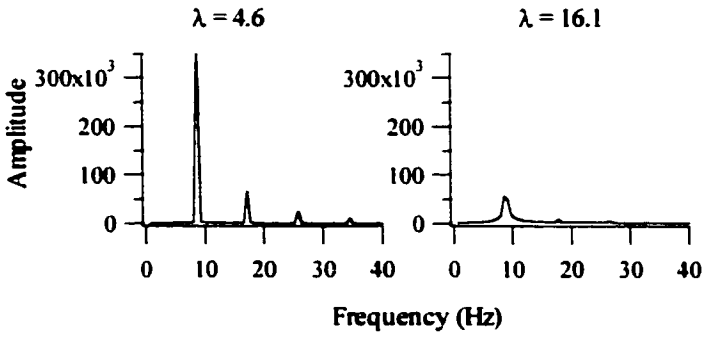

Figure 6.38: Temperature frequency response for air-fuel ratio of 4.6 and 16.1 at location of z =0.52 and centerline. Case: Fr(.01), Re(40).

Time-averaged, local values of Reynolds number for $\lambda = 4.6$ and 16.1 are shown in Figure 6.39. Air-fuel ratio does not significantly effect these values.

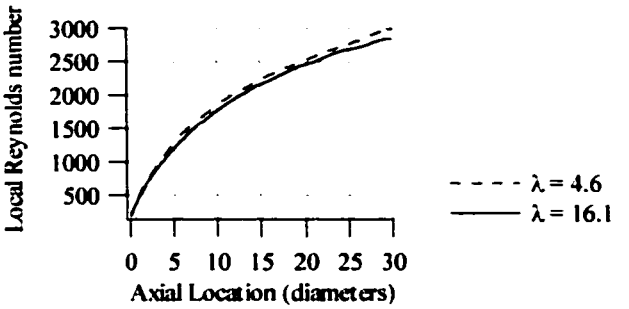

Figure 6.39: Local Reynolds and Froude number at different axial locations for air-fuel ratio of 4.6 and 16.1. Case (Fr=.01, Re = 40).

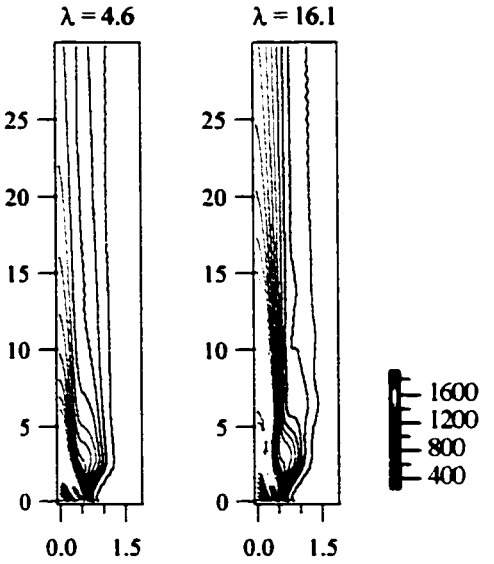

Figure 6.40: Time-averaged temperature contours for air-fuel ratio of 4.6 and 16.1. Dimensions are in diameters. Case: Fr(.01), Re(40).

6.6 Effect of Inlet Velocity Profile

As noted earlier, the fuel velocity at the pool surface is not spatially uniform and can vary with time for pool fires. Akita and Yumoto[1] measured the burning rates of liquid methanol pool fires and found that the burning rate is higher at the pool rim. For a 5.33 cm diameter fire, the burning rate was approximately 5 times higher at the rim than in the center of the pool. For a 14.4 cm diameter fire, the burning rate was approximately 2 times higher at the rim than in the center of the pool. The work performed by Kuldeep, et al.[26] on the condensed and gas phase regions of a 1.1 cm pool fire, indicate that velocities at the pool rim are ~20 times greater than those at the inner regions. The velocity profile appears exponential, with approximately constant velocities within 0.4 radii, then increasing to a maximum value at the pool rim. This is due to flame attachment at the pool rim. As the pool diameter is decreased, the difference between pool rim velocities and inner region velocities increase. To further test whether pool like gas fires have similar flame dynamics as pool fires, the effect of an inlet fuel velocity profile reflecting flame attachment is investigated, and the results are presented in this section. These results should go in Chapter 5 for model validation, but are presented here due to the discussion provided in this chapter concerning the dynamics of interest. The following cases are for methane and (Fr = .01, Re = 40). The boundary condition for the inlet fuel velocity is specified as

$$v_{in} = 0.145 * \exp((2.14\,r)^5)^3, \quad 0 \le r \le 0.5 \text{ diameters} \tag{6.12}$$

This function, along with the constant velocity profile, is shown in Figure 6.41. This velocity profile was chosen so that the dimensionless, area-weighted, average velocity is 1. The constants in equation (6.12) can be varied to satisfy this condition since the average can change depending on how the grid is stretched. For the discrete radial

locations specified by the chosen grid, the velocity values at the pool rim are ~20 times higher than the values under .4 radii.

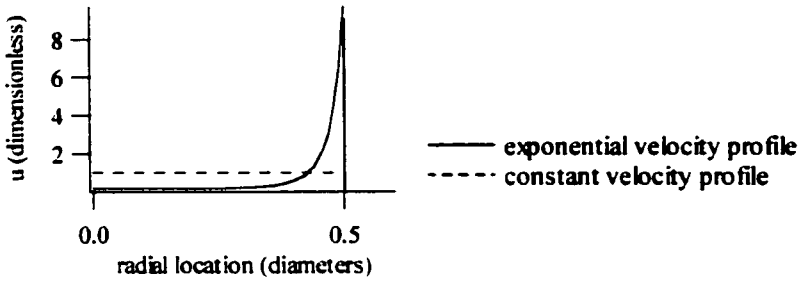

Figure 6.41: Comparison of inlet fuel velocity profiles.

A pool rim velocity of this magnitude was chosen because the diameter for this case, 1.7 cm, is close to that of the diameter investigated by Kuldeep, et. al., 1.1 cm. Figure 6.42 shows the spatially integrated, absolute values of the vorticity production terms. The results indicate an exponential velocity profile does not appreciably effect these terms. This is also the case for the spatially integrated, absolute values of vorticity as shown in Figure 6.43.

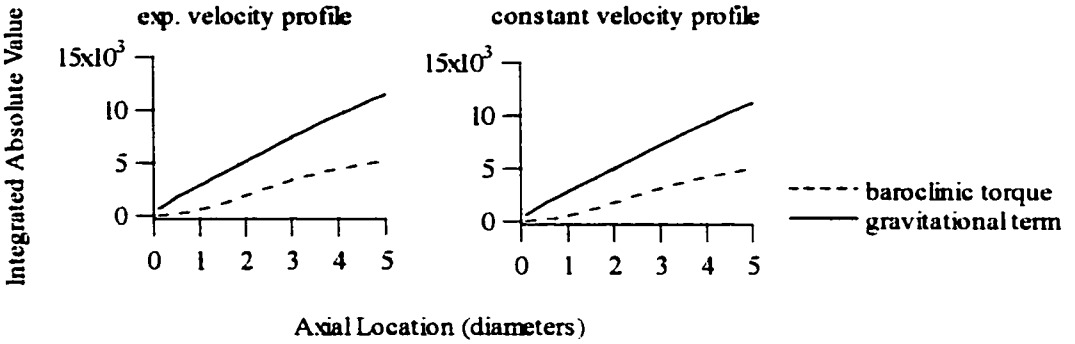

Figure 6.42: Spatially integrated, absolute values of vorticity production terms for an exponential and constant velocity profile. Case: (Fr = .01, Re = 40).

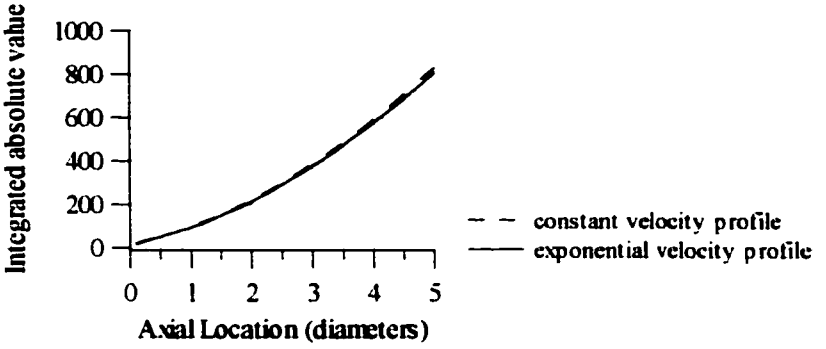

Figure 6.43: Spatially integrated, absolute values of vorticity for an exponential and constant velocity profile. Case: (Fr = .01, Re = 40).

The spatially integrated values of kinetic energy of fluctuations production terms shown in Figure 6.44 indicate that an exponential inlet velocity profile does not effect the buoyant production. Shear production due to axial velocity gradients in the radial direction show a minor increase at an elevation around 4 diameters, but is unaffected at lower elevations. The spatially integrated values of kinetic energy of fluctuations shown in Figure 6.45 indicate that an exponential inlet velocity profile does not effect these values.

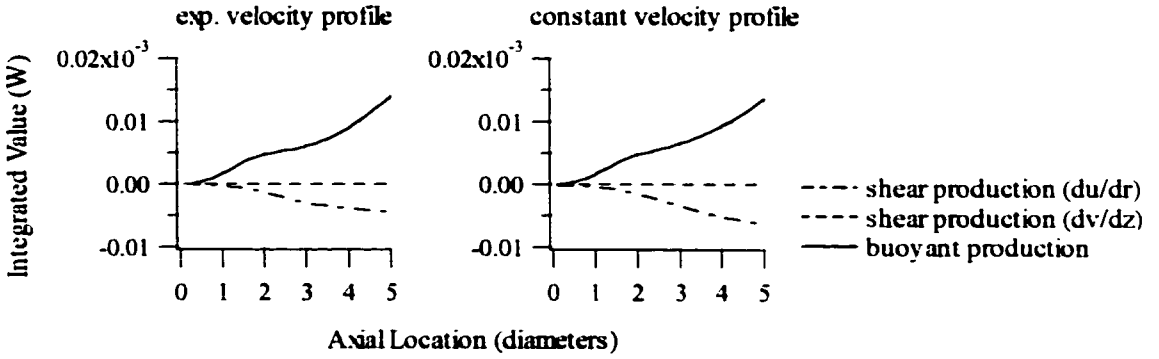

Figure 6.44: Spatially integrated values of kinetic energy of fluctuations production terms for an exponential and constant velocity profile. Case: (Fr = .01, Re = 40).

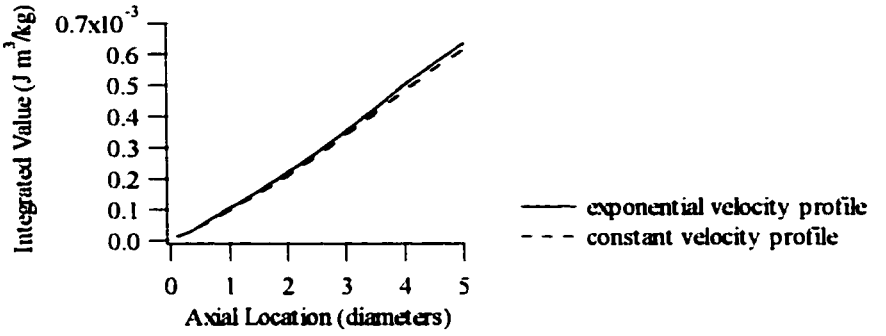

Figure 6.45: Spatially integrated values of kinetic energy of fluctuations for an exponential and constant velocity profile. Case: (Fr = .01, Re = 40).

The time-averaged, local Reynolds number shown in Figure 6.46 indicates that an exponential inlet velocity profile does not effect these values. This is also true of the temperature frequency spectra shown in Figure 6.47.

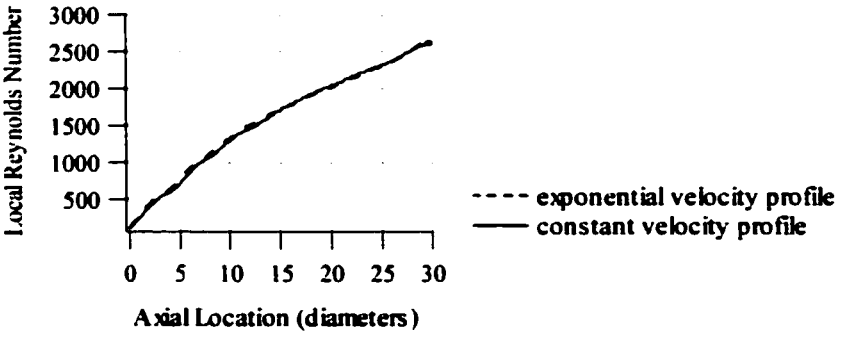

Figure 6.46: Time-averaged, local values of Reynolds number for an exponential and constant velocity profile. Case: (Fr = .01, Re = 40).

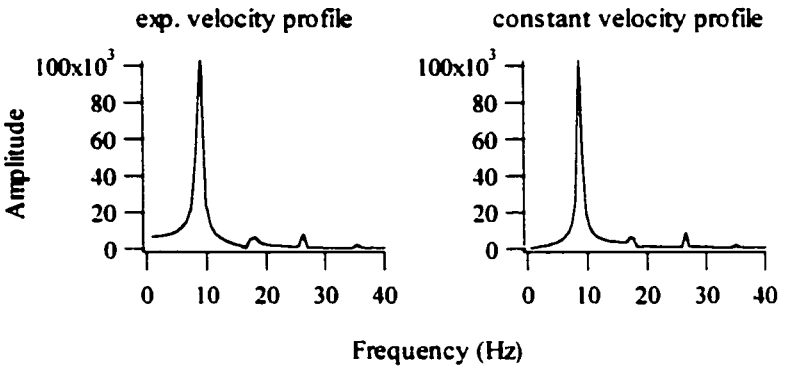

Figure 6.47: Temperature frequency spectra for an exponential and constant velocity profile. Location: z = 0.52, centerline. Case: (Fr = .01, Re = 40).

Figure 6.48 shows the time-averaged, temperature contours for an exponential inlet velocity profile and a constant inlet velocity profile. The flame height is similar for both cases.

It can be concluded that the inlet velocity profile has minor influence on the investigated flame dynamics. Though the exponential velocity profile provides a high shear near the pool rim, buoyancy forces are strong enough to dominate any effect the inlet velocity condition may have. This is supportive evidence that pool-like gas fires display similar gas-phase dynamics to that of pool fires, and thus further validates the model.

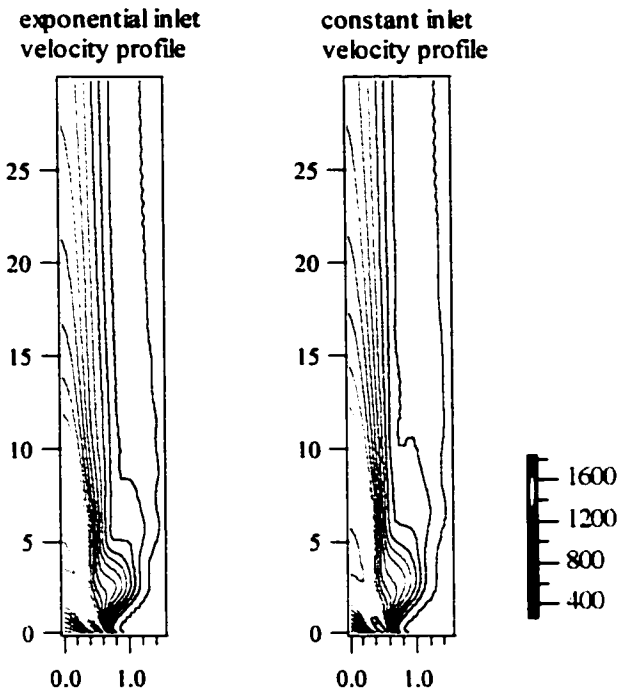

Figure 6.48: Time-averaged, temperature contours for an exponential and constant velocity profile. Dimensions are in diameters. Case: (Fr = .01, Re = 40).

6.7 Instantaneous Contours for case Fr = .001, Re = 40

In order to discuss additional features of the results thus far presented, instantaneous values in the form of contour and velocity vector plots are shown for the case, (Fr = .001, Re = 40). Figure 6.49 shows contours of temperature, vorticity, baroclinic torque, the gravitational term, vortex stretching, expansion and diffusion. In the temperature plot, the flame sheet is represented by the highest temperature contours. Figure 6.49.b indicates that negative vorticity is shown to occur on the fuel-side of the flame sheet, while areas of negative and positive vorticity occurs on the air-side of the flame sheet. The highest occurring values of vorticity occur along the flame sheet.

Baroclinic torque and the gravitational term are greatest around the flame sheet location, where density gradients are at a maximum. The density goes from a very low value at the flame sheet to a high value at the air interface. Thus, it can be expected that both vorticity generation terms would have maximum values around the flame sheet. It can also be seen that the vorticity and the gravitational term in the inner core are negative. Since the baroclinic torque does not have much influence in this region, the negative vorticity can be attributed to the gravitational term in the inner core. The gravitational term is also more distributed than baroclinic torque. Vortex stretching is seen to have positive values in areas of bulging and negative areas of necking. Vortex expansion is seen to occur mostly along the flame sheet. Areas of positive vorticity diffusion occur primarily in the central core, and negative diffusion occurs primarily outside of this region. The difference in sign is expected since the flame sheet separates the region where vorticity is greatest.

Figure 6.50 shows instantaneous contour plots of temperature, density, radial density gradients in the axial direction, axial velocity gradients in the radial direction, and radial velocity gradients in the axial direction. Contour plots of the averaged shear and buoyancy production of kinetic energy of fluctuations are also shown in Figure 6.50. The highest density gradients occur along the flame sheet, with the existence of positive density gradients in the axial directions. The density gradient plot indicates the existence of positive and negative areas. The buoyant production of kinetic energy of fluctuations indicates areas of positive and negative production as well. This indicates regions of stable and unstable configurations occurring. The unstable condition of positive axial density gradients, and hence positive buoyant production of kinetic energy of fluctuations, provides a source for fluid motion and the formation of vortices. The shear production of kinetic energy of deviation is greatest from axial velocity gradients in the radial direction, with production from radial velocity gradients in the axial direction negligible. This results from the high axial acceleration of gases by the large buoyancy forces. Though the Favre-averaged, spatially integrated values from Figure 6.4 indicate

that the net effect of shear production is negative, it can be seen that there are areas of positive and negative shear production. Thus, shear does provide local sources of instability.

Time averages of temperature were obtained for each case in order to compare flame structure. Time-averaged temperature contours over a cycle are shown in Figure 6.51. For (Re=100, Fr=.001), the flame is spread over a greater axial extent than the other cases due to the higher momentum. For cases (Re = 40, Fr=.01) and (Re = 10, Fr = .001) there is less mixing by the dynamic behavior of vortices, and thus the time-averaged, flame height is greater than that for cases (Re=40, Fr =.001) and (Re = 40, Fr = .0001). Case (Re= 40, Fr =.0001) has the least, time-averaged flame height due to the occurrence of the most energetic vortices and entrainment. With increasing entrainment, the fuel is consumed faster, and thus the flame height decreases.

Figure 6.52 shows the velocity vectors for methane, case Fr = .001, Re = 40, over a complete cycle. The formation of a vortex occurs very near the pool surface and rim then grows in diameter as it entrains the surrounding air. It can also be seen that the gases in the inner core are highly accelerated. The formation rate of the vortex shown coincides with the dominant frequency of the temperature spectra. This result agrees with the findings by other investigators that the pulsating nature of pool fires is directly linked to the rate of vortex formation.

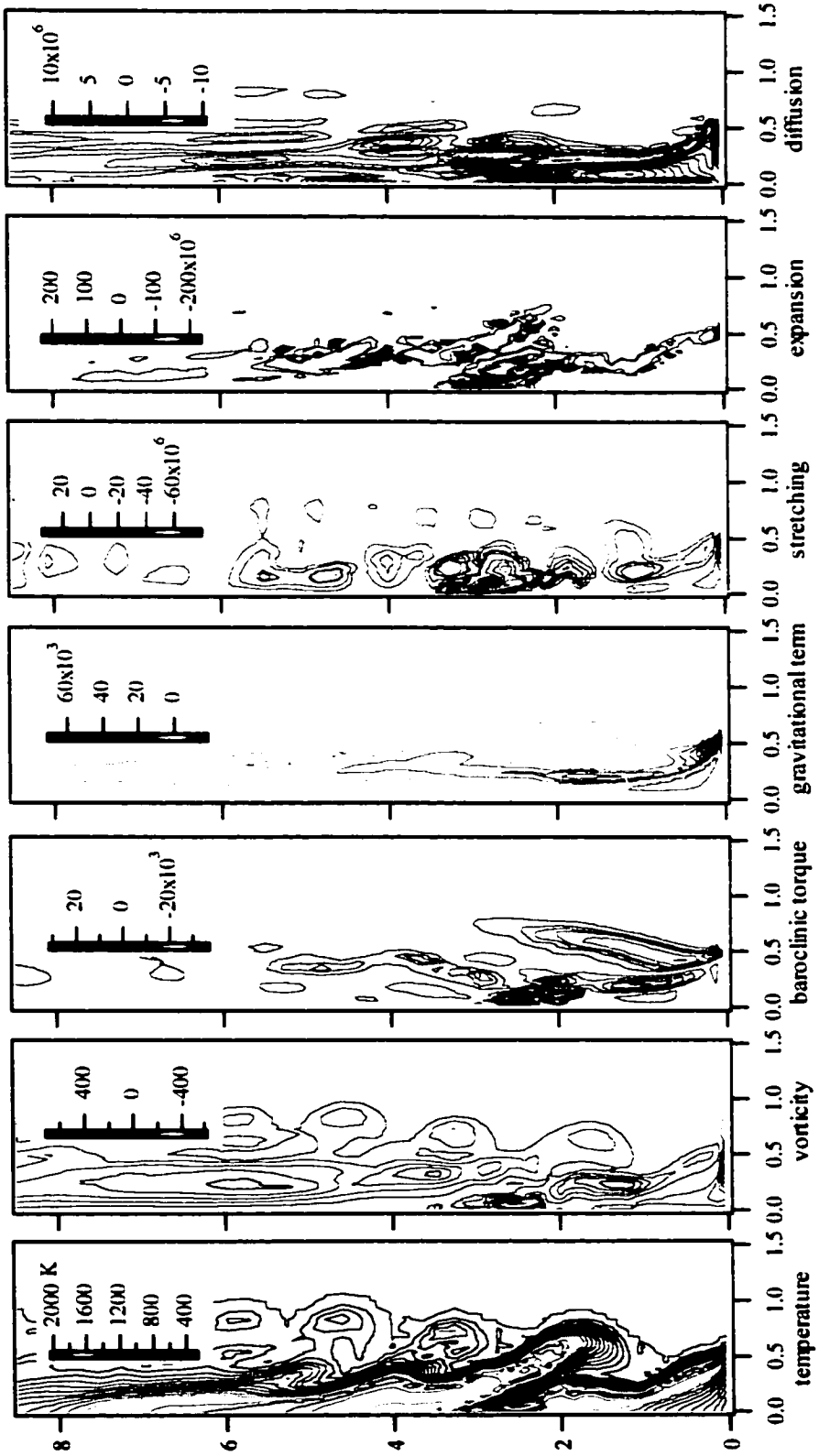

Figure 6.49: Instantaneous contour plots of temperature, vorticity, and vorticity terms in equation (6.1).

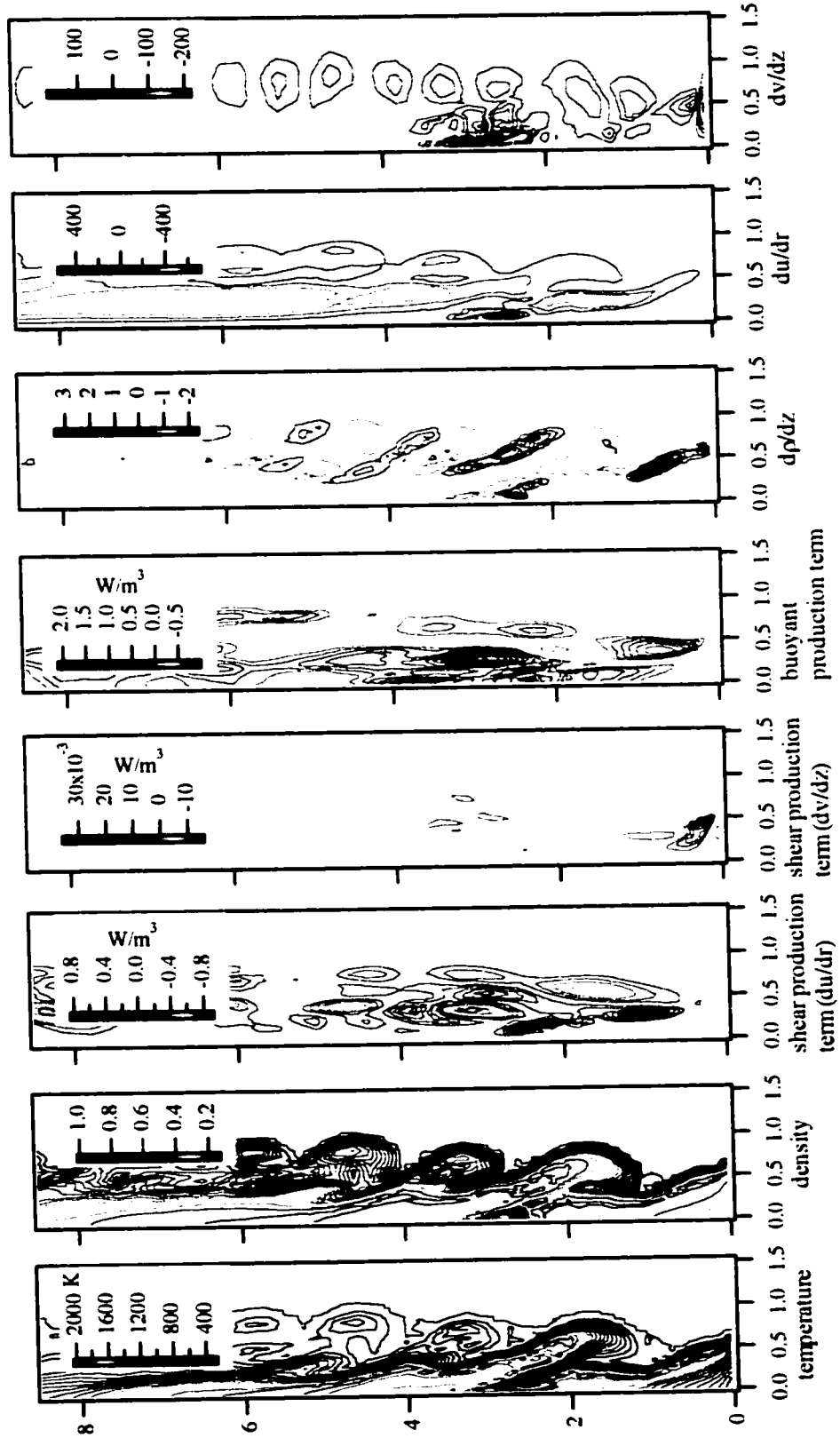

Figure 6.50: Contour plots of temperature, density, kinetic energy of deviations production terms, axial density gradients, axial velocity gradients in the radial direction, and radial velocity gradients in the axial direction.

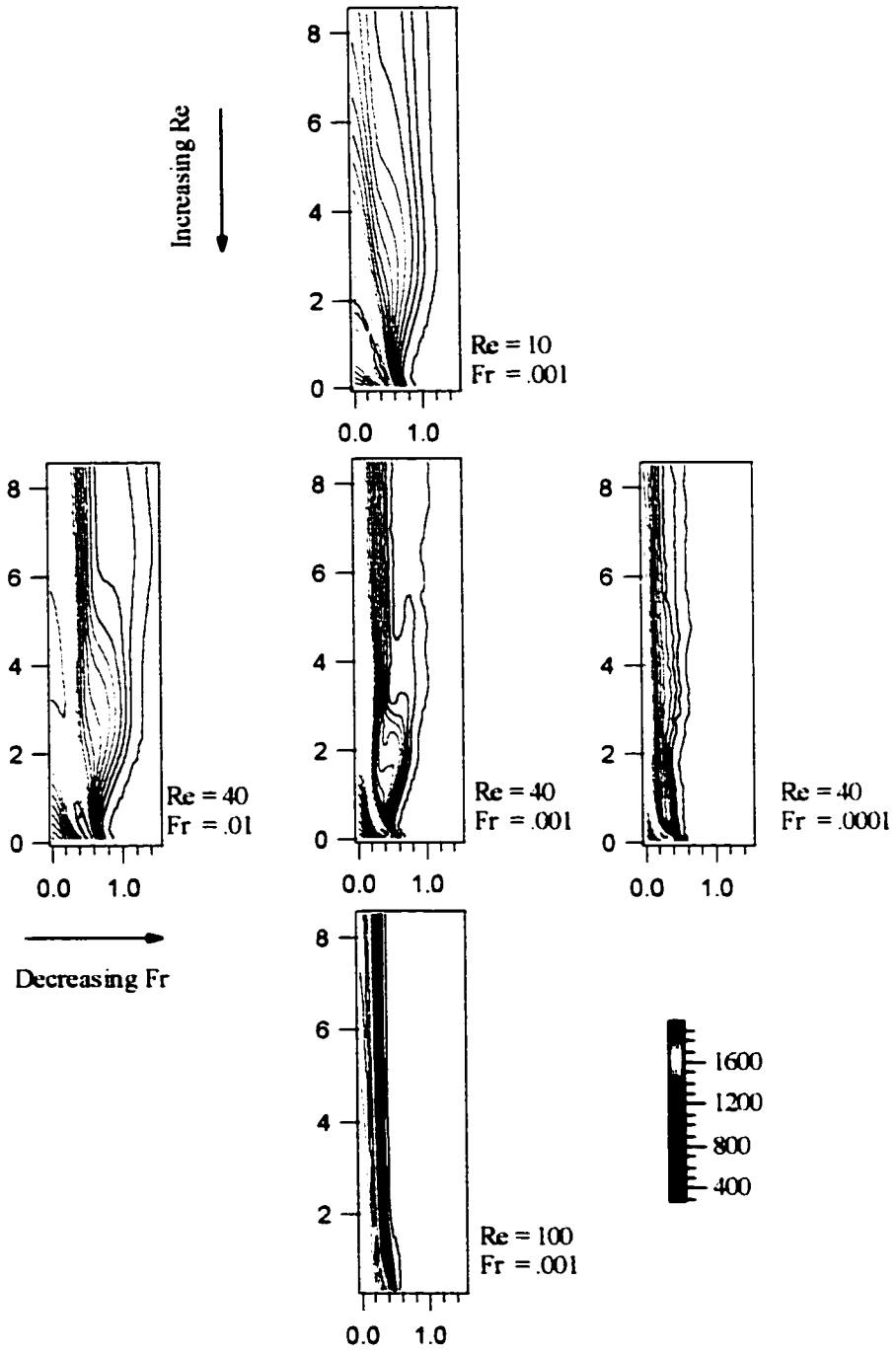

Figure 6.51: Time-averaged, temperature contours over a cycle for all cases.

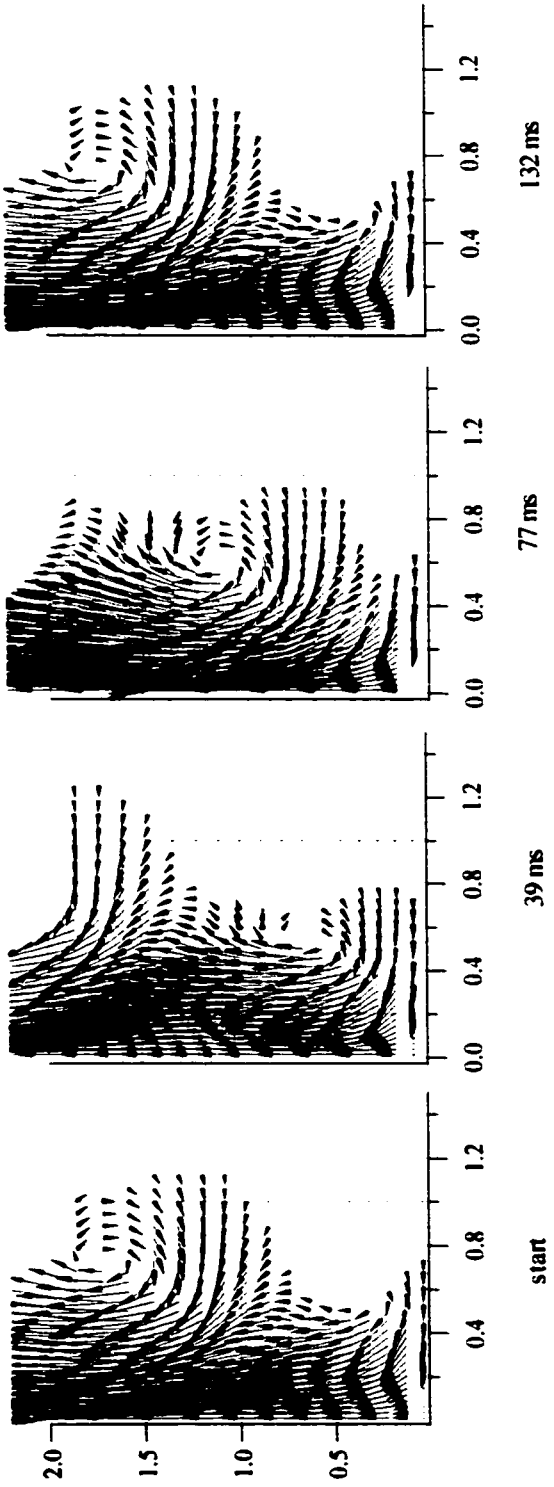

Figure 6.52: Velocity vectors over one cycle show the formation of a vortex. Case: methane, Fr = .001, Re = 40.

Chapter 7

Conclusions

The gas-phase dynamics of small circular pool fires have been investigated via direct numerical simulation. The aim of the present work is to assess the relative contributions of mechanisms that effect vortex formation. These mechanisms include vorticity production, Kelvin-Helmoltz instabilities, and Rayleigh-Taylor instabilities. The time-averaged, spatially integrated values of vorticity production, production of kinetic energy of fluctuations, and frequency spectra have been assessed for a range of source Froude and Reynolds numbers, $(10^{-4}\text{-}10^{-2})$ and $(10\text{-}10^{2})$ respectively, as well as fuel molecular weights, air-fuel ratios, and heat release rates. An approximate critical local Reynolds number has also been identified by using the available experimental visualizations of pool fires. The following sections provide a summary of the results, a conclusive statement about the results, as well as recommendations for future work.

7.1 Summary

For the summarized results that follow, the vorticity and vorticity production terms, that is baroclinic torque and the gravitational term in equation (6.1), refer to spatially integrated, time-averaged, absolute quantities. Similarly, the kinetic energy of fluctuations and its production terms, namely that due to shear and buoyancy effects as specified in equation (6.2), refers to spatially integrated, Favre-averaged quantities.

7.1.1 Vorticity Production Terms for Various Froude and Reynolds Numbers

The vorticity production terms have been assessed over a source Froude number range of $(10^{-4}\text{-}10^{-2})$ and Reynolds number range of $(10\text{-}10^{2})$ for methane. It has been

found that the gravitational production term in the vorticity transport equation (6.1) provides the greatest contribution to vorticity production for all parametric cases. The contribution from the gravitational term is approximately a factor of two greater than from baroclinic torque. Baroclinic torque occurs mostly at elevations of 2-3 diameters above the pool surface, while the gravitational term contributes throughout higher elevations, and thus is more distributed. Both terms increase with decreasing Froude number, and decrease with increasing Reynolds number, as does the integrated absolute values of vorticity. An order of magnitude change in Froude number resulted in the production terms changing by a factor of 5 approximately, while an order of magnitude change in Reynolds number resulted in the production terms changing by a factor of 1.5 approximately. Thus, the Froude number is the dominant parameter effecting these terms. This indicates that these terms are driven mainly by buoyancy forces.

7.1.2 Shear and Buoyancy Production Terms for Various Froude and Reynolds Numbers

The kinetic energy of fluctuations production terms have been assessed over a source Froude number range of (10^{-4}-10^{-1}) and Reynolds number range of (10-10^{2}) for methane. Fluctuations due to buoyancy production are greater than that due to shear production, approximately by a factor of two, for all cases. This shear production term is from axial velocity gradients in the radial direction. The shear production term from radial velocity gradients in the axial direction is negligible for all cases. The buoyancy production term and kinetic energy of fluctuations were found to increase with decreasing Froude number, and increase with increasing Reynolds numbers. Value of shear production were found to decrease for decreasing Froude number, and increase for increasing Reynolds number. For all cases, shear production values are negative, thus its net effect is to provide stability. However, not all regions have negative shear production. Local areas of instability occur with positive shear production, but when spatially integrated the negative contributions have a greater effect. Buoyancy production also has negative and positive areas occurring, but when spatially integrated the net effect

is positive, hence destabilizing, for all cases. Thus, it can be concluded that buoyant production is the dominant factor providing instabilities.

7.1.3 Frequency Spectra for Various Froude and Reynolds Numbers

Frequency spectra from temperature data at various locations have been determined over a source Froude number range of (10^{-4}-10^{-1}) and Reynolds number range of (10-10^2) for methane. The dominant frequency decreases with decreasing source Froude number, and decreases with increasing Reynolds number. The dominant frequency remained the same at all locations sampled, though amplitudes differed. The amplitudes increase by several orders of magnitude for an order of magnitude decrease in Froude number at all locations. The amplitudes decreased by a factor of ~ 2 for an order of magnitude change in Reynolds number, with the exception at the sampled location of z = 0.52 diameters and centerline where several orders of magnitude increase occurred. This indicates that the magnitude of fluctuations is dominated by the Froude number.

7.1.4 Local Reynolds number for Various Source Froude and Reynolds numbers

A Reynolds number has been interpreted as a function of elevation above the pool surface for over a source Froude number range of (10^{-4}-10^{-1}) and Reynolds number range of (10-10^2) for methane. The time-averaged, local Reynolds number increases with increasing source Reynolds number, and increases with decreasing source Froude number. The axial location at which this critical Reynolds number is reached for each case was found to decrease with decreasing source Froude number, and decrease with increasing source Reynolds number. Based on experimental evidence, an approximate critical local Reynolds number of 3000 as been identified as the limit of an axisymmetric model.

7.1.5 Effect of Heat Release Rate Varied by Fuel Inlet Density

The effect of the heat release rate varied by way of the fuel inlet density as been assessed for the case (Fr = .01, Re = 40) using methane. Heat release rates of 200, 300 and 400 watts were compared. Vorticity and the vorticity production terms are not effected by heat release rate.

The kinetic energy of fluctuations production terms were compared for the various heat release rates. Buoyancy production is not effected by heat release rate, whereas shear production increases with increasing heat release rate, approximately by 50% for a 100% increase in heat release rate. This shear production is from axial velocity gradients in the radial direction. Its spatially integrated values are negative for all cases. Shear production from radial velocity gradients in the axial direction is negligible for all cases. The kinetic energy of fluctuations increases with increasing heat release rate, approximately by 25% for a 100% increase in heat release rate.

The dominant frequency and amplitudes from temperature data remain the same for all cases at the location sampled. Time-averaged, local values of Reynolds number are not effected by heat release rate. Time-averaged, temperature contours indicate that the average location of the flame-sheet is shifted towards lower elevations for decreasing heat release rate.

7.1.6 Effect of Heat Release Rate Varied by Heat of Combustion

The effect of the heat release rate varied by way of the heat of combustion has been assessed for the case (Fr = .01, Re = 40). Heat release rates of 200 and 300 watts were compared. A change in the heat of combustion results in a change in flame temperature. Thus, the case of heat release rate of 200 watts has an average flame-sheet

temperature of 1860 K, whereas the case of heat release rate of 300 watts has an average flame-sheet temperature of 1393 K.

The vorticity production terms are effected by changes in flame temperature, but not by changes in heat release rate. Baroclinic torque decreases by approximately 50% and the gravitational term by 25% for a 25% decrease in flame temperature. Hence, flame temperature has a greater effect on baroclinic torque. Similarly, the vorticity decreases approximately 25% for a 25% decrease in flame temperature. Thus, flame temperature is a pertinent parameter that can influence vorticity.

The kinetic energy of fluctuations production terms were compared for various flame temperature cases. Buoyancy and shear production are not appreciably effected by flame temperature. This shear production is from axial velocity gradients in the radial direction. Its spatially integrated values are negative for all cases. Shear production from radial velocity gradients in the axial direction is negligible for all cases. The kinetic energy of fluctuations decreases by approximately 50% for a 50% decrease in flame temperature. The decrease in the kinetic energy with flame temperature was greater than that for the case with similar heat release rate, but different inlet fuel density. Thus, flame temperature is a parameter that can influence the energetics.

The dominant frequency from temperature data remains the same for all cases, though the amplitude decreases approximately 30% with a 25% decrease in flame temperature at the location sampled. Time-averaged, local values Reynolds number are not effected by flame temperature. Time-averaged, temperature contours indicate that the average location of the flame-sheet is approximately similar for equal heat release rates but different flame temperature.

7.1.7 Effect of Fuel Molecular Weight

The effect of fuel molecular weight has been assessed for case (Fr = .01, Re = 40). Methane, ethane, and propane, with respective molecular weights of 16, 30, and 44 were compared. Fuel molecular weight does not effect the vorticity production terms. Vorticity slightly decrease with increasing fuel molecular weight.

The kinetic energy of fluctuations production terms were accessed. The buoyancy production term is not effected by fuel molecular weight, and shear production decreases with fuels lighter and heavier than air. This shear production is from axial velocity gradients in the radial direction. Its spatially integrated values are negative for all cases. Shear production from radial velocity gradients in the axial direction is negligible for all cases. The kinetic energy of fluctuations decreases by approximately 20% with a 175% increase in fuel molecular weight.

The dominant frequency from temperature data remained the same for all cases, though the amplitude decreased by approximately 40% with each increase in fuel molecular weight at the location sampled. The time-averaged, local Reynolds number values are not effected by fuel molecular weight. Time-averaged, temperature contours indicate that increasing fuel molecular weight decreases flame height.

7.1.8 Effect of Air-Fuel Ratio

The effect of fuel air-fuel ratio by mass has been assessed for case (Fr = .01, Re = 40). A carbon monoxide-methanol mixture, having an air-fuel ratio of 4.6 and molecular weight of 30, was compared with ethane, which has an air-fuel ratio of 16.1 and molecular weight of 30. Vorticity and the vorticity production terms are not significantly effected by air-fuel ratio. Both production terms decreased slightly with a decrease in the air-fuel ratio.

The kinetic energy of fluctuations production terms are effected by air-fuel ratio. Buoyancy production increases and shear production decreases by a factor of 2 with a 70% decrease in air-fuel ratio. This shear production is from axial velocity gradients in the radial direction. Its spatially integrated values are negative for all cases. Shear production from radial velocity gradients in the axial direction is negligible for both cases. The kinetic energy of fluctuations decreases approximately 30% for a 70% decrease in air-fuel ratio.

The dominant frequency from temperature data remained the same for both cases, though amplitude increased by a factor of 7 for a decrease in air-fuel ratio at the location sampled. Time-averaged, local values of Reynolds number are not effected by air-fuel ratio. Time-averaged, temperature contours indicate that the average location of the flame-sheet is shifted towards lower elevations for decreasing air-fuel ratio.

7.1.9 Further Observations

Instantaneous contour plots (Figures 6.48 and 6.49) show additional features of the dynamics occurring in the gaseous flame region. Baroclinic torque and the gravitational term are greatest around the flame sheet location, where density gradients are at a maximum. The gravitational term is more distributed than baroclinic torque. Negative vorticity on the fuel side of the flame sheet can be attributed to the gravitational term. Negative vorticity occurs on the fuel side of the flame sheet, whereas negative and positive vorticity occur on the air side of the flame sheet. The highest values of vorticity occur along the flame sheet.

Vortex stretching has positive values in areas of bulging and negative areas of necking. Vortex expansion occurs mostly along the flame sheet. Areas of positive vorticity diffusion occur primarily in the central core, and negative diffusion occurs primarily outside of this region.

Negative and positive values of buoyant and shear production of kinetic energy of fluctuations occur. This indicates regions of stable and unstable configurations. The unstable condition of positive axial density gradients, and hence positive buoyant production of kinetic energy of fluctuations, provides a source for fluid motion and the formation of vortices. Although Favre-averaged, spatially integrated values indicate that the net effect of shear production is negative, there are areas of positive and negative shear production. Thus, shear does provide local sources of instability.

Vortex formation occurs near the pool surface and rim. A vortex grows in diameter and entrains the surrounding air as it travels upward due to the high buoyancy forces. Gases in the inner core are highly accelerated. The vortex formation rate coincides with the dominant temperature frequency, and thus is linked to the pulsating nature of the flame.

7.2 Summary of Conclusions

The aim of this work is to access the relative contributions to vortex formation from the vorticity production terms, shear instabilities, and unstable density stratifications. The conclusion is that the gravitational term, that is, radial density gradients interacting with gravity, and unstable density stratification as in a Rayleigh-Taylor instability are the dominant mechanisms effecting vortex formation. Baroclinic torque is approximately half to that of the gravitational term, and its principal effect occurs at lower elevations, approximately under 3 diameters. The net effect of shear is to provide stability, though local areas exist which are destabilizing. Local regions of stabilizing density stratification also occur. It has also been found that Froude number, Reynolds number, heat release rate, flame temperature, fuel molecular weight and air-fuel ratio can effect the investigated flame dynamics. It can be concluded that the Froude number is the dominant parameter effecting flame dynamics. It has been demonstrated

that an approximate critical local Reynolds number can be identified for which an axisymmetric model is valid. Using available experimental evidence, this value as been found to be around 3000. It has also been demonstrated with the model validation results that an axisymmetric, single-step, irreversible, reaction model with finite rate chemistry is capable of capturing essential features of the gas-phase of pool fires.

7.3 Recommendations for Future Work

The first recommendation for future work is to use an axisymmetric model, but to not include all of the simplification made in the present work. Thus, this could involve investigating the heat feedback and mass flux coupling at the pool surface, and incorporating a radiation and soot model. Radiation and soot modeling is especially important for larger fires, or lower Froude numbers, when radiation becomes the dominant mode of heat transfer to the pool surface and flame temperature decreases as a result of radiation. It has been shown in this work that flame temperature is a significant parameter. Secondly, it is recommended that azimuthal variations be investigated by developing a three-dimensional model. To be able to investigate all of the effects in the present work, and to have a reasonable length of run time, it would be necessary to develop a code that could be used on parallel computers. Multigriding techniques could also be incorporated to further decrease the computational run time. Further work is necessary to validate the local Reynolds number for which an axisymmetric simulation is valid. Laboratory experiments could be performed on several different diameters within the range of interest to obtain measurements of temperature, velocity, and detailed visualization. Finally, it is recommended that a turbulence model such as Large Eddy Simulation be utilized to investigate lower Froude numbers or larger fires.

LIST OF SYMBOLS

$\dot{\omega}_i$	production rate of specie i
c_p^{∞}	ambient specific heat at constant pressure
c_v^{∞}	ambient specific heat at constant volume
D_{ij}^{∞}	ambient binary diffusion coefficient
$\dot{Q}$	heat release rate
$\overline{\rho}$	time-averaged density
$\overline{p}$	time-averaged pressure
ρ'	fluctuating density
p'	fluctuating pressure
u''	fluctuating velocity
$\tilde{u}$	Favre-averaged velocity
c_p	mixture specific heat at constant pressure
c_v	mixture specific heat at constant volume
D	pool diameter
D_{ij}	binary diffusion coefficient
Fr	Froude number
MW_i	molecular weight of specie i
p	pressure
$p^{(0)}$	zeroth order pressure
$p^{(1)}$	first order pressure
Q	heat of combustion
r	radial coordinate
R	universal gas constant

Re	Reynolds number
Sc	Schmidt number
t	time
T	temperature
T^{∞}	ambient temperature
T_i	temperature of species i
T_{in}	inlet fuel temperature
v	velocity vector
v_{in}	inlet fuel velocity
v_r	radial velocity component
v_z	axial velocity component
Y_i	mass fraction of specie i
Z	mixture fraction
z	axial coordinate
T	shear stress tensor
α	grid stretching parameter
λ	stoichiometric air-fuel coefficient
μ	dynamic viscosity
μ_{in}	inlet fuel dynamic viscosity
ν_i	stoichiometric coefficient of specie i
ρ	mixture density
ρ^{∞}	ambient density
ρ_{in}	inlet fuel density
υ	kinematic viscosity
ω_θ	azimuthal vorticity component

Subscript symbols

O	oxidant
F	fuel
P	product

List of References

1. Akita, K. and Yumoto, T. (1965) Heat Transfer in Small Pools and Rates of Burning of Liquid Methanol, *Tenth Symposium (International) on Combustion*, pp. 943-948.

2. Barr, J., (1953) Flames of fuel jets. *Fourth Symposium (International) on Combustion*, p. 765.

3. Baum, H.R. and Rehm, R.G. (1990) Transient combustion in a turbulent eddy. *Twenty-Third Symposium (International) on Combustion*. pp. 715-722.

4. Blinov, V.I. and Khudyakov, G.N. (1957) Certain laws governing diffusive burning of liquids. *Academiia Nauk, SSSR Doklady*, , U.S. Army Translation NTIS number AD296762, pp. 1094-1098.

5. Buckmaster, J. and Peters, N., (1986) The infinite candle and its stability – a paradigm for flickering diffusion flames. *Twenty-first Symposium (International) on Combustion*, pp. 1829 –1836.

6. Buckmaster, J. D., and Ludford G.S. (1982), *Theory of Laminar Flames*, Cambridge University Press.

7. Burgess, D. and Hertzberg, M. (1974) *Heat Transfer in Flames*, Eds. Afgan, N. H. and Beers, J. M., John Wiley & Sons, New York, NY, Chapter 27.

8. Byram, G. M. and Nelson, R. M. (1970) The modeling of pulsating fires. *Fire Tech.* **6**, pp. 102-110.

9. Cetegen, B. M. and Ahmed, T. A. (1993) Experiments on the periodic instability of buoyant plumes and pool fires. *Combust. Flame*, **93**, pp. 157-184.

10. Cetegen, B. M. and Dong, Y. (2000) Experiments on the instability modes of buoyant diffusion flames and effects of ambient atmosphere on the instabilities. *Experiments in Fluids*, **28**, pp. 546-558.

11. Cetegen, B. M. and Kasper, K. D. (1996) Experiments on the oscillatory behavior of buoyant plumes of helium and helium-air mixtures. *Phys. Fluids*, **8** (11), pp. 2974-2984.

12. Chamberlin, D.S. and Rose, A. (1928) The flicker of luminous flames. Industr. Eng. Chem., 20, pp. 1013-1016.

13. Chandrasekhar S. (1961) *Hydrodynamic and Hydromagnetic Stability*, Oxford University Press

14. Chen, L. D., Vilimpoc, V., Goss, L. P., Davis, R. W., Moore, E. F., Roquemore, W. M. (1992) Time evolution of a buoyant jet diffusion flame. *Twenty-fourth Symposium (International) on Combustion*, pp. 303-310.

15. Corlett, R. C. (1968) Gas Fires with Pool-Like Boundary Conditions. *Combustion and Flame*, **12**, pp. 19-32.

16. Cox, G., (1995*) Combustion Fundamentals of Fires* (1st ed.) Academic Press, London, p. 101.

17. Davis, R. W., Moore, E. F., Roquemore, W. M., Chen, L. –D., Vilimpoc, V. and Goss, L. P. (1991) Preliminary results of a numerical-experimental study of the dynamic structure of a buoyant jet diffusion flame. *Combust. and Flame*, **83**, pp. 263-270.

18. Eckert, E. R. and Drake, R. M. (1972) *Analysis of Heat and Mass Transfer.* McGraw Hill, New York.

19. Ferziger, J.H. and Peric, M. (1996) *Computational methods for fluid dynamics*,
Springer, Germany.

20. Ghoniem, A. F., Lakkis, I, and Soteriou, M. (1996) Numerical simulation of the dynamics of large fire plumes and the phenomenon of puffing. (1996) *Twenty-Sixth Symposium (International) on Combustion*, pp. 1531-1539.

21. Hamins, A., Yang, J.C. and Kashiwagi, T. (1992) An experimental investigation of the pulsation frequency of flames. *Twenty-Fourth Symposium (International) on Combustion.* pp. 1695-1702.

22. Heskestad, G. (1983) *Fire Safety J.*, **5**, p. 103.

23. Hottel, H.D. (1961) Review. *Fire Res. Abs.* **1**, pp. 41- 44.

24. Jiang, X, and Luo, H. (2000) Combustion-induced buoyancy effects of an axisymmetric reactive plume. *Proceedings of the Combustion Institute*, **28**, pp.1989-1995.

25. Katta, V.R., Goss, L. P., Roquemore, W. M. (1994) Effect of nonunity lewis number and finite-rate chemistry on the dynamics of a hydrogen-air jet diffusion flame. *Combust. and Flame*, 96, pp.60-74.

26. Kuldeep, P., Li, C., Kailasanath, K., Ndubizu, C., Anath, R and Tatem P.A. (1999) Numerical modelling of methanol liquid pool fires. *Combust. Theory Modelling*, **3**, pp. 743-768.

27. Kundu, P. K. (1990) *Fluid Mechanics*, Academic Press, Inc., California.

28. Lee, D. E. and Baek, S. W. (1998) Numerical simulation of a pool fire. *KSME Int. Journal*, **12**, 5, pp.980-987.

29. McMurtry, P.A., Jou, W.-H., Riley, J. J., and Metcalfe, R. W. (1986) Direct numerical simulations of a reacting mixing layer with chemical heat release. *AIAA J.*, **24**, pp. 962-970.

30. McNally, C.S., Pfefferle, L.D., Schaffer, A.M., Long, M.B., Mohammed, R.K., Smooke, M.D. and Colket, M.B. (2000) Characterization of coflowing methane/air non-premixed flame with computer modeling, rayleigh-raman imaging and on-line mass spectrometry. *Proceedings of the Combustion Institute*, **28**, pp. 2063-2070.

31. Mell, W. E., McGrattan, K. B. and Baum, H. R. (1996) Numerical simulation of combustion in fire plumes. *Twenty-Sixth Symposium (International) on Combustion*, pp. 1523-1530.

32. Mitchell, R.E., Sarofim, A.F. and Clomburg, A. (1980) Experimental and numerical investigation of confined laminar diffusion flames. *Combust. Flame*, **37**, pp. 227 – 244.

33. Mitchell, R.E., Sarofim, A.F. and Clomburg, A. (1980) Partial equilibrium in the reaction zone of methane-air diffusion flames. *Combust. Flame*, **37**, pp. 201 – 206.

34. Most J., Mandin, P., Chen, J. and Joulain P. (1996) Influence of gravity and pressure on pool fire-type diffusion flames. *Twenty-Sixth Symposium (International) on Combustion*, pp.1311-1317.

35. Rehm, R. G. and Baum, H. R. (1978) The equations of motion for thermally driven, buoyant flows. *Journal of Research of the National Bureau of Standards*. **83**, pp. 297-308.

36. Reid, R. C., Prausnitz, J. M., and Poling, B. E., (1987) The Properties of Gases & Liquids, McGraw-Hill.

37. Santoro, R.J., Yeh, T.T., Horvath, J.J. and Semerjian, H.G. (1987) The transport and growth of soot particles in laminar diffusion flames. *Combust. Sci. and Tech*, **53**, pp. 89-115.

38. Sato, H., Amagai, K. and Arai, M. (2000) Flickering frequencies of diffusion flames observed under various gravity fields. *Proceedings of the Combustion Institute*, **28**, pp.1989-1995.

39. Schonbucher, A., Banhardt, A.V., Bieller, V., Kaufmann, K.M., Lucas, R. and Schiess, N. (1986) Simultaneous observations of organized density structures and the visible field in pool fires. *Twenty-first Symposium (International) on Combustion*, pp. 83 –92.

40. Sibulkin, M., and Hansen, A. G. (1975) Experimental study of flame spreading over a horizontal surface. *Combustion Science and Technology*, **10**, pp. 85-92.

41. Smooke M. D., McEnally, C. S., and Pfefferle, L. D. (1999) Computational and experimental study of soot formation in a coflow, laminar diffusion flame. *Combust. Flame*, **117**, pp. 117-139.

42. Tieszen, S. R., Nicolett, V. F., Gritzo, L. A., Holen, J.K., Murray, D., and Moya, J. L. (1996) Vortical structures in pool fires: observations, speculation, and simulation. SAND 96-2607.

43. Versteeg, H.K. and Malalasekera, W. (1995) *An introduction to computational fluid dynamics the finite volume method*, Longman.

44. Weckman, E. J. and Sobiesiak, A. (1988) The oscillatory behaviour of medium-scale pool fires. *Twenty-second Symposium (International) on Combustion*, pp. 1299-1310.

45. Wilke, C. R., (1950) Viscosity Equation for Gas Mixtures. *J. Chem. Phys.*, **18**(4), pp. 517-519.

46. Yuan, T. Durox T., and Villermaux E. (1994) An analogue study for flame flickering. *Experiments in Fluids*, **17**, pp. 337-349.

Vita

Anay Luketa-Hanlin was born in Seattle, Washington. She is married to Brian Hanlin and has two daughters, Kathryn and Amanda, 5 and 12, respectively. She attended Seattle University, graduating with a Bachelor of Science in Mathematics and Bachelor of Arts in Psychology in 1987. She then attended the University of Washington, graduating with a Master of Science in Mechanical Engineering in 1996, and then a Doctor of Philosophy in Mechanical Engineering in 2002.